EVIDENCE FOR ANOMALOUS COSMIC RAY HYDROGEN

Thesis by

Eric R. Christian

In Partial Fulfillment of the Requirements

for the Degree of

Doctor of Philosophy

California Institute of Technology

Pasadena, California

1989

(Submitted February 15, 1989)

SRL 89-01

Acknowledgements

I would like to thank my advisor, Dr. Edward Stone, for all of his guidance during my time at Caltech. I have learned much and feel I am a better researcher due to his advice and supervision.

I am also indebted to the many people responsible for the highly successful *Voyager* missions, and especially those involved in the *Voyager* CRS experiments. Special thanks to Dr. Alan Cummings, with whom I have enjoyed working, and Dr. Frank McDonald and Dr. Bill Webber, who have been helpful and supportive even when we have disagreed.

There are also many people at the Caltech Space Radiation Laboratory who have been extremely helpful. Specifically, I promised to thank Randy Burrell, who spent so many hours running data tapes for me. Also I would like to thank Dr. Steve Schindler and my other co-workers on the HEIST balloon experiment who made my years on that project so interesting. I also have to thank J. Eric Grove, Dr. Koon H. Lau, David Palmer and all of the other students with whom I have shared the trials and tribulations of graduate school.

My *Voyager* work has been supported in part by NASA under contract NAS 7-918 and grant NGR 05-002-160. I also gratefully acknowledge the tuition, scholarship, and other support provided by the California Institute of Technology.

Last and most of all, my wife, Christine Gallant, has in many ways been responsible for my getting to this point. I cherish her love and support over the years, and the hours she has spent helping me prepare this thesis have been valuable beyond measure.

Abstract

The High Energy Telescopes on the *Voyager 1* and *Voyager 2* spacecraft are used to measure the differential energy spectra of hydrogen and other elements. During the period of minimum solar modulation in 1987, changes in the shape of the hydrogen energy spectra are observed. It is shown that these changes are difficult to explain in the framework of current modulation theory, and are consistent with the emergence of an anomalous cosmic ray (ACR) hydrogen component. ACR hydrogen is predicted by the current theories of anomalous cosmic rays, but this is the first evidence that ACR hydrogen is actually present. Several different estimates of the contribution of ACR hydrogen are used to obtain peak fluxes of 0.33 ± 0.12 particles/m^2 s sr MeV and 0.67 ± 0.18 particles/m^2 s sr MeV for *Voyager 1* and *Voyager 2* respectively during the time period 1987/209-313.

Using a model developed by Cummings and Stone (1987), we relate these fluxes of ACR hydrogen and the peak fluxes of ACR helium to the relative abundance of hydrogen and helium, n(H I)/n(He I), in the neutral gas flowing into the solar system from the local interstellar medium. For two different choices of parameters, we obtain values of 3 ± 1 and 5 ± 3 for n(H I)/n(He I), which should be compared to the cosmic relative abundance of ~ 10. Our values are consistent with previous results obtained from solar ultraviolet backscatter experiments, and support the hypothesis that hydrogen is substantially ionized in the very local interstellar medium.

Table Of Contents

Chapter 1

Introduction

1.1. Cosmic Rays

Only in the last fifteen years have we known of the existence of anomalous cosmic rays. Anomalous cosmic rays are an unusual component of the population of extraterrestrial energetic particles. Because anomalous cosmic rays are not the dominant component, their study requires knowledge of the other constituents as well.

The study of cosmic rays began when Hess (1912) discovered an extraterrestrial source of ionizing radiation, which is now known to consist primarily of charged particles. These charged particles are mostly protons and heavier atomic nuclei with a few percent electrons and positrons. The energetic nuclei are partially or fully stripped of electrons and have an elemental composition roughly the same as the composition of the solar system (see, e.g., Simpson 1983). Nuclei with kinetic energies greater than 1 MeV can be divided into several distinct populations of particles.

Particles with kinetic energies less than a few MeV are primarily solar energetic particles (SEPs) and energetic storm particle events. These particles are accelerated by solar flares and shocks in the solar wind. Figure 1.1 is a proton energy spectrum from the *Voyager 2* Cosmic Ray Subsystem, in which the SEP component can be seen as the steeply falling portion of the energy spectrum at low energies. SEPs are treated as background in this analysis, as this dissertation is primarily concerned with more energetic phenomena.

1.1.1. Galactic Cosmic Rays and Modulation

The proton energy spectrum in Figure 1.1 from ~20 MeV and up is dominated by galactic cosmic rays (GCRs). Cosmic rays provide a unique sample of particles from outside the solar system, although their precise source is still in question. They originate in the galaxy, probably within 10^3 parsecs (Ormes and Freier 1978), and they are accelerated by magneto-hydrodynamic shocks (see, e.g., Simpson 1983 for a review). These cosmic ray nuclei diffusively propagate in the galaxy, which modifies the accelerated energy spectrum. The galactic energy spectrum is further changed by the interaction of the cosmic rays with the heliosphere in a process known as modulation. The shape of the observed galactic cosmic ray proton energy spectrum seen in Figure 1.1 is a consequence of both the presumably constant galactic energy spectrum and a time variable level of solar modulation.

The dynamic properties of the heliosphere are established by an outward flowing solar wind formed from the expansion of the solar corona (see, e.g., Axford 1985). This solar wind contains a frozen-in magnetic field and extends out to the heliopause, which is the boundary between the solar wind and the local interstellar medium. Because the solar wind is supersonic, it is expected to undergo a shock transition before it reaches the heliopause. This solar wind shock is expected to be somewhere ~50 - 100 AU from the sun (Webber 1987; Axford 1985; McKibben 1988).

The properties of the solar wind vary throughout the 11 year solar activity cycle and thus the modulation level is also affected by the solar cycle, resulting in an anticorrelation between the flux of low energy galactic cosmic rays and the activity level of the sun, as first shown by Forbush (1954). There are several major processes involved in cosmic ray modulation. The particles are diffusing into the solar system and at the same time they are being convected out with the solar wind. In addition to

the diffusion process, there are drifts, both gradient and curvature, although the exact role of these drifts is still unclear. The particles are also losing energy in the adiabatic expansion of the solar wind. Low energy galactic cosmic rays are excluded from the solar system because their convection out of the solar system is faster than their diffusion in. The low energy portion of the observed galactic cosmic ray energy spectrum in Figure 1.1 is composed of cooled particles with initially higher energies, and the shape of this region of the energy spectrum has a flux proportional to the kinetic energy shape, which is expected for adiabatically cooled particles (Rygg and Earl 1967).

The solar wind characteristics also vary with the 26 day solar rotation period. All observation periods used in this dissertation are multiples of 26 days, to average out any effects due to solar rotation.

1.1.2. Anomalous Cosmic Rays

Until the mid 70s, solar energetic particles, galactic cosmic rays, and particles accelerated in the interplanetary medium were the only known extraterrestrial energetic particles. However, Garcia-Munoz *et al.* (1973) reported that the helium energy spectrum from 10 MeV/nucleon to 80 MeV/nucleon was essentially constant and not proportional to kinetic energy as expected from simple modulation theory. The energy spectra of oxygen and nitrogen were also found to have large excesses of flux in the intermediate energies between the SEP component and the galactic energy spectrum (Hovestadt *et al.* 1973; McDonald *et al.* 1974) whereas the carbon energy spectrum showed no such enhancement in flux (Figure 1.2).

These excess fluxes were interpreted as resulting from a new component of cosmic ray with an anomalous composition. A solar origin for these anomalous cosmic rays (ACRs) was ruled out by the positive radial gradient observed (e.g., McDonald *et al.*

Figure 1.1

Voyager 2 hydrogen energy spectrum from the time period 1978/353 - 1979/14. The dotted line represents the power law for the solar energetic particle component and the dashed line shows the galactic cosmic ray energy spectrum.

Figure 1.1

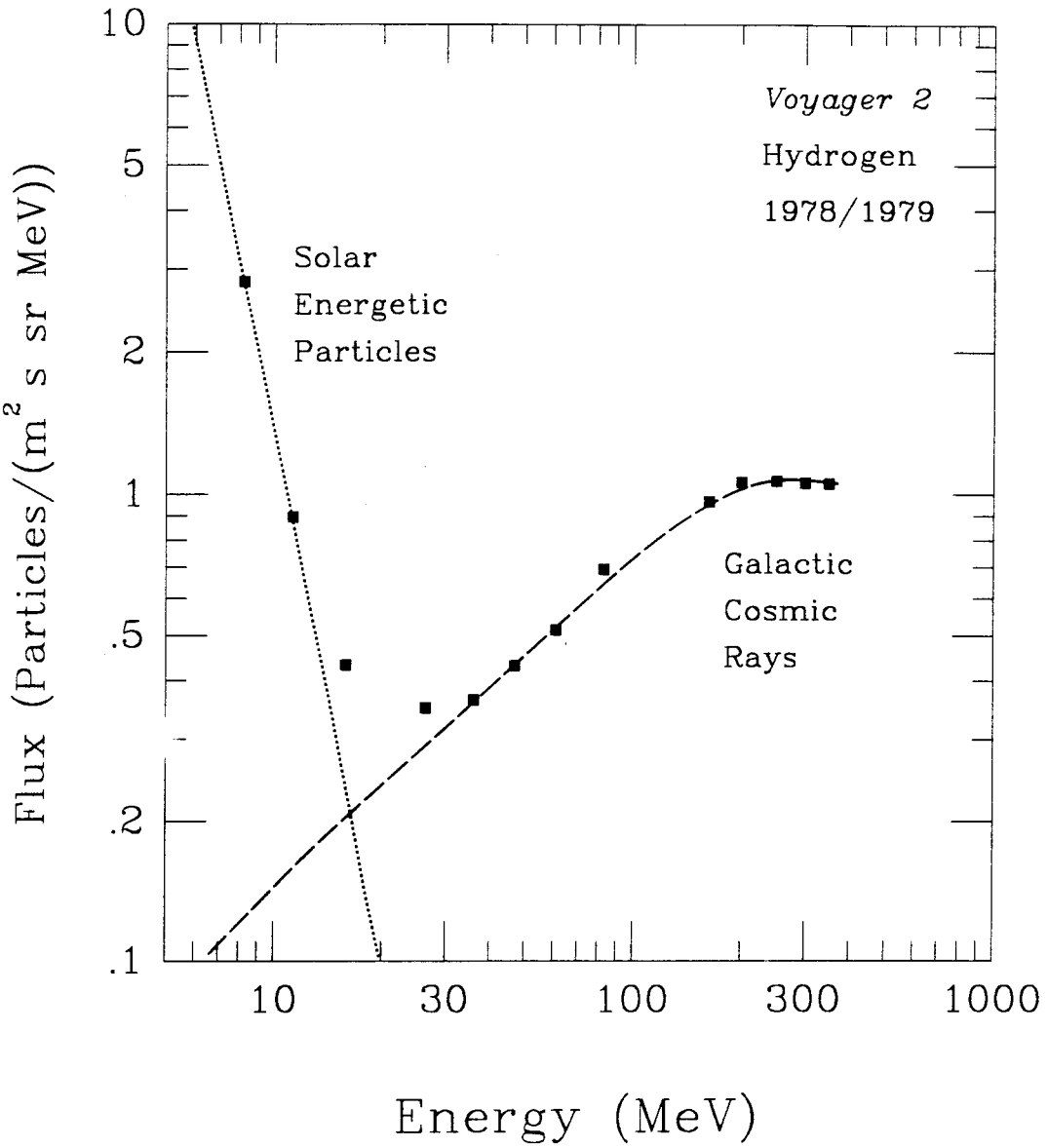
10
5
2
1
.5
.2
.1
Flux (Particles/(m^2 s sr MeV))
Voyager 2
Hydrogen
1978/1979
Solar
Energetic
Particles
Galactic
Cosmic
Rays
10
30
100
300
1000
Energy (MeV)

Figure 1.2

Quiet time energy spectra for the elements H, He, C, N, and O measured at 1 AU over the period from 1974 to 1978. Note the "anomalous" enhancements in the low-energy spectra of He, N, and O. The H and He points below 40 MeV per nucleon are 1975 data from the EIS instruments on *IMP-7* and *IMP-8*, while the higher energy points are 1975 data from the University of Chicago experiment on *IMP-7* (Garcia-Munoz, Mason, and Simpson 1977). For C, N, and O the *IMP-8* EIS data were obtained from 1974 to 1976, and extend from $\sim$4 to $\sim$50 MeV per nucleon. Data at $\sim$25 MeV per nucleon and at $>$50 MeV per nucleon are Chicago *IMP-8* data from 1974 to 1978 (Garcia-Munoz *et al.* 1979). For the GCR component the smooth lines are fits that assume a source spectrum $dJ/dT \propto (T + 400\ \text{MeV per nucleon})^{-2.6}$ (where J is the particle flux and T the kinetic energy per nucleon) and a solar modulation level of $\Phi = 300$ MeV per nucleon. Curves through the low-energy enhancements have been drawn by eye.

(From Mewaldt, Spalding, and Stone 1984).

Figure 1.2

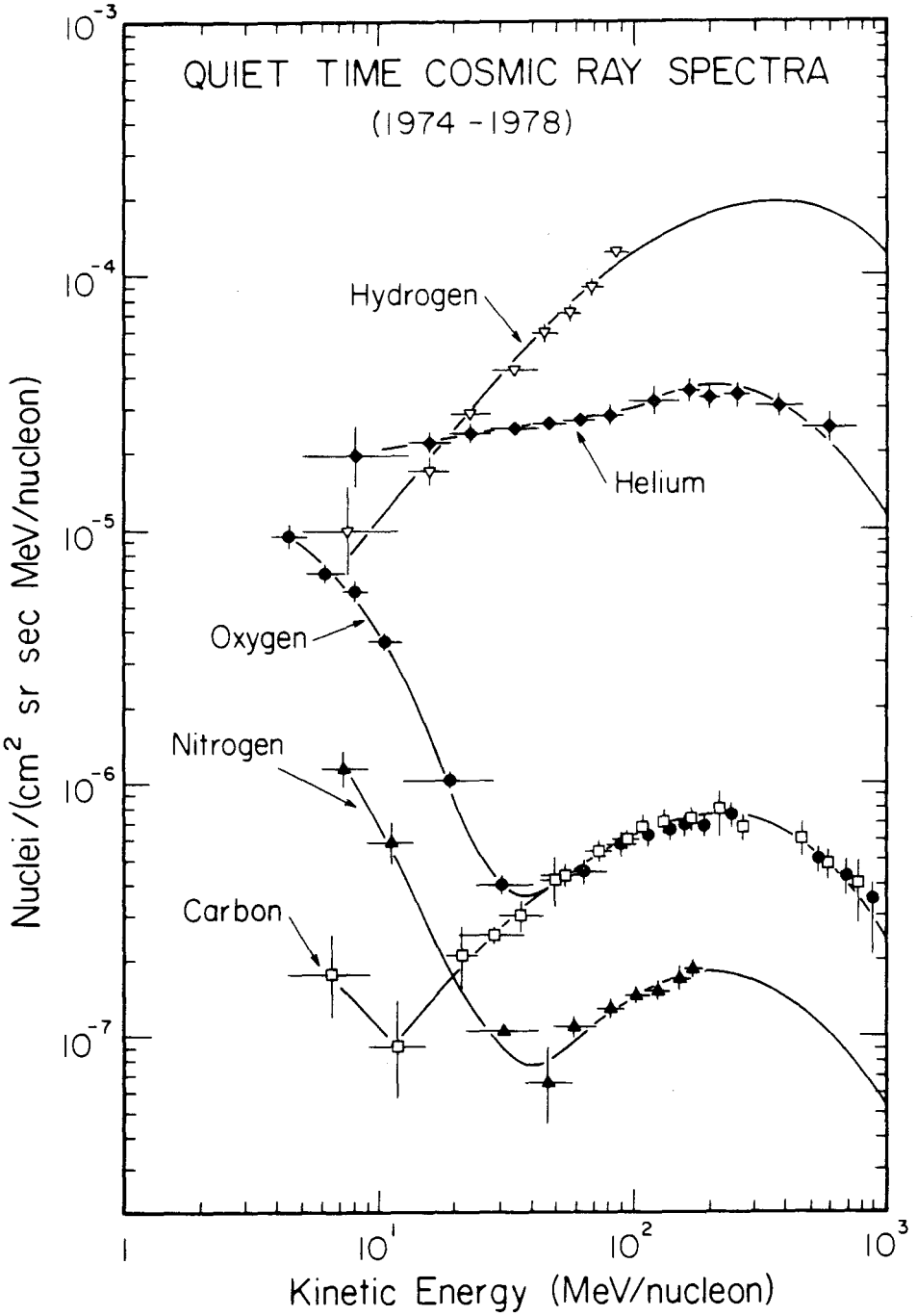
QUIET TIME COSMIC RAY SPECTRA
(1974 - 1978)
Hydrogen
Helium
Oxygen
Nitrogen
Carbon
Nuclei/(cm² sr sec MeV/nucleon)
Kinetic Energy (MeV/nucleon)
10⁻³
10⁻⁴
10⁻⁵
10⁻⁶
10⁻⁷
1
10¹
10²
10³

1974). The curious composition and the fact that the observations were inconsistent with a galactic component being modulated by the sun were strong arguments against a galactic origin. Indeed the fact that the enhanced component of helium consists entirely of ^{4}He (Garcia-Munoz *et al.* 1976) and that the excess nitrogen is predominantly ^{14}N (Mewaldt *et al.* 1975; Mewaldt *et al.* 1976) indicates that there has been no fragmentation of the anomalous cosmic ray component (which would form some ^{3}He and ^{15}N); therefore, the origin of this component is local.

The currently accepted theory that best fits the observations is that the anomalous cosmic rays are interstellar neutrals (Fisk, Kozlovsky, and Ramaty 1974), which, because they are neutral, can be swept far into the heliosphere by the relative motion of the sun and the local interstellar medium. They are then singly ionized near the sun by photoionization or charge exchange with the solar wind. These ions are then picked up by the solar wind, convected outwards in the heliosphere, and accelerated at the solar wind termination shock (Pesses, Jokipii, and Eichler 1981; Jokipii 1986; Potgieter and Moraal 1988). This process is illustrated in Figure 1.3.

These particles diffuse back into the solar system more easily than galactic cosmic rays of the same kinetic energy per nucleon because the rate of diffusion is proportional to a positive power of the particles' magnetic rigidity, R, which is the momentum per unit charge.

$$R = \frac{p\,c}{Z\,e} \quad . \tag{1.1}$$

The particle momentum is p, c is the speed of light, Z is the particle charge state, and e is the charge of the electron. Thus the singly ionized anomalous cosmic rays propagate in the solar wind more easily than the fully ionized galactic cosmic ray nuclei because at a given energy per nucleon, the anomalous cosmic rays have a much higher rigidity.

The anomalous composition of this component is then explained, because the relative abundances of the anomalous cosmic rays will reflect the neutral abundances of the local interstellar medium. Thus the abundant elements with high ionization potentials, such as He, N, O, and Ne (Garcia-Munoz *et al.* 1973; McDonald *et al.* 1974; Hovestadt *et al.* 1973), were the first detected. Carbon is not as abundant in anomalous cosmic rays because it is mostly ionized in the interstellar medium. However, the observation of a carbon ACR component has recently been reported, along with an ACR component of argon (Cummings and Stone 1987).

Hydrogen is probably partially ionized in the very local interstellar medium (VLISM) although the degree of ionization is in question (see, e.g., Cox and Reynolds 1987). Even so, it should be the most abundant neutral in the VLISM. Because it is easily ionized by photoionization or charge exchange with the solar wind, it has been suggested that hydrogen should also have an ACR component (see, e.g., Fisk 1986). However, as pointed out by Fisk (1986) the likely peak energy and shape of an anomalous cosmic ray hydrogen energy spectrum may be very similar to the modulated galactic cosmic ray hydrogen energy spectrum, thus making it difficult to distinguish between the two. This is due to the fact that there is no difference in the charge state of ACR hydrogen and GCR hydrogen and thus the particle propagation in the heliosphere will be similar.

Yet the identification of an anomalous cosmic ray hydrogen component would clearly add to our understanding of anomalous cosmic rays, the heliosphere, and local interstellar medium. The amount of hydrogen accelerated at the termination shock can have effects on the dynamics of the shock (Lee and Axford 1988; Drury 1988). A measurement of the ACR hydrogen flux would also be another step towards relating the

Figure 1.3

Generation of anomalous cosmic rays. Neutrals from the very local interstellar medium (VLISM) flow into the heliosphere due to the relative motion of the solar system and the VLISM. The neutrals are singly-ionized through photoionization or charge exchange and then convected out of the solar system with the solar wind (Fisk, Kozlovsky, and Ramaty 1974). They are subsequently accelerated at the solar wind termination shock (see, e.g., Pesses, Jokipii, and Eichler 1981) and can diffuse back into the solar system.

Figure 1.3

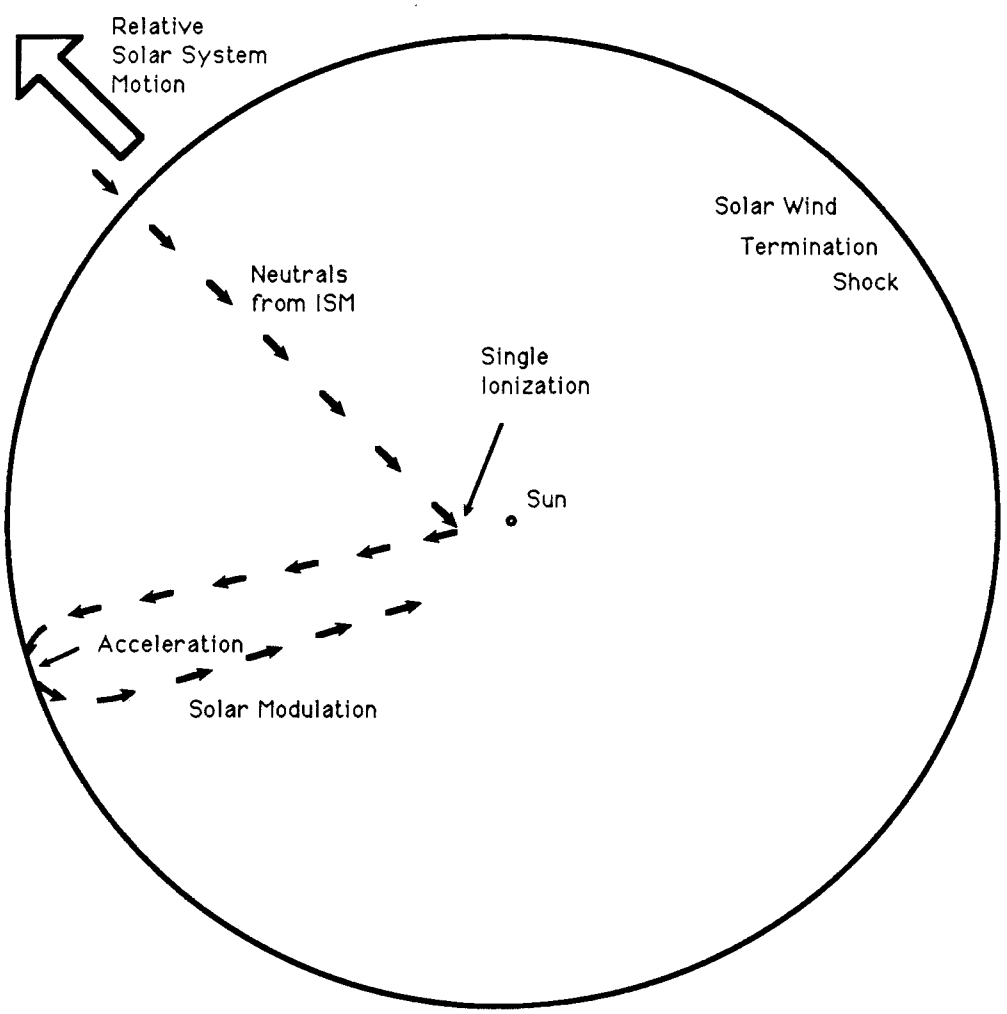
Relative
Solar System
Motion
Solar Wind
Termination
Shock
Neutrals
from ISM
Single
Ionization
Sun
Acceleration
Solar Modulation

ACR composition to that of the interstellar neutrals. Whereas galactic cosmic rays are a sample of material from many distant locations, anomalous cosmic rays sample only the region just outside the heliosphere, which is called the very local interstellar medium.

1.2. The Local Interstellar Medium

The solar system seems to be surrounded by a large hot (10^6 K) bubble of gas, which extends out several tens of parsecs (Cox and Reynolds 1987 and references therein). The density of this region is surprisingly low, only about 4×10^{-3} cm^{-3}. More important to the study of anomalous cosmic rays is the evidence that the solar system is at the edge of a small interstellar cloud, as first suggested by Vidal-Madjar *et al.* (1978). Observations of the optical and ultraviolet absorption lines in the energy spectra of nearby stars indicate that there may be several small clouds within a few parsecs of the solar system (Vidal-Madjar *et al.* 1985; Ferlet *et al.* 1986), but we cannot tell whether the heliosphere is actually embedded in one of these clouds.

However, there does exist a more direct way of measuring the parameters of the local gas. Observations of backscattered solar H Ly α 1216 angstrom and He 584 angstrom emission lines have provided information about the densities and temperature of interstellar H I and He I atoms flowing into the solar system (e.g., Weller and Meier 1981; Dalaudier *et al.* 1984; Bertaux *et al.* 1985). These measurements are especially relevant, because it is these atoms that are ionized and then accelerated to become anomalous cosmic rays.

Recent results agree that the VLISM is denser and colder than its surrounding hot bubble, with a total density $\sim$0.1 - 0.2 cm^{-3} and a temperature of about 10^4 K. The measured H I density is $\sim$0.06 - 0.07 cm^{-3} and the He I density is $\sim$0.01 cm^{-3}

(Chassifière *et al.* 1986; Ajello *et al.* 1987). The comparison of these values and the results of this dissertation will be discussed in §4.2.4.

In this dissertation, the energy spectra of hydrogen observed near the time of maximum fluxes in 1985 to 1987 from instruments on the *Voyager 1* and *Voyager 2* spacecraft are carefully examined. The spectral changes seen represent the first evidence for the existence of anomalous cosmic ray hydrogen.

Chapter 2

The Experiment and Data Analysis

2.1. The Experiment

The *Voyager 1* and *Voyager 2* spacecraft were launched on September 5 and August 20, 1977, respectively. *Voyager 1* has been climbing out of the ecliptic plane since its November 1980 encounter with Saturn, while *Voyager 2* is continuing in the ecliptic towards its August 1989 encounter with Neptune (Figure 2.1). Although the planetary encounters of both *Voyagers* were an important and exciting part of their mission, this dissertation will concern itself only with cosmic ray observations gathered during the interplanetary cruise phases. These observations consist of data obtained from the Cosmic Ray Subsystems (CRSs) of *Voyager 1* and *Voyager 2*. Because both general and detailed descriptions of the instrument and electronics already exist in print (Stone *et. al.* 1977; Stillwell *et. al.* 1979; Garrard 1976), only the features important to this analysis will be presented.

Each CRS consists of The Electron Telescope (TET), four Low Energy Telescopes (LETs), and two High Energy Telescopes (HETs). The TET is an electron energy-spectrometer effective in the energy range from $\sim$5 to 110 MeV, and is not used in this analysis. The four nominally identical LETs measure the kinetic energy and nuclear charge, Z, of particles with $1 \leq Z \leq 30$ and kinetic energies of a few MeV/nucleon ($\sim$3 - 8 MeV/nucleon for H and He). The two High Energy Telescopes measure Z and the kinetic energy of nuclei with $1 \leq Z \leq 30$ and kinetic energies between a few MeV/nucleon and a few hundred MeV/nucleon. In addition, individual isotopes can be resolved for elements from hydrogen through oxygen. The analysis of the HET events

is the key component of the observations in this analysis.

2.1.1. The High Energy Telescope System

Each *Voyager* spacecraft carries two nominally identical HETs, denoted HET 1 and HET 2. Each HET (Figure 2.2) is a double-ended telescope consisting of two thin surface barrier solid-state detectors (A1 and A2), which define the aperture at one end, two curved Li-drifted solid-state detectors (B1 and B2) at the other end, and a stack of seven double-grooved Li-drifted detectors in the middle. The B1 and B2 detectors are curved to minimize variations in particle path length. The central portion of one of the double-grooved detectors is labelled element C1, and the other six central portions are paired into three detector elements: C2, C3, and C4. The area between the grooves forms annular detectors around each central area. The combination of the seven annular detectors constitutes a cylindrical anticoincidence or guard detector, denoted G, surrounding C1 through C4.

Particles that enter the telescope through A1 and stop in the stack are identified using the guard and C4 as an anticoincidence cup. These events are labelled A-Stopping and are illustrated by trajectory AS in Figure 2.2. Particles from the B end of the telescope are determined with anticoincidence conditions on G and C1. These "B-Stopping" particles are represented by trajectory BS in Figure 2.2. Entering from both ends of the telescope are higher energy particles, which penetrate the entire C stack, portrayed in Figure 2.2 as trajectory P. At the highest energies, the direction of penetrating particles is not distinguishable, because the particles do not slow down sufficiently in the telescope. This problem will be discussed later, in §2.4.3.

Because there are only three digital pulse heights available for each event, the energy losses in some of the detectors are added together before digitization. Table 2.1

Figure 2.1

(a) Spacecraft trajectories projected onto the ecliptic plane. (b) Spacecraft trajectories mapped into a common meridian plane. The horizontal axis is the ecliptic plane. Distances are in astronomical units. Both (a) and (b) are from Stone (1987).

Figure 2.1

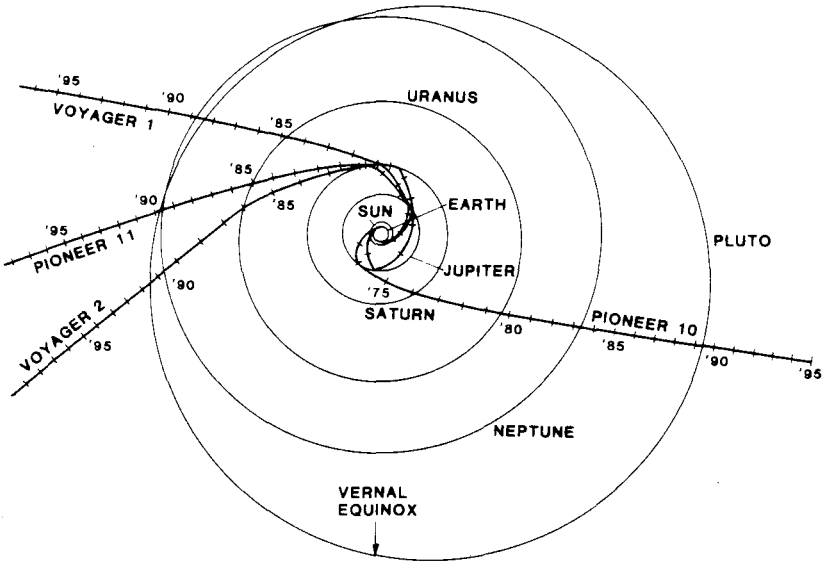
'95
'90
VOYAGER 1
'85
URANUS
'85
'90
'85
SUN
EARTH
'95
PIONEER 11
PLUTO
JUPITER
'90
'75
SATURN
VOYAGER 2
'95
'80
PIONEER 10
'85
'90
'95
NEPTUNE
VERNAL
EQUINOX

(a)

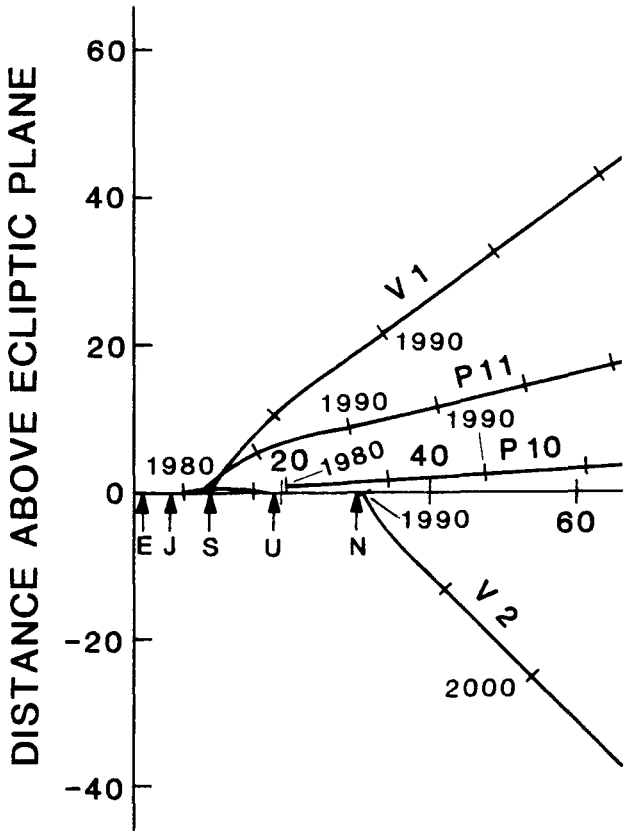
DISTANCE ABOVE ECLIPTIC PLANE
60
40
20
0
-20
-40
V1
1990
P11
1990
1990
1980
20
1980
40
P10
1990
60
E
J
S
U
N
V2
2000

(b)

Figure 2.2

Schematic cross section of the *Voyager* High Energy Telescopes in the Cosmic Ray Subsystem. The three possible classes of trajectories are illustrated as AS (A-Stopping particles), BS (B-Stopping) and P (Penetrating) (from Cook 1981).

Figure 2.2

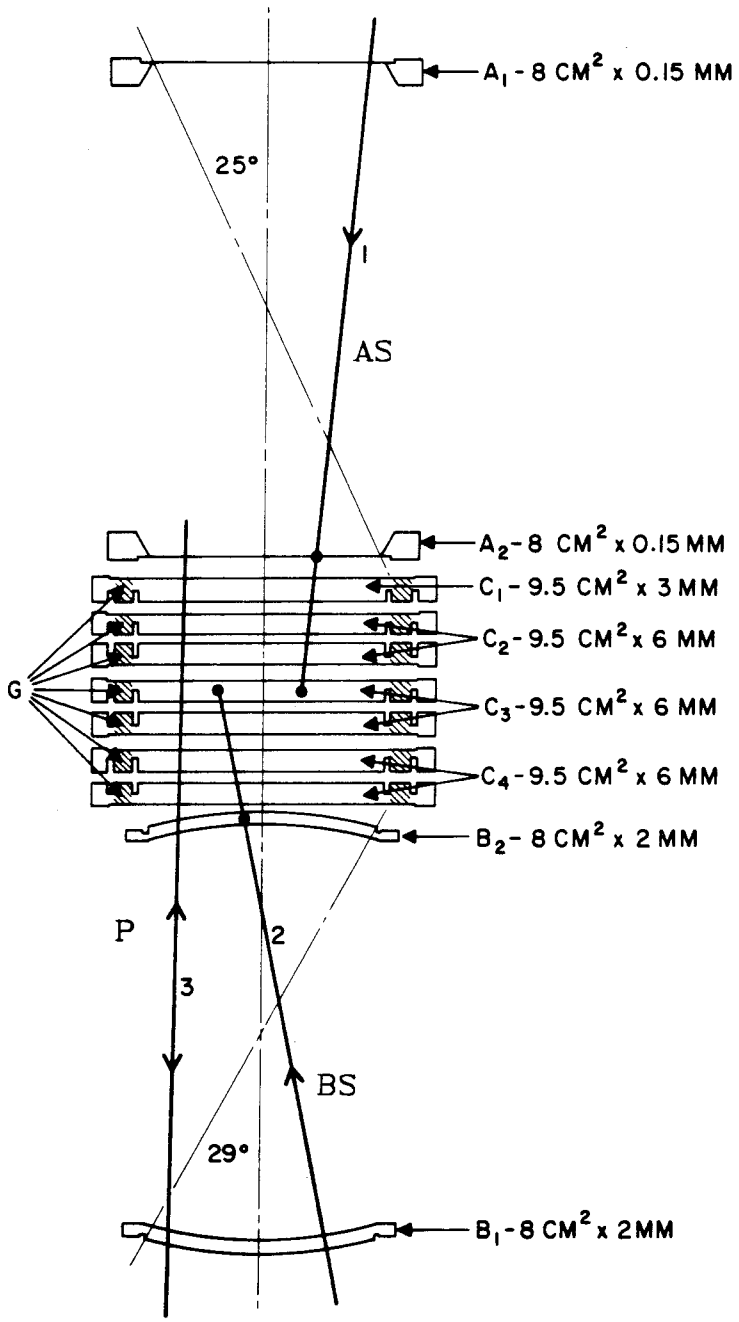

HIGH ENERGY TELESCOPE (HET)

shows which detectors are pulse-height analyzed for each of the three modes.

Table 2.1			
Mode	PHA 1	PHA 2	PHA 3
A-Stopping	C1 + C2 + C3	A2	A1
B-Stopping	B1	B2	C2 + C3 + C4
Penetrating	B1	C1	C2 + C3 + C4

Table 2.1 Pulse-Height Analyzed Detectors

2.2. Analysis Method

This section will describe a method for determining charge (Z), mass (A), and the initial kinetic energy (E) for a particle traversing a detector with at least two pulse-height analyzed ΔE measurements. First there will be a brief general discussion of the method, followed by a detailed description of the analysis of *Voyager* High Energy Telescope (HET) events using this procedure.

For a particle of given Z, A, and E, going through a stack of n detectors, a point can be plotted in an n-dimensional space, where each coordinate (i) is the energy (ΔE_i) deposited in the i-th detector. When Z and A are fixed and E is varied, a track is traced out in this n-dimensional space. In reality, events are going to be spread in n-space about this track due to Landau fluctuations, variations in incident angle, electronics noise, etc. Ideally, for any event of given Z and A, the most likely initial energy would be that energy corresponding to the point on the theoretical track closest to the point for the event, and the distance (r) between the event and the closest point on the

track can be used as a measure of how "good" the event is. Each coordinate should be properly scaled by its respective fluctuation ($\sigma_{\Delta E_i}$), so:

$$r^2 = \sum_{i=1}^{n} \frac{(\Delta E_i - \Delta \epsilon_i)^2}{\sigma^2_{\Delta E_i}} \quad , \tag{2.1}$$

where $\Delta \epsilon_i$ is the theoretical energy loss in the i-th detector, i.e., the i-th coordinate of the closest point on the track. Events on the track can then be discriminated from background events by selecting events with r less than a certain value. Note that $r = 1$ defines events that are one sigma from the theoretical track.

Certain regions of the track will have to be left out of the analysis due to ambiguities arising from crossing tracks. This crossing of tracks can occur between tracks of different Z and A, and for different energy regions of the same track.

There are also complications due to the dependence of energy loss, dE/dx, on energy. After a steep decrease in dE/dx with increasing energy, there is a minimum value of the energy loss at the "minimum ionizing energy" and then a slow increase (the relativistic rise). Because of this shape, there is a region of incident energies from slightly less than minimum ionizing on up for which the track is completely ambiguous, unless there is sufficient mass to slow the particles down below minimum ionizing. This effect is what determines the upper limit of incident energies in this analysis.

In practice, determination of r and E is not this easy. The solid-state detectors on *Voyager* contain "dead layers" in which the energy deposited is not added into the pulse-height analysis. The dead layers arise from the method of construction of Li-drifted solid state detectors. This causes an offset in the track for particles that penetrate these dead layers, as can be seen in Figure 2.3, which shows A-Stopping ^{1}H, ^{2}H, ^{3}He, and ^{4}He theoretical tracks projected onto the plane formed by the energy loss

Figure 2.3

Theoretical energy loss tracks of ^{1}H, ^{2}H, ^{3}He, and ^{4}He projected onto the plane formed by the energy loss in two of the three pulse-height analyzed detectors. The initial kinetic energy increases to the right along the track. The expanded region shows the break in the track caused by dead layers (layers in which the energy loss cannot be measured). The curve shows the approximation used to smooth the breaks.

Figure 2.3

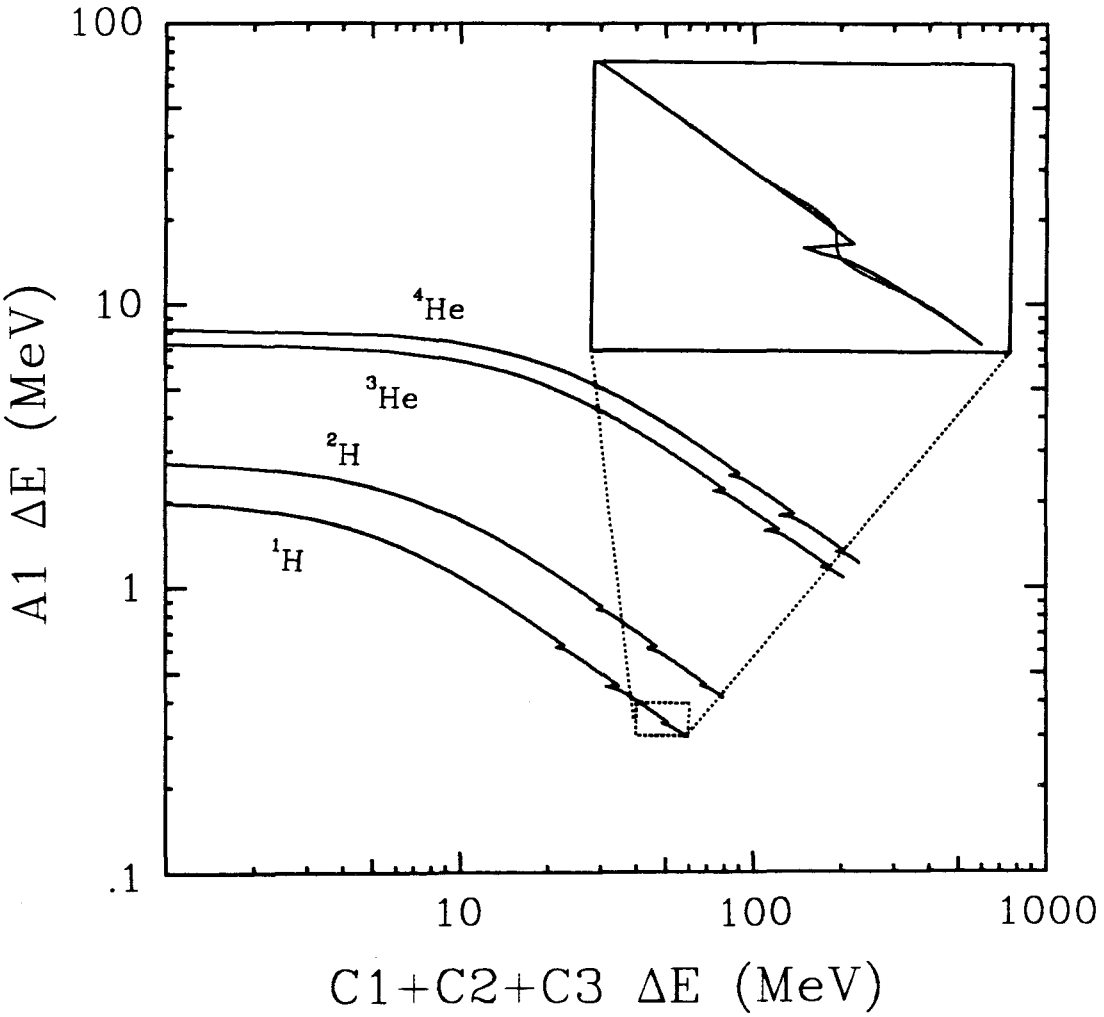

in two of the three pulse-height analyzed detectors. Because the dead layers are thin ($\sim$150 μm), this problem affects only particles in a small energy range (a few MeV/nucleon), smaller than the final energy resolution. However, these breaks cause the calculation of E to be analytically difficult. This is further complicated by the fact that the $\sigma_{\Delta E_i}$ are not analytically known. To avoid these difficulties, a computationally simpler procedure has been used, which roughly approximates the correct r and E calculation.

If one differentiates between particles that stop in a given detector and particles that fully penetrate the detector, and if dead layers are neglected, then for a given Z and A, the energy deposited in the detector is a monotonic function of the initial energy, with the ΔE monotonically increasing with increasing energy for stopping particles, and decreasing with increasing energy for penetrating particles, ignoring particles with incident energies more than the minimum ionizing energy. Therefore, taking each of these cases separately, the value of the initial energy is a direct function of the ΔE. There is, however, a maximum theoretical ΔE for a particle, which corresponds to stopping at the end of the detector. If the measured ΔE is greater than the maximum, the initial energy calculated will be outside the range of the analysis and so the event will be disregarded. Because the fluctuations can cause the particles near the end of range to deposit a ΔE greater than the maximum, the actual initial energy range must be narrowed so that it does not include particles too near the end of range.

The *Voyager* High Energy Telescopes have three detectors or stacks of detectors that are pulse-height analyzed for each event and these three pulse heights give three independent values of the initial energy, E, for each event, if Z and A are assumed. Then, the average of the three E_i (or more correctly, a weighted average) is approximately the closest E on the theoretical track, and the variance of the E_i, σ_E^2, as given

by $\Sigma (E_i - E_{avg})^2$ is a measure of how close the point is to the theoretical track, and so can be used to select events.

One problem with this is the breaks in the ΔE vs. E curves caused by the dead layers. This was resolved by artificially smoothing the curves so that the ΔE_i are always monotonic functions of E. The smoothing is acceptable because the energy region affected (stopping in the dead layers) is smaller than the energy resolution. This also allowed the analysis to use pre-written fast cubic-spline interpolation routines, which require monotonic functions. The expanded region in Figure 2.3 shows the theoretical track for ^{1}H around one of the dead-layer breaks and the artificial smoothing that was used.

Another problem arises due to the fact that, in regions where the slope, $\delta \Delta E_i / \delta E_i$, is small, a small fluctuation in ΔE_i causes a large shift in E_i, and therefore in E_{avg} and in the variance, σ_E^2. Because of this, another variance, $\sigma_{\Delta E}^2$, is calculated from $\Sigma (\Delta \epsilon_i - \Delta E_i)^2$, where the three $\Delta \epsilon_i$ are the nominal theoretical values for ΔE_i given an initial energy E_{avg}. The variance works well as a measure of the distance from the event to the theoretical track in the region where $\delta \Delta E_i / \delta E_i$ is small, but not in the region where it is large. By using a combination of both variances, σ_E^2 and $\sigma_{\Delta E}^2$, the appropriate events can be selected across the entire energy range. The cut using both variances was determined empirically and will be discussed later.

2.3. Selection of Events and Preliminary Analysis

Several steps are required before calculating Z, A, and E for an event. Each event analyzed by the *Voyager* CRS returns three pulse heights and a tag word. The tag word includes information on detector triggers, the state of the guard detector, etc. Because the analysis is separate for each of the three HET trigger modes (A-Stopping,

B-Stopping, and Penetrating), the first rough selection restricts analysis to events of the correct mode. There is also a restriction on the gain of the CRS HET charge-sensitive preamplifiers. The preamplifiers can toggle between two states that differ in gain by a factor of $\sim$5, which increases the dynamic range so that elements from hydrogen up through iron can be analyzed. Because this analysis is primarily interested in hydrogen and helium, only events with the preamplifiers in the high gain (HG) mode are selected. Events that occur when the preamplifiers are switching gains, or occur during other times when the electronics are unstable, have a caution flag set, and these events are also removed from the analysis. Events that deposit more than 0.3 MeV in the guard detectors for A-Stopping and B-Stopping, and more than 2.5 MeV for Penetrating are also disregarded.

On *Voyager 1*, only HET 2 is analyzed due to an electronics problem on HET 1, and on *Voyager 2*, only HET 1 events are used because the HET 2 preamplifier alone is currently in low gain mode. Although the other HETs are usable early in the *Voyager* flights, the time required to include the extra geometry from their analysis is prohibitive. At this step, wide windows on the raw pulse heights are also used to discriminate against particles far from the hydrogen and helium tracks.

The next step takes the selected events and converts the digital pulse height values into energy loss, ΔE_i, in MeV using data from pre-flight calibrations of the detectors. The digital pulse heights have a random number between 0 and 1 added to them before conversion to distribute the particles uniformly throughout the in ΔE bin. This is done because it is easier to visually analyze such factors as event density when the events are spread out.

2.4. Determination of Initial Energy

The main step in this analysis is the event by event calculation of the initial kinetic energy. This is achieved by the use of stored tables of E vs. ΔE_i that were calculated with Cook's range-energy programs (Cook 1981), which interpolate between values of the proton energy loss in silicon tabulated by Janni (1966). The Z and A scaling of the range-energy relationship is the semi-empirical form used by Heckman *et al.* (1960):

$$R(E, M, Z) = \frac{M}{Z^2} R_p \left(\frac{E}{M} \right) + M Z^{\frac{2}{3}} C \left(\frac{137\,\beta}{Z} \right) . \qquad (2.2)$$

The first term is the particle range scaled from the proton range-energy relationship (R_p) of Janni (1966) and the second term corrects for charge pickup. The function, C, was optimized for *Voyager* silicon detectors by Cook (1981).

The calculation of the E vs. ΔE_i tables requires knowledge of the thicknesses of all detectors, and all absorbing layers such as the aluminized mylar telescope windows and the dead layers. The thicknesses used were derived by Alan Cummings for an earlier analysis, and were used exactly as given to keep consistency with the previous analysis. The thicknesses of the A1 and A2 detectors and the dead layers were directly measured. The thicknesses of some of the B and C detectors were derived from flight data using the spacing between the breaks in the particle distribution tracks caused by the dead layers, and nominal thicknesses were used for detectors for which this was not done. However, the uncertainties in these values may be as large as the scatter of thicknesses used or $\sim$10%. All values have been converted into equivalent silicon thicknesses. A layer is considered active if the energy deposit in that layer is pulse-height analyzed, otherwise it is labelled as dead.

Table 2.2					
Detector	Active	Thickness (μm)			
		V1 HET 1	V1 HET 2	V2 HET 1	V2 HET 2
window	no	50.00	50.00	50.00	50.00
A1	yes	150.30	150.70	146.20	151.50
A2	yes	149.30	149.70	142.30	150.20
C1	yes	3214.00	3040.00	3035.00	3168.00
dead	no	89.30	60.60	73.90	97.50
C2	yes	3594.00	3435.00	3109.00	3427.00
dead	no	157.00	176.50	149.80	142.70
C2	yes	3280.00	3177.00	2950.00	3427.00
C3	yes	3362.00	3301.00	3018.00	3309.00
dead	no	129.30	153.00	184.70	154.00
C3	yes	3362.00	3302.00	3018.00	3309.00
C4	yes	3000.00	3300.00	3000.00	3000.00
dead	no	155.95	153.90	152.87	176.60
C4	yes	3000.00	3000.00	3000.00	3000.00
dead	no	63.60	87.21	68.74	88.80
B2	yes	2246.00	2200.00	2200.00	2200.00
B1	yes	2238.00	2200.00	2200.00	2200.00
dead	no	87.20	60.53	88.24	76.60
window	no	64.00	64.00	64.00	64.00

Table 2.2 Assumed Detector Thicknesses in μm equivalent silicon

To first order, these thickness differences look the same as gain changes in the analog to digital conversion, but the differences in thickness affect the ranges of initial energy for which a particle stops in a detector, and have second order effects in the shape of the ΔE tracks. The second order effects were too small to be seen, so these thicknesses and their appropriate energy ranges were used throughout the procedure. It should be noted, however, that there may be systematic differences between the actual incoming kinetic energy and the calculated value on the order of the uncertainties in detector thicknesses ($\sim$10% for the B and C detectors).

However, using these thicknesses to derive theoretical tracks did not correctly align the tracks with the center of the observed particle distributions. This was corrected by using multiplicative factors in the analysis programs, which modify the observed ΔE_i so that they agree with the theoretical curves. This correction was always less than 10% and was obtained by visually fitting the theoretical tracks and the particle distributions with an estimated accuracy of better than 3%. This should result only in a few percent uncertainty in particle fluxes, because the width of the tracks is large compared to 3%. This is smaller than other uncertainties in the absolute particle flux. These multiplicative corrections are also used to compensate for any drifting of the electronic gains during the eleven years of flight. These drifts are easily detected as shifts in the end-of-range points in the various modes and are in all cases less than 5% since launch (Christian 1988).

Yet these multiplicative factors were not always enough to get complete agreement. For two of the detectors the multiplicative factors needed to match theoretical and observed tracks were different for hydrogen and helium by $\sim$2%. This is probably not due to uncertainties in the detector thicknesses because errors of greater than 25%

would be required to cause the 2% effects observed. Therefore this effect is probably due to uncertainties in calibration or shifts in the offset of the analog to digital conversion. This was corrected by shifting the gains for hydrogen in the *Voyager 1* HET 2 B1 and *Voyager 2* HET 1 B1 detectors by an extra 2% with regard to the helium gains in the B-Stopping mode.

Because the exact analysis varied between the three different event modes, due to both program evolution and the tailoring of the programs to each of the modes, they will be treated separately in the following discussion of event discrimination and initial energy determination.

2.4.1. A-Stopping

Figures 2.4, 2.5, and 2.6 show the three ΔE_i vs. ΔE_j projections of *Voyager 2* HET 1 A-Stopping events during the time period 1977/337 - 361 (1977 days 337 to 361). The tracks for ^{1}H and ^{4}He are clearly visible and these isotopes can be analyzed from $\sim$7 MeV/nucleon up to a few tens of MeV/nucleon. In order to trigger as an A-Stopping event a particle must trigger A1 and A2 and not C4. This analysis also requires a trigger in detector C1 so that every event analyzed has three pulse height measurements. These events have a better background subtraction than events that have only two pulse heights. The two pulse height events are very low energy ($\sim$5 MeV/nucleon) and are not of much interest to this dissertation.

Note that the bin edges of the analog to digital conversion are visible in Figures 2.5 and 2.6 for small values of C1+C2+C3 ΔE. For these values of ΔE, the resolution of the detector is better than the resolution of the analog-to-digital converter, although the fact that the edges are sharp indicates that the binning noise is small.

Because the hydrogen and helium tracks don't cross, the areas around the hydrogen and helium tracks are analyzed separately. After rough cuts to determine Z, three initial kinetic energies, E_i, are calculated from tables of E_i vs. ΔE_i. From the three E_i, the average initial energy, E_{avg}, and the variance, σ_E^2, are calculated:

$$E_{avg} = \sum_{i=1}^{3} \frac{E_i}{3} \tag{2.3}$$

$$\sigma_E^2 = 1000 \times \sum_{i=1}^{3} \frac{(E_{avg} - E_i)^2}{E_{avg}^2} \quad . \tag{2.4}$$

E_{avg} is then taken to be E, the initial kinetic energy, and used to calculate the $\Delta\epsilon_i$ from the inverse tables, ΔE_i vs. E. The variance $\sigma_{\Delta E}^2$ is obtained from:

$$\sigma_{\Delta E}^2 = 1000 \times \sum_{i=1}^{3} \frac{(\ln(\Delta E_i) - \ln(\Delta\epsilon_i))^2}{E_{avg}^2} \quad . \tag{2.5}$$

The analysis uses the natural logs, $\ln(\Delta E_i)$ and $\ln(\Delta\epsilon_i)$, because that is what is returned by the interpolation subroutine and is thus computationally quicker. The multiplication by 1000 merely moves the two variances into a more convenient range. Note that the variance $\sigma_{\Delta E}^2$ should be more correctly normalized so that it is unitless as the variance σ_E^2 is, although this parameterization does work. Figure 2.7 shows a plot of $\sigma_{\Delta E}^2$ vs. σ_E^2 in which it can be seen that the edge of the hydrogen events is diagonal on the log-log plot. This enables the two variances to be combined into a single parameter, called r′, which can be used to discriminate events in the track from background events:

$$r' = 0.6 \times \ln(\sigma_{\Delta E}^2) + \ln(\sigma_E^2) \quad . \tag{2.6}$$

Figure 2.4

Energy loss in the A1 and A2 detectors for *Voyager 2* HET 1 A-Stopping events during the time period 1977/337 - 361. The theoretical tracks (from left to right) for ^{1}H (mostly buried in the hydrogen track), ^{2}H, ^{3}He, and ^{4}He are also included.

Figure 2.5

Energy loss in the C1+C2+C3 and A1 detectors for the events of Figure 2.4. The theoretical tracks (from bottom to top) are ^{1}H, ^{2}H, ^{3}He, ^{4}He. The steps in the track at low values of C1+C2+C3 ΔE are due to the size of the analog-to-digital-conversion bins.

Figure 2.6

The events of Figure 2.4 projected onto the C1+C2+C3 ΔE vs. A2 ΔE plane. The steps in the track at low values of C1+C2+C3 ΔE are due to the size of the analog-to-digital-conversion bins.

Figure 2.4

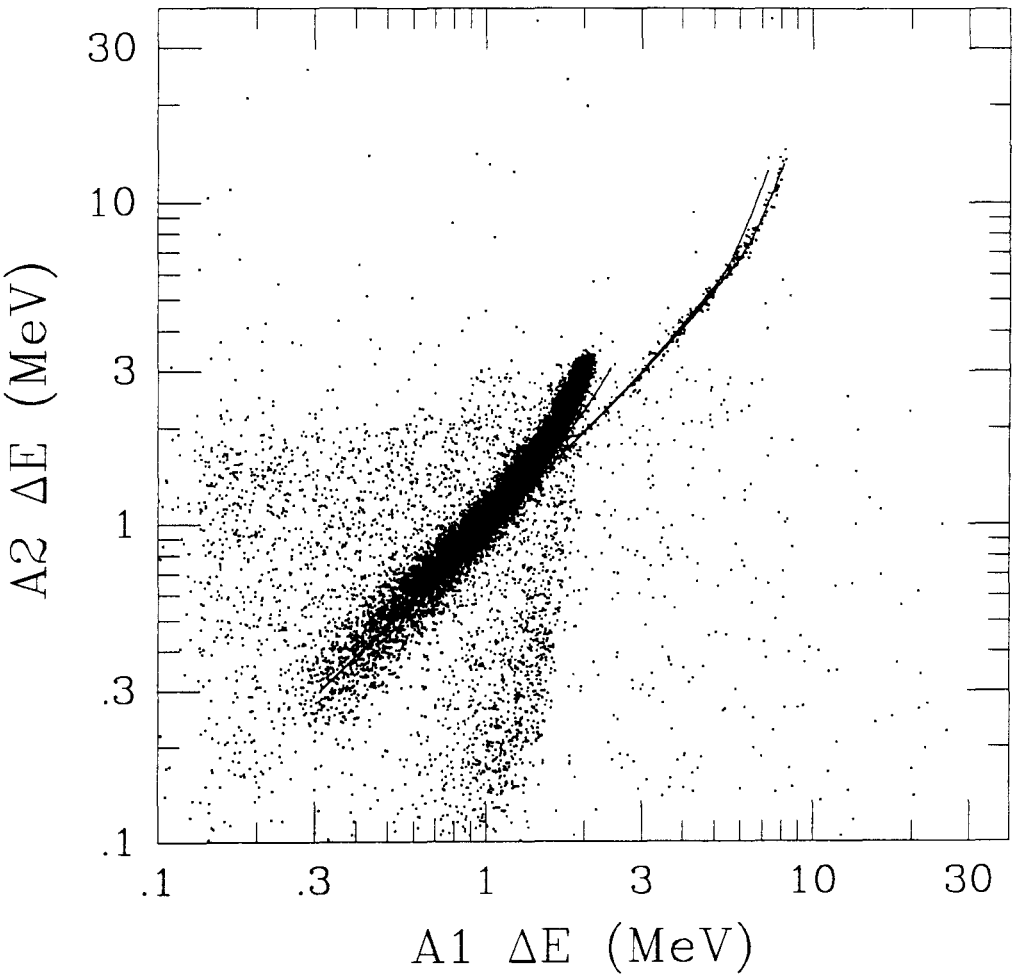

Figure 2.5

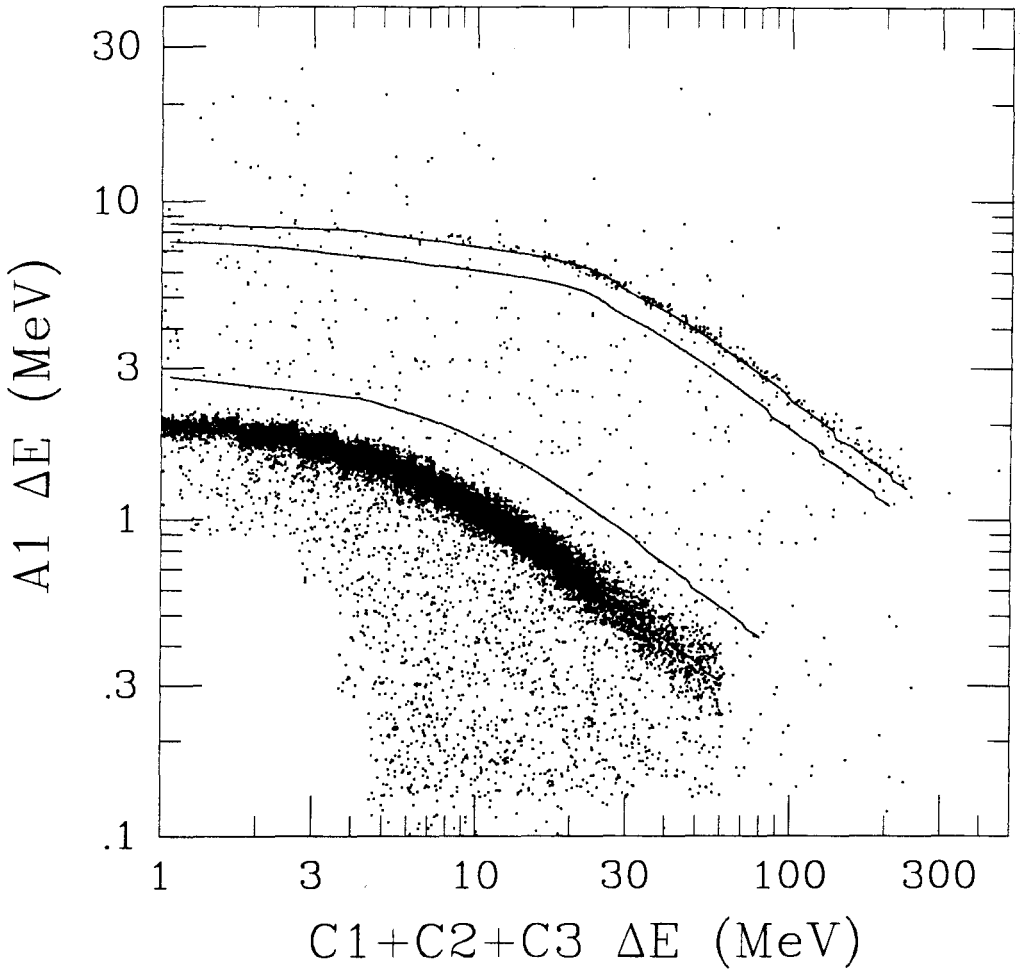

Figure 2.6

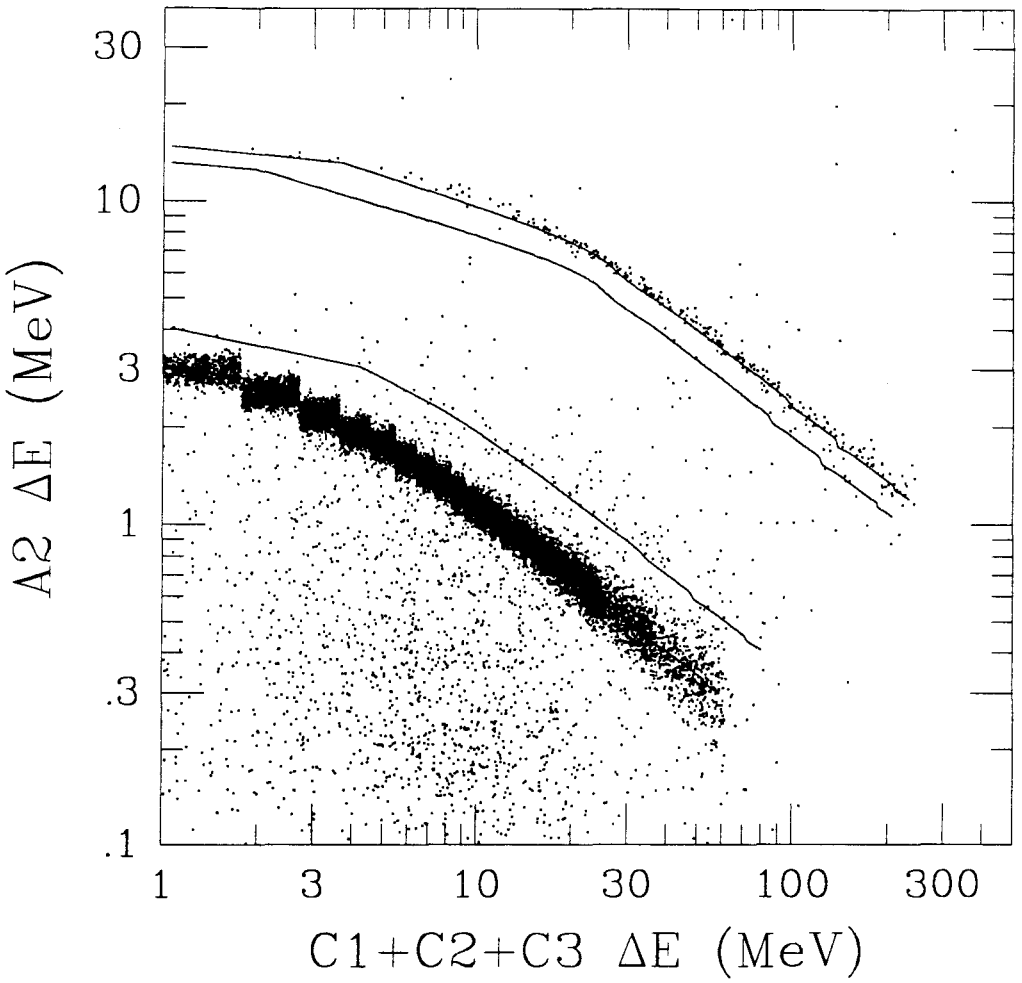

Figure 2.7

$\sigma^2_{\Delta E}$ vs. σ^2_E for *Voyager 2* HET 1 A-Stopping events from 1977/335-361 assuming the events to be ^1H. The dashed line separates the ^1H events from any ^2H events. The parameter, r', is measured perpendicular to the dashed line.

Figure 2.7

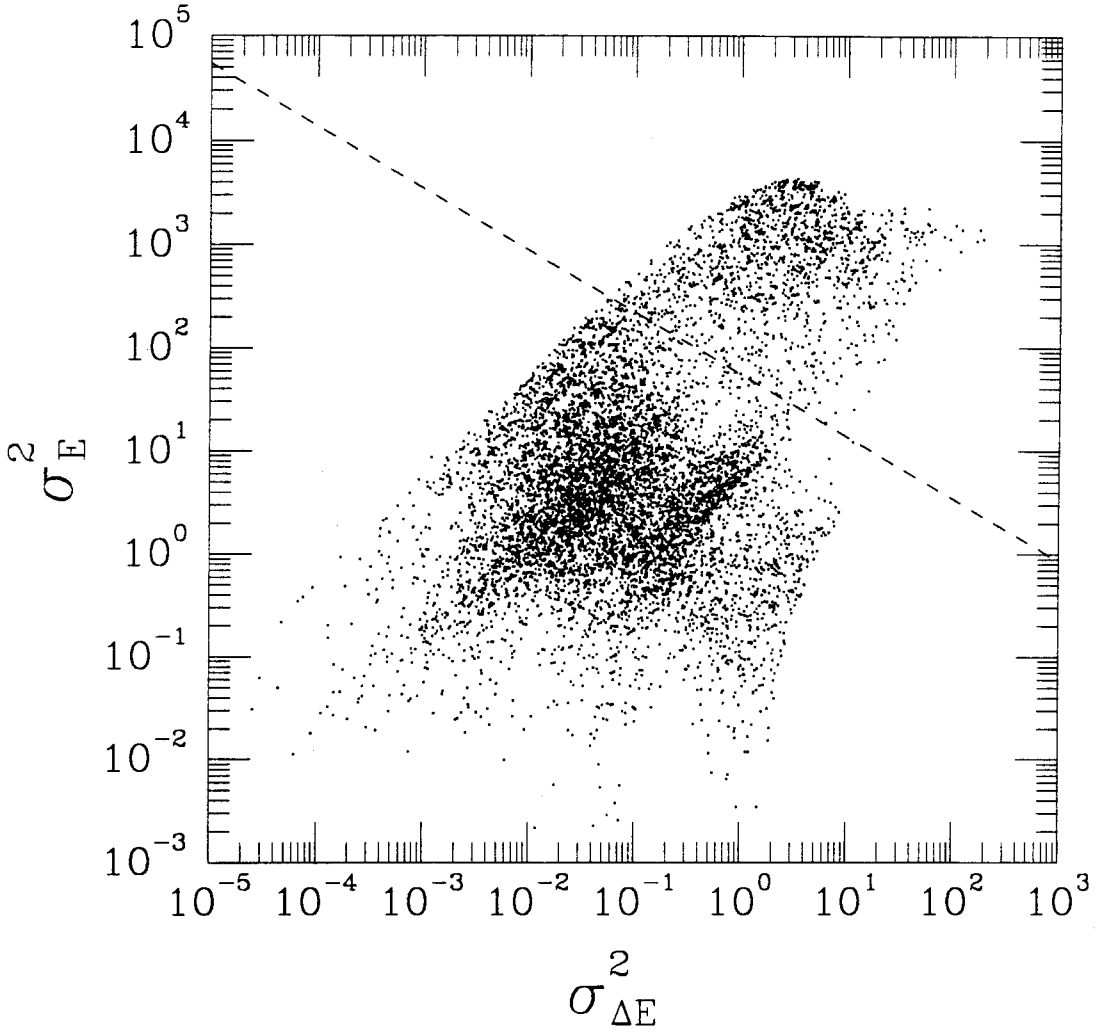
10^5
10^4
10^3
10^2
10^1
10^0
10^{-1}
10^{-2}
10^{-3}
σ^2_E
10^{-5} 10^{-4} 10^{-3} 10^{-2} 10^{-1} 10^0 10^1 10^2 10^3
$\sigma^2_{\Delta E}$

Figure 2.8 shows the histogram of r' for particles near the hydrogen tracks, assuming that the particles are ^1H.

When this analysis was begun, there was hope that primary ^2H and ^3He could also be analyzed. Because of this, events near the hydrogen track have r' calculated for ^1H and ^2H independently. The mass is determined by which of the two isotopes has the minimum r'. This is done for ^3He and ^4He as well. Background particles are discriminated against by restricting events to those with $r' < r_{max}$, where r_{max} is obtained from the r' histograms such as Figure 2.8.

In practice, the deuterium and ^3He primary fluxes were too small to be usefully analyzed because of the ^1H and ^4He backgrounds. However, the r_{max} used for ^1H and ^4He still reflect this attempt to analyze the less abundant isotopes and are set so that particles with the same charge but one amu different in mass will be discriminated against.

Figures 2.9, 2.10, and 2.11 show the events of Figures 2.4, 2.5, and 2.6 separated into good events (top) and background (bottom). Good events are those that will be included in the subsequent flux calculations. In the background events of Figures 2.10 and 2.11 there are particles that appear to be in the hydrogen track in these two-dimensional projections. These are events that appear either below or to the left of the hydrogen track of Figure 2.9 and are mostly due to events that pass near the edges of the A1 and A2 detectors and thus give incorrect measurements of the energy deposited. The geometry factors used have been reduced to reflect this loss of effective area (see §2.5).

In Figure 2.11 there are also background events in the hydrogen track, which are secondaries created in the mass above A2. A helium track is also observable in the background events of Figure 2.11 due to these secondaries. Using three pulse heights

enables the analysis to discriminate against these types of events.

2.4.2. B-Stopping

B-Stopping events require triggers in detectors B1 and B2 and no trigger in detector C1. Figures 2.12, 2.13, and 2.14 show the two-dimensional projections in ΔE space for B-Stopping particles with the theoretical tracks for ^{1}H, ^{2}H, ^{3}He, and ^{4}He. In Figure 2.12 the events that trigger B1 and B2 but not C4 are seen as the portion of the tracks in which the energy deposited in B2 is decreasing (as the particles stop earlier in B2) while the energy deposited in B1 is increasing. These events are at energies that are already covered in the A-Stopping analysis. As with the A-Stopping mode, these two pulse height events are not included in this analysis, so effectively events must also trigger C4.

Because the B1 detector is more than ten times as thick as detector A1, there are correspondingly more secondaries generated by fragmentation. This is apparent in Figure 2.14 because the deuterium track is clearly visible whereas it is not visible in Figure 2.13.

The analysis for B-Stopping is nearly identical to that for A-Stopping events, with r' and E_{avg} calculated as shown in Equations (2.3) through (2.6). The good ^{1}H and ^{4}He events have kinetic energies of between $\sim$29 and $\sim$73 MeV/nucleon before they enter the telescope. Figures 2.15, 2.16, and 2.17 are the events divided into accepted particles and background. Included in the background are good particles that stop in detector B2 and so are not included in this analysis.

Figure 2.8

The events of Figure 2.7 histogrammed along the direction perpendicular to the dashed line (r'). The dashed line is at r_{max}. Events with $r < r_{max}$ are accepted as good ^1H.

Figure 2.8

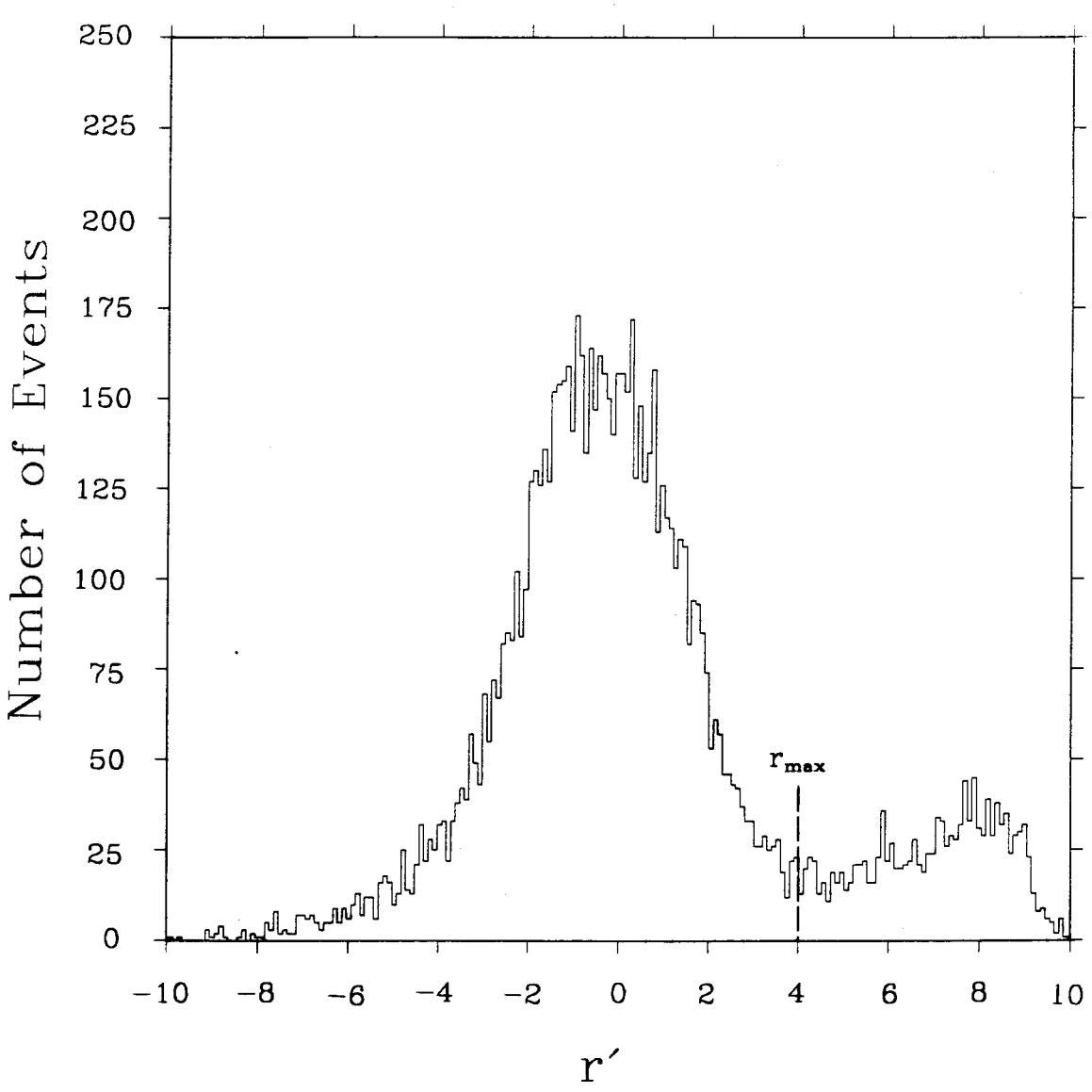
Number of Events
250
225
200
175
150
125
100
75
50
25
0
−10
−8
−6
−4
−2
0
2
4
6
8
10
r′
r_max

Figure 2.9, Figure 2.10, and Figure 2.11

Planar projections in ΔE_i space of the events in Figures 2.4 - 2.6 separated into good events (top) and background (bottom).

Figure 2.9

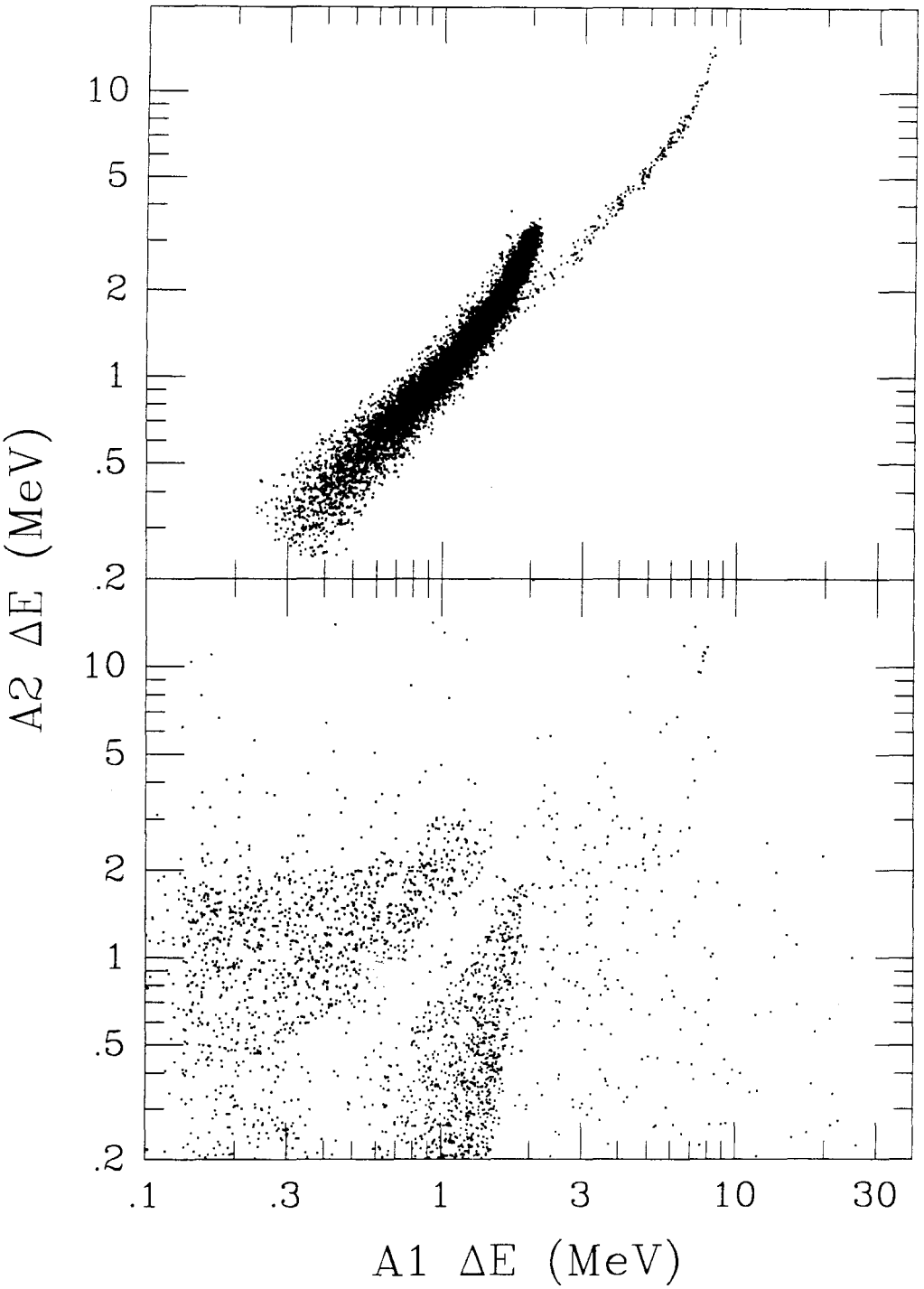

Figure 2.10

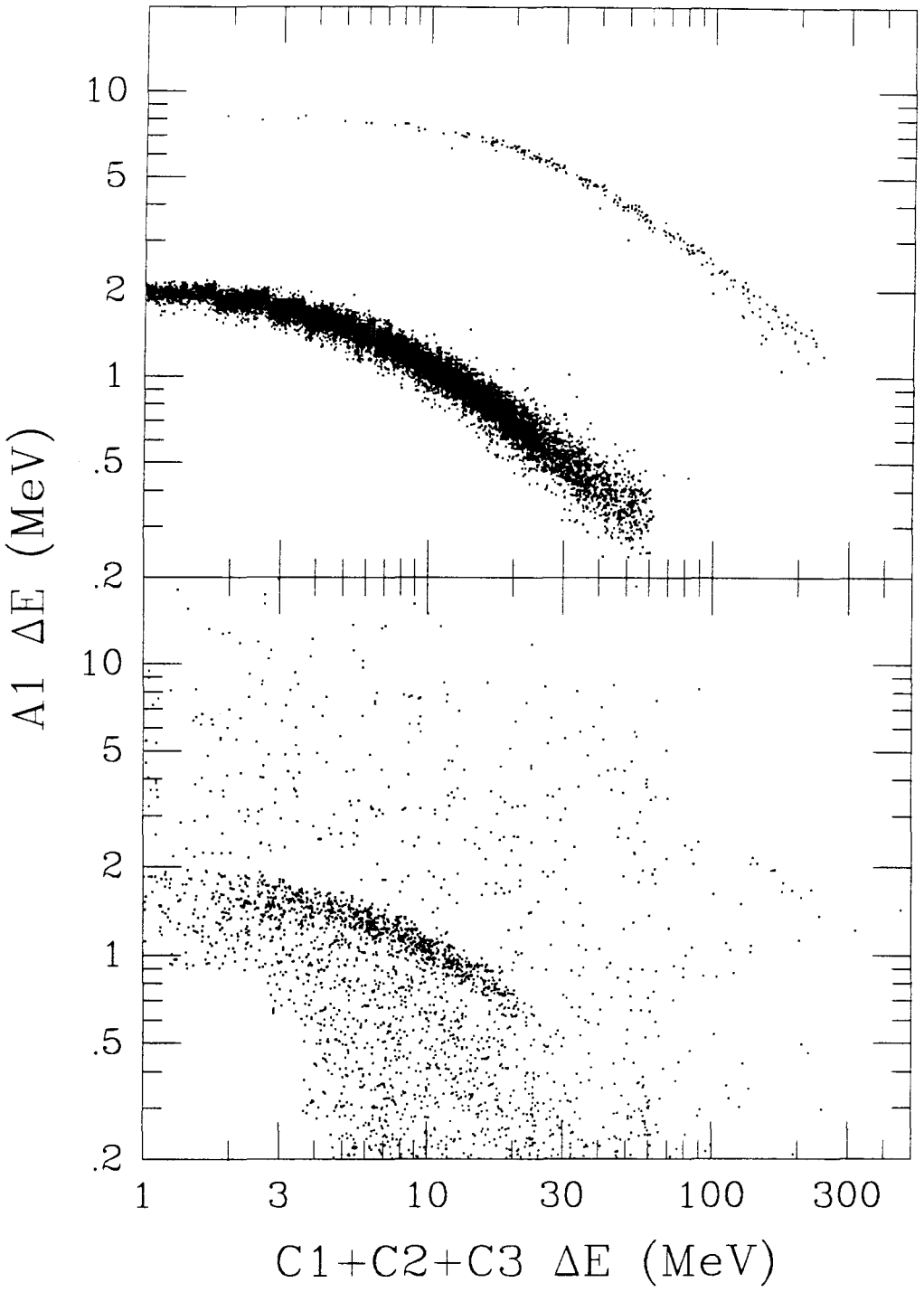

Figure 2.11

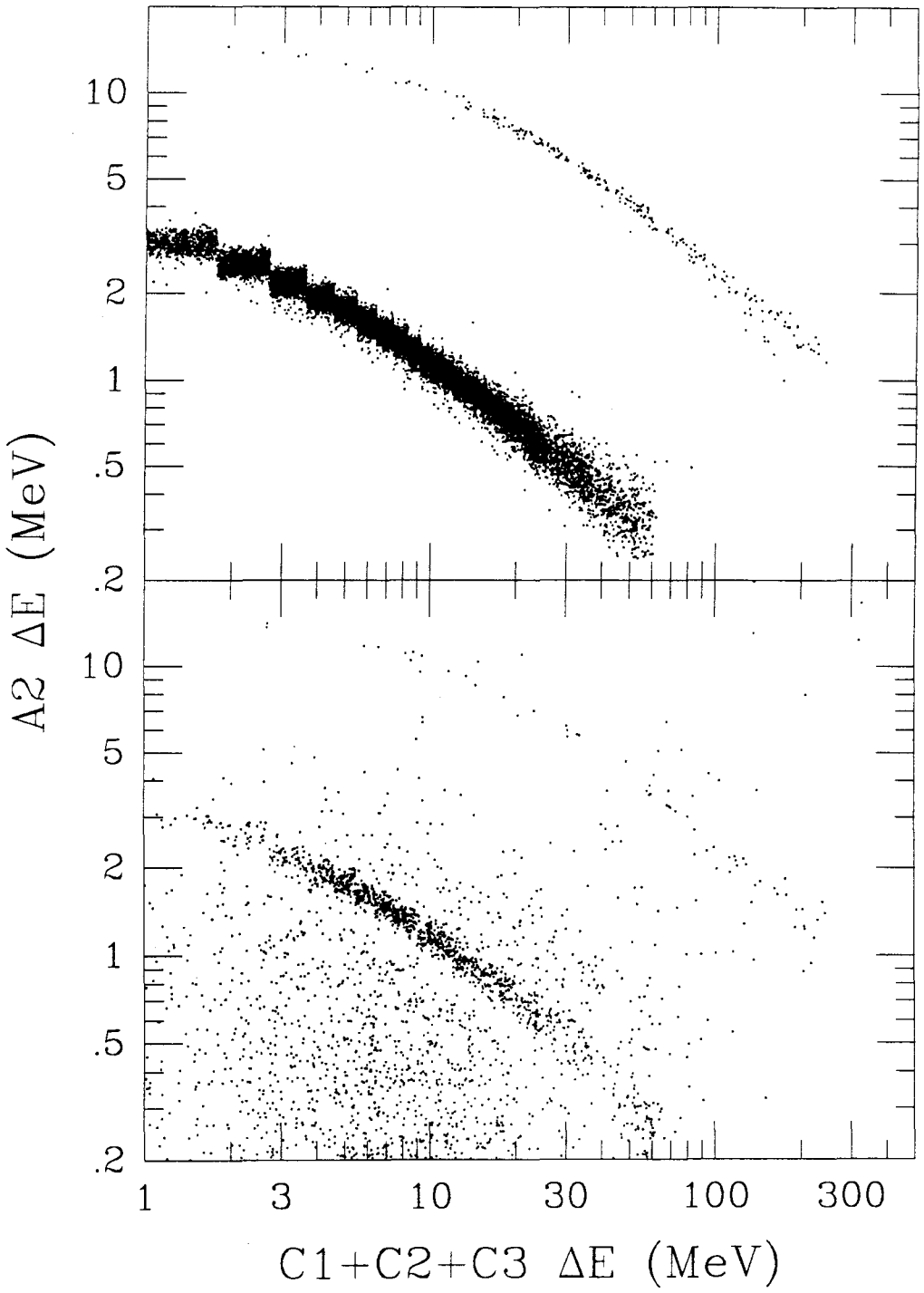

Figure 2.12

Voyager 1 HET 2 B-Stopping events from the time period 1977/335 - 361. Included are the theoretical tracks for ^{1}H, ^{2}H, ^{3}He, and ^{4}He (left to right).

Figure 2.13

Voyager 1 HET 2 B-Stopping events from the time period 1977/335 - 361. Included are the theoretical tracks for ^{1}H, ^{2}H, ^{3}He, and ^{4}He (bottom to top).

Figure 2.14

Voyager 1 HET 2 B-Stopping events from the time period 1977/335 - 361. Included are the theoretical tracks for ^{1}H, ^{2}H, ^{3}He, and ^{4}He (bottom to top).

Figure 2.12

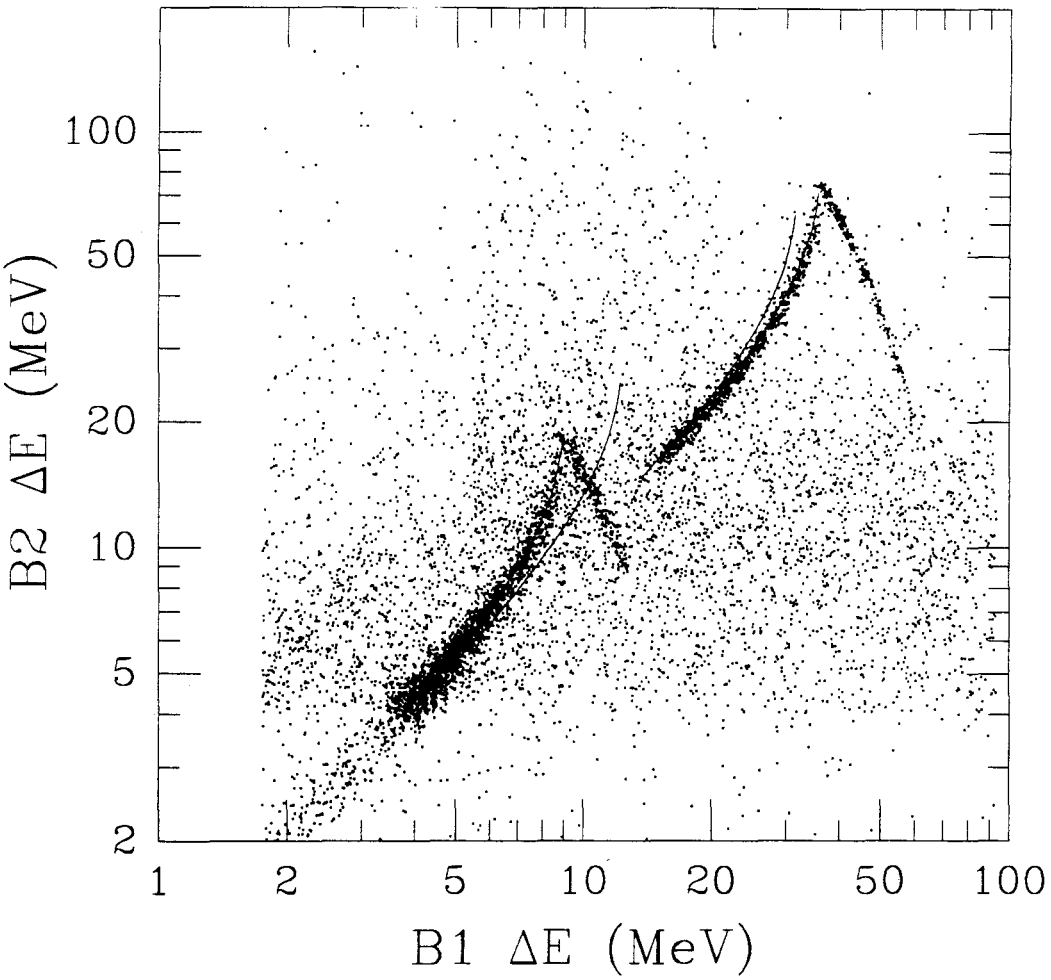

Figure 2.13

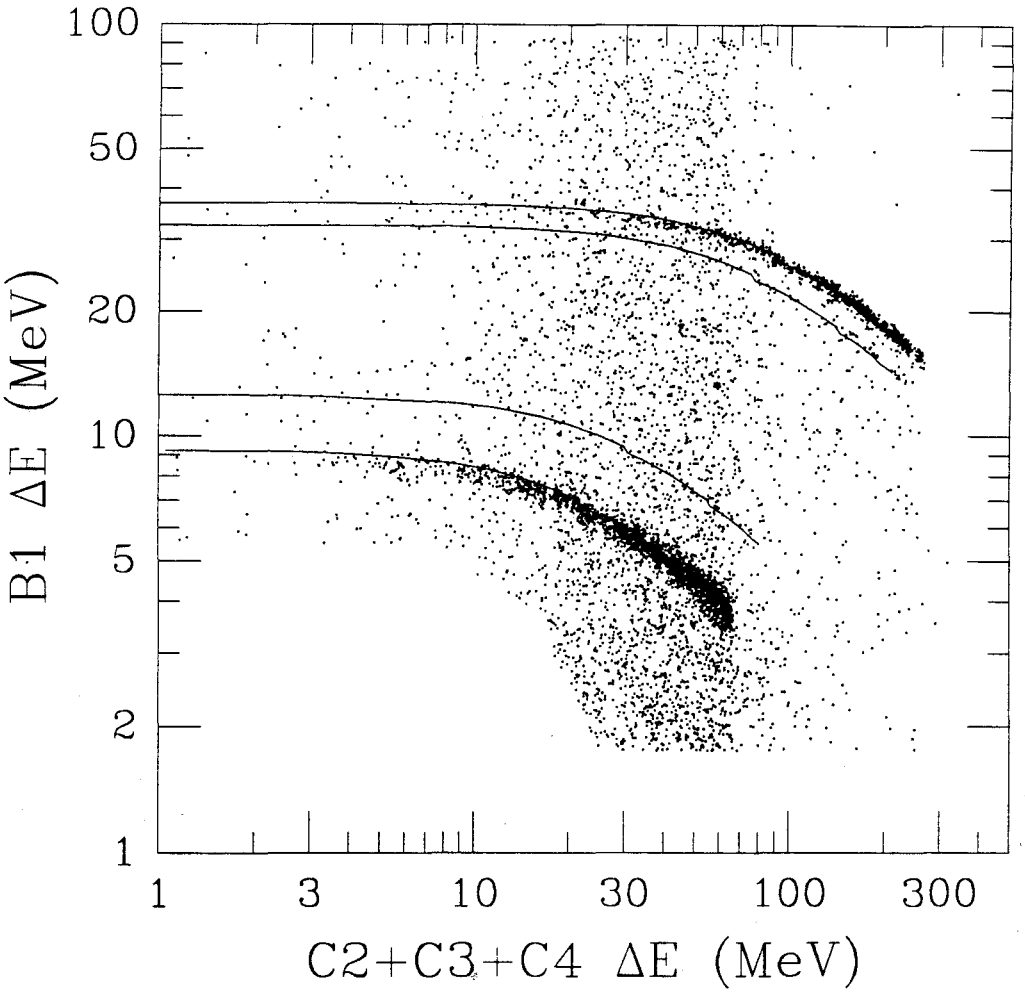

Figure 2.14

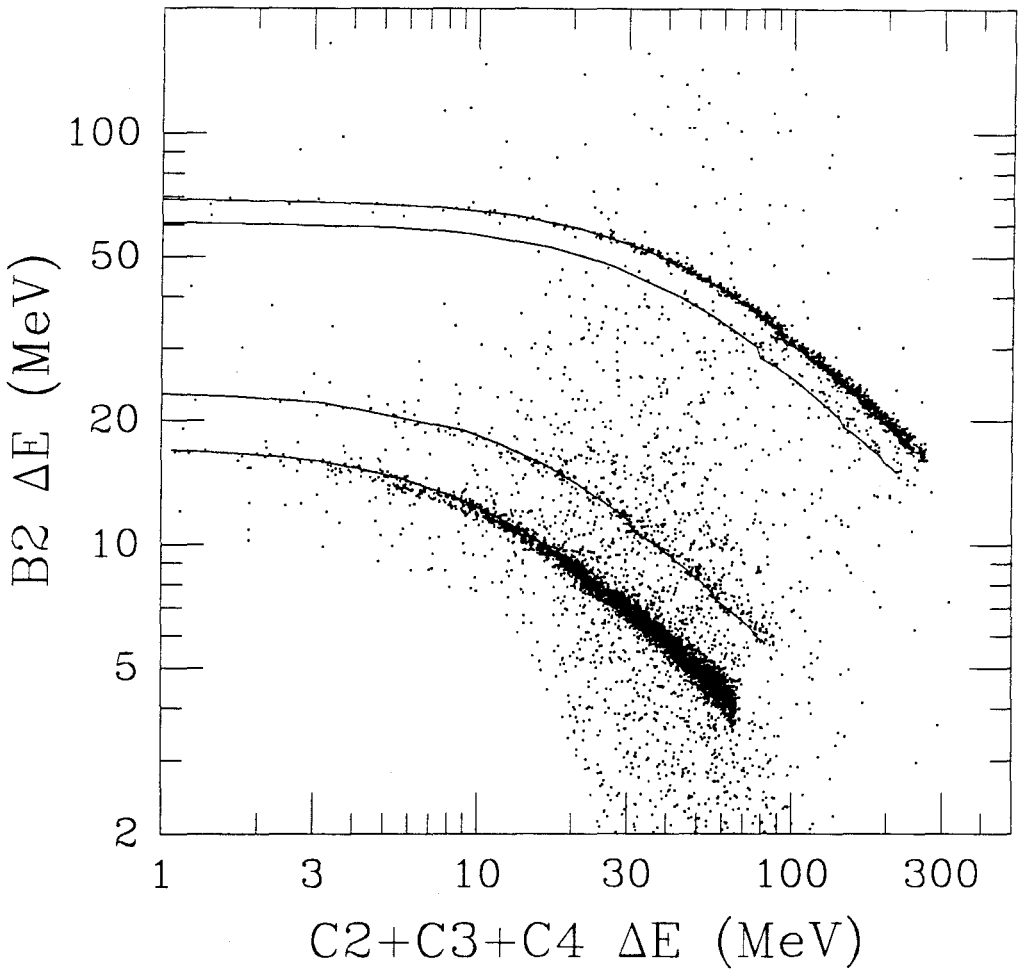

Figure 2.15, Figure 2.16, and Figure 2.17

Planar projections in ΔE_i space of the events in Figures 2.12, 2.13, and 2.14 separated into good events (top) and background (bottom).

Figure 2.15

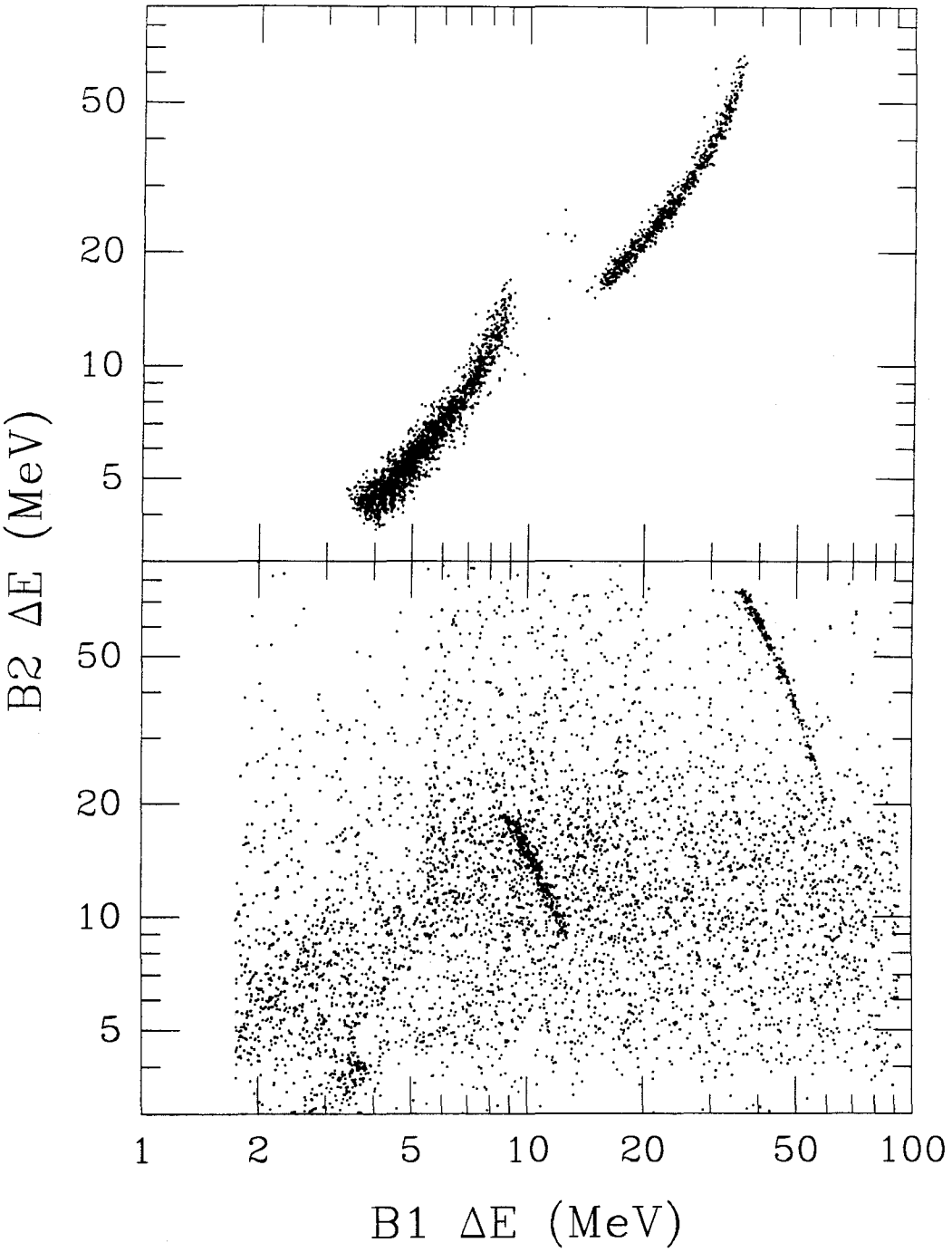

Figure 2.16

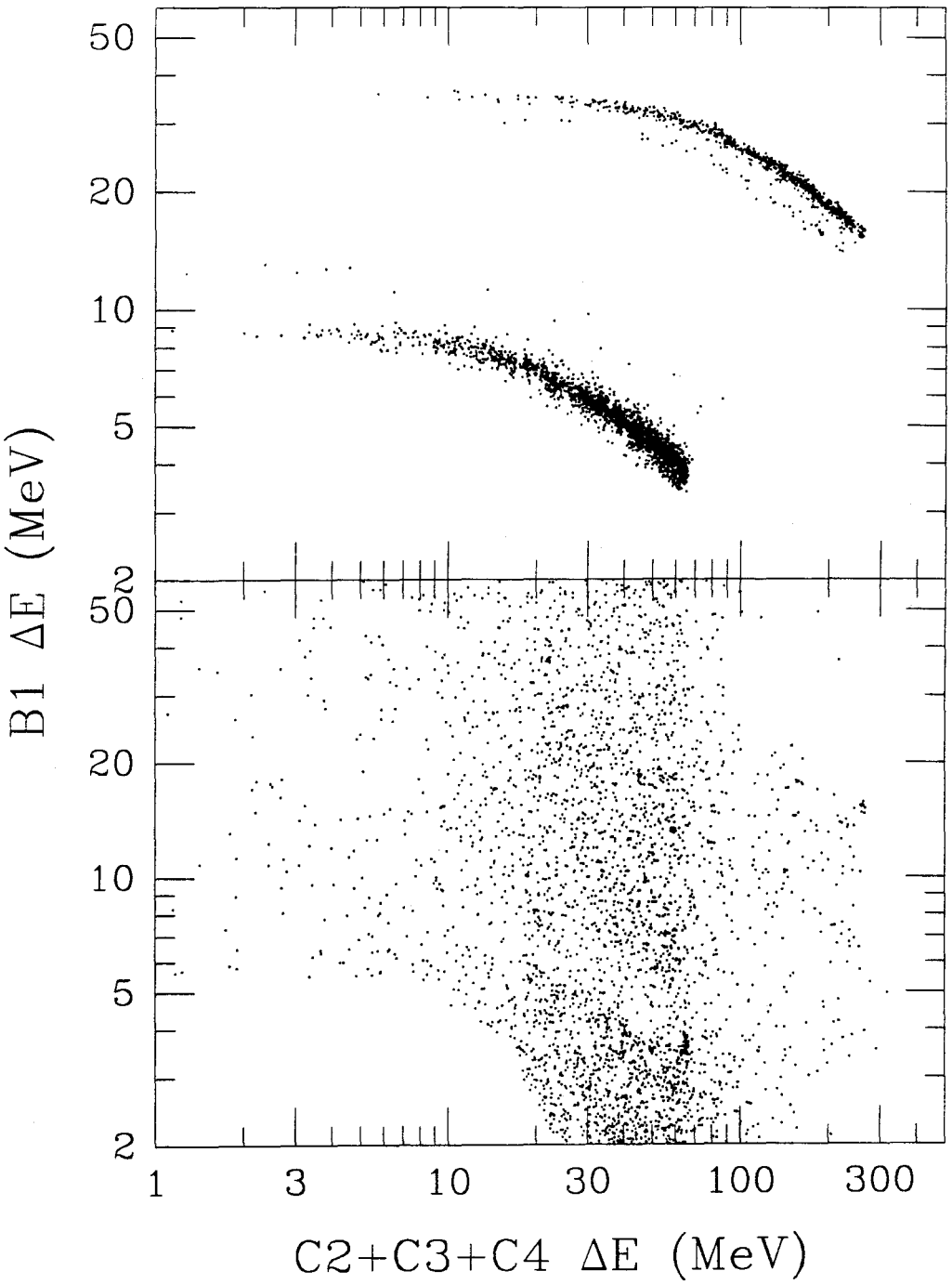

Figure 2.17

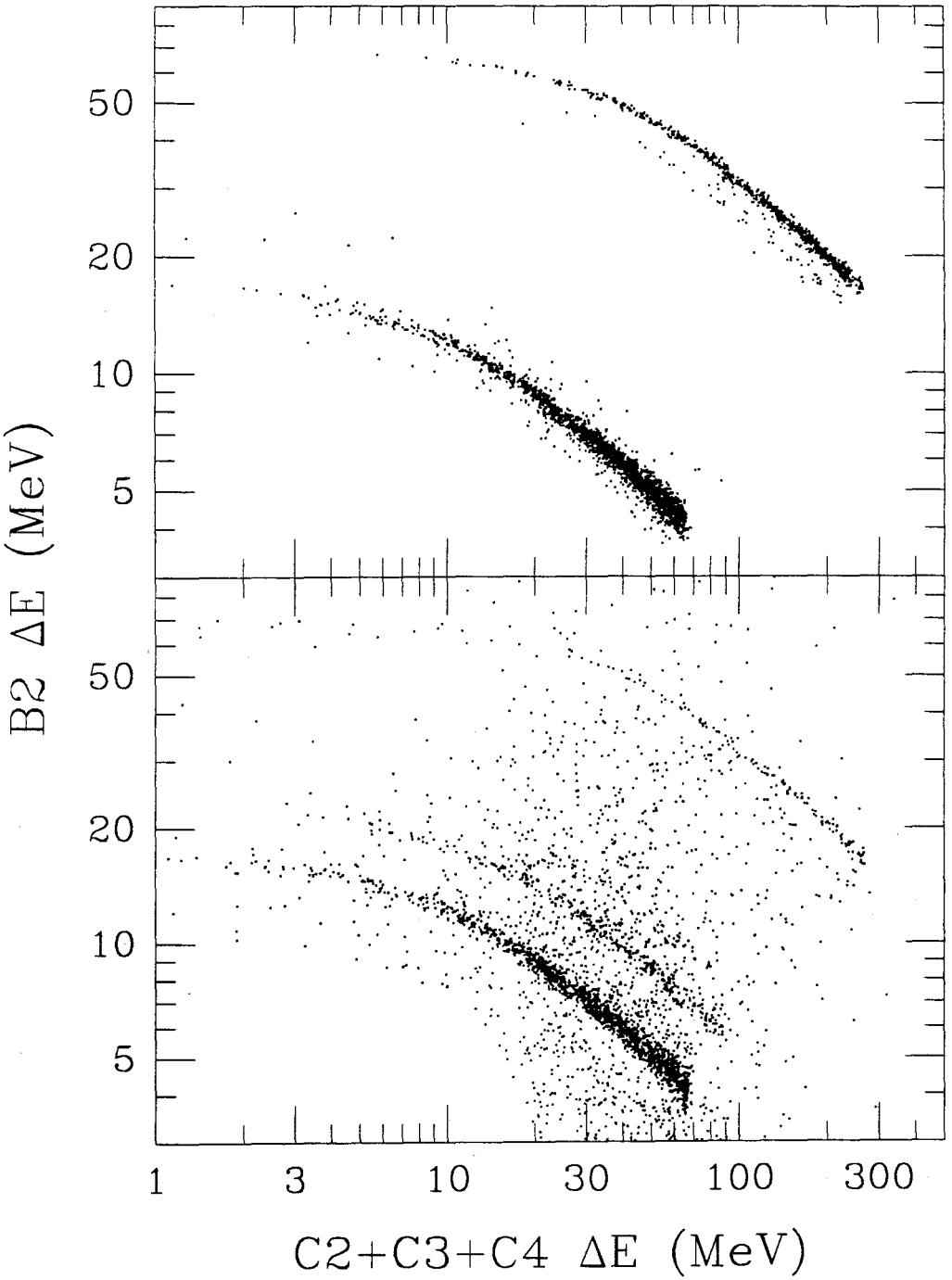

2.4.3. Penetrating

For several reasons the Penetrating mode is much more difficult to analyze than either A-Stopping or B-Stopping. One problem is the bidirectional nature of this mode. At the lower energies, the slowing down of the particle is noticeable and so the direction of the event can be determined, but at higher energies the width of the track combines events from both the A side (particles that hit detector A1 first) and the B side (particles that hit B1 first). Also, for the Penetrating mode, isotopes are indistinguishable for both hydrogen and helium because the separation of the tracks is smaller than the width. Add to this the fact that the helium high-energy (minimum ionizing) particles overwhelm a sizable portion of the hydrogen energy spectrum, and the penetrating procedure becomes much more difficult and complicated than either of the stopping modes. However, of the three, this is the one that was attempted first, and this is evident in its cruder analysis techniques.

The distribution of Penetrating events in ΔE space is shown in Figures 2.18, 2.19, and 2.20. The large concentration of events in the lower left of Figure 2.18 consists of high energy, minimum ionizing hydrogen. The minimum ionizing helium concentration, in the center, overlaps the hydrogen track in both directions. Clusters of boron and carbon high energy events can also be seen in the upper right corner, but they do not interfere with the helium track.

Because the hydrogen and helium tracks overlap, the analysis has been broken up into four regions for which unambiguous determination of Z and initial kinetic energy can be made: the lower energy portion of the hydrogen A-side track (labelled H-A on Figure 2.18) from the end of the track until just before the track is covered by the high energy helium events, the same energy region on the hydrogen B-side track (labelled H-B), the high energy part of the hydrogen track between the minimum-ionizing hydrogen

and helium concentrations, and the helium track from just beyond the minimum ionizing helium to the end of the tracks in both directions (He-A and He-B). The analysis is separate for each of the four regions with the two variances, σ_E^2 and $\sigma_{\Delta E}^2$, given by:

$$\sigma_E^2 = \sum_{i=1}^{3} \frac{(E_{avg} - E_i)^2}{E_{avg}^2} \tag{2.7}$$

$$\sigma_{\Delta E}^2 = \sum_{i=1}^{3} \frac{(\Delta E_i - \Delta \epsilon_i)^2}{E_{avg}^2} \quad , \tag{2.8}$$

which are different from the stopping programs.

For the region around the helium track, variances are calculated for both possible particle directions. The initial kinetic energy is given by the direction with the smallest value of the variance $\sigma_{\Delta E}^2$. This works correctly for particles in the lower energy tails of the distribution and is acceptable in the region where the two directions are indistinguishable because the difference in E calculated for the two directions is smaller than the energy resolution resulting from the width of the distribution.

The same type of analysis is done for the higher energy hydrogen region for which the two directions are indistinguishable. The minimum energy of this analysis, 150 MeV, is set by the interference of minimum ionizing helium, and the high energy limit, 375 MeV, results from loss of resolution due to binning, as all three pulse heights are only in a few bins.

The regions around the low energy hydrogen tracks are analyzed separately. Only a small region (79 MeV to 87 MeV) is uncontaminated by helium events. The events of Figures 2.18, 2.19, and 2.20 are separated into good events and background in Figures 2.21, 2.22, and 2.23.

Figure 2.18

Energy loss in the B1 and C1 detectors for *Voyager 2* HET 1 Penetrating events. The concentration of particles at the lower left is composed of minimum ionizing (high energy) hydrogen. The hydrogen track extends up and right from this concentration and branches to the right (labelled H-A for particles coming from the A-side) and up (labelled H-B for particles from the B-side). Both tracks pass through the concentration of high energy helium events at $\sim$(3,4). The Helium-A and Helium-B tracks extend from this concentration.

Figure 2.19

Energy loss in the C2+C3+C4 and B1 detectors for the events of Figure 2.18.

Figure 2.20

The events of Figure 2.18 projected onto the C2+C3+C4 ΔE vs. C1 ΔE plane.

Figure 2.18

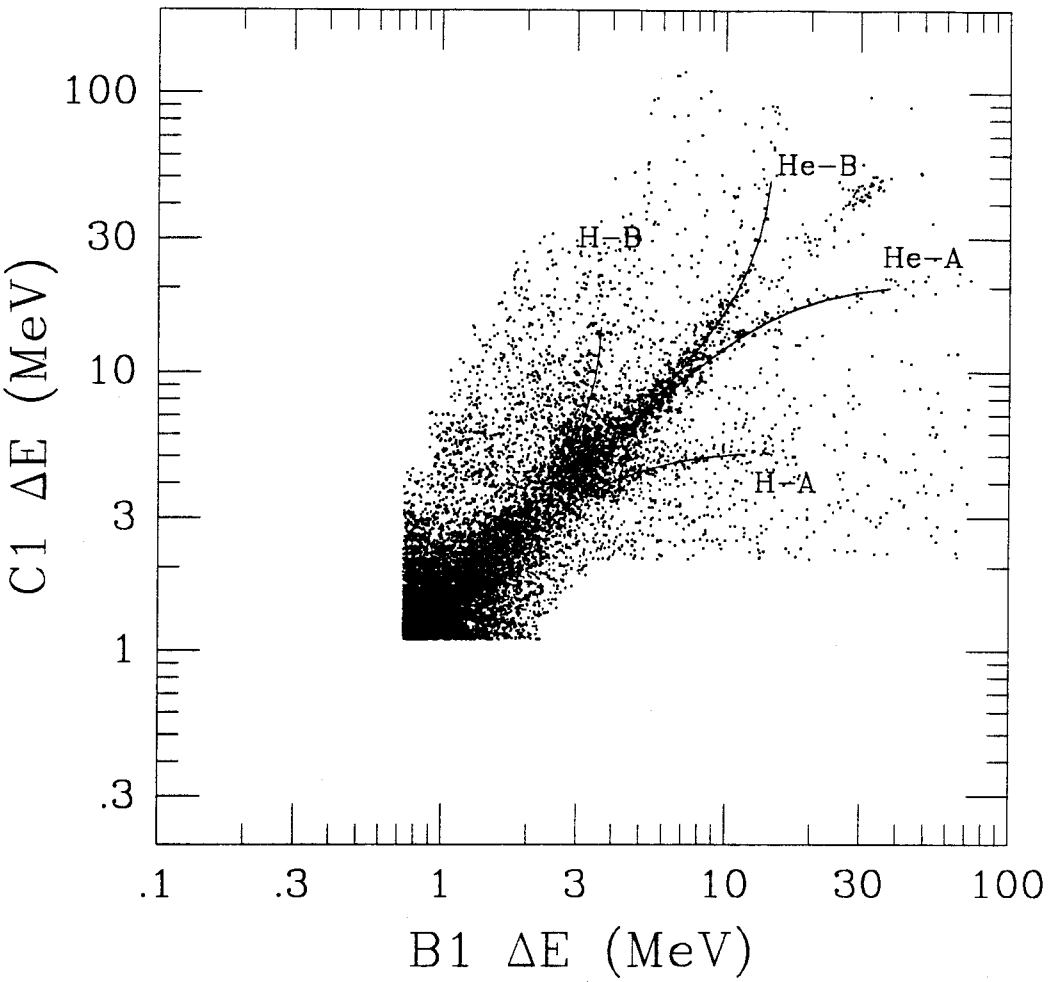

Figure 2.19

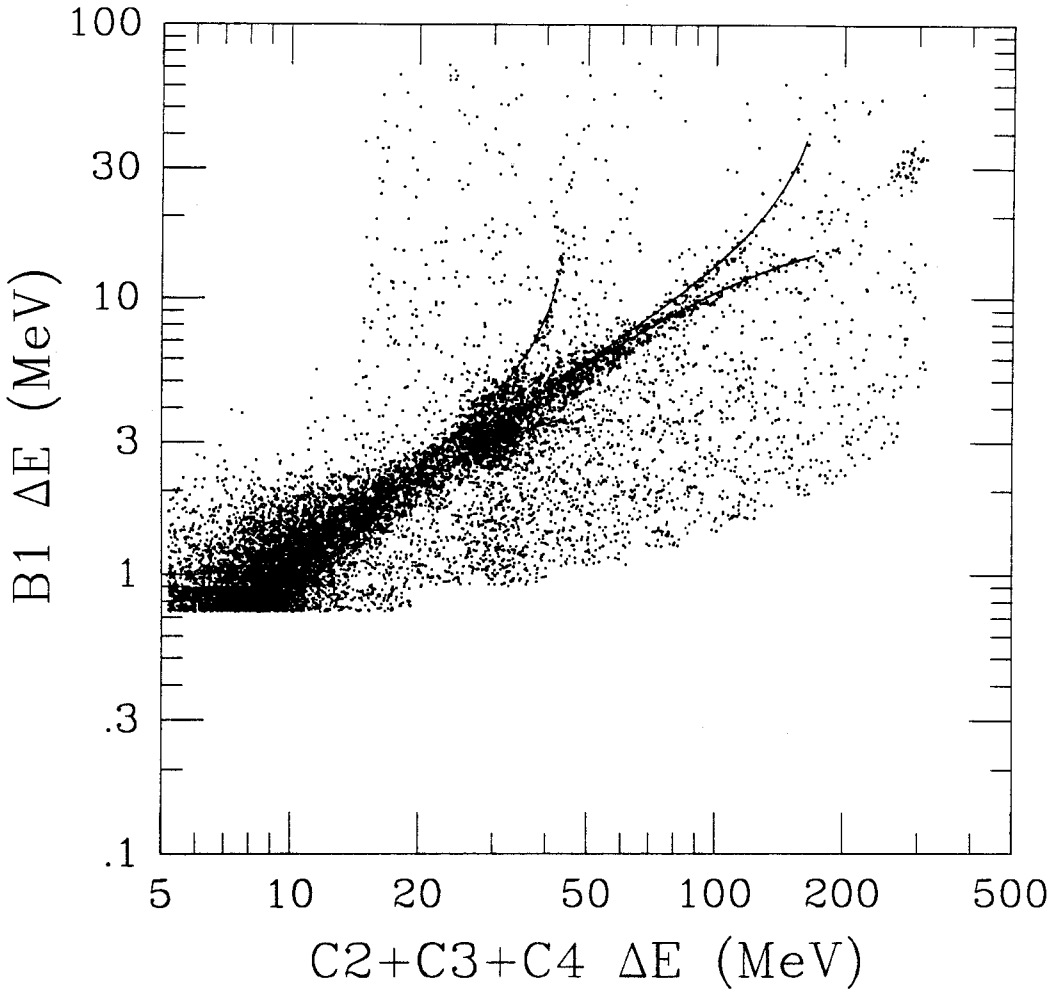

Figure 2.20

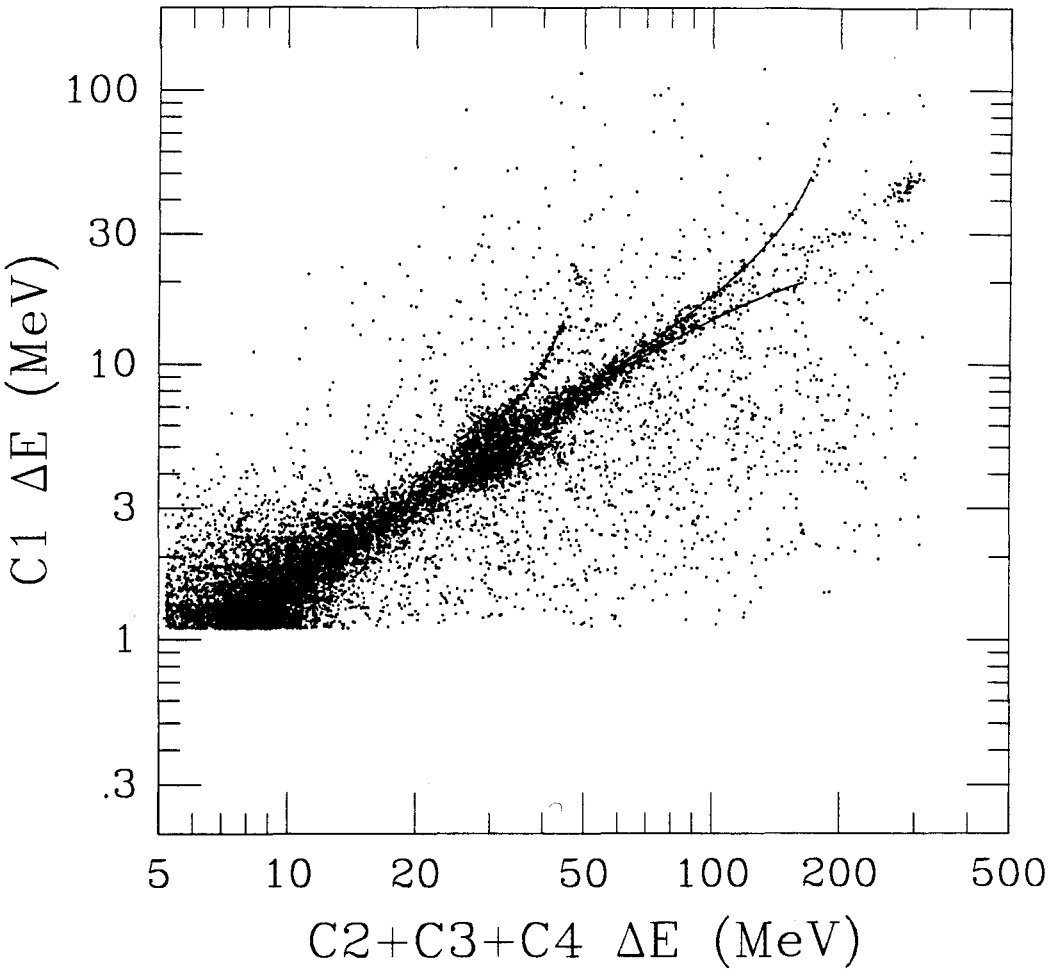

Figure 2.21, Figure 2.22, and Figure 2.23

Planar projections in ΔE_i space of the events in Figures 2.18, 2.19 and 2.20 separated into good events (top) and background (bottom).

Figure 2.21

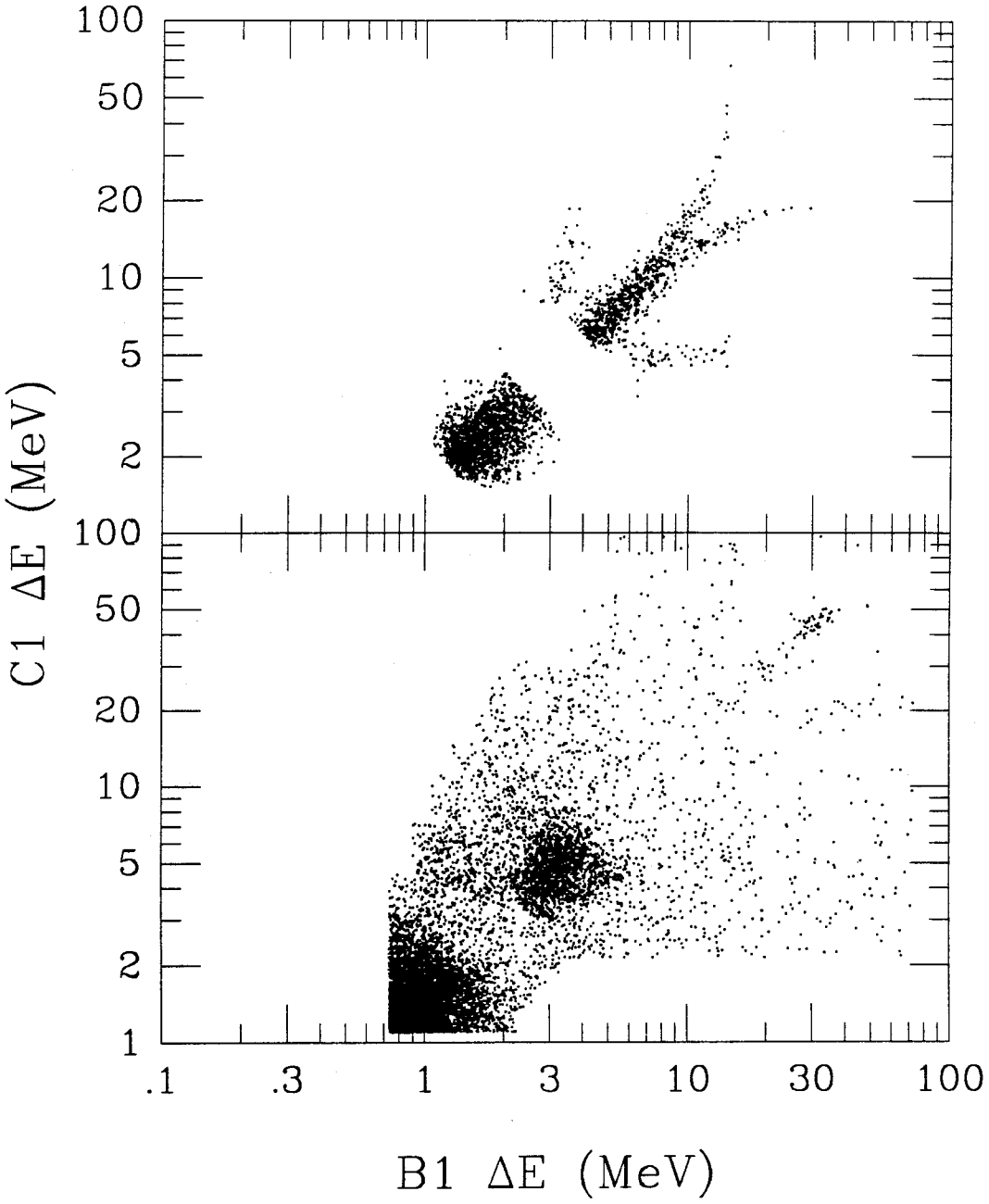

Figure 2.22

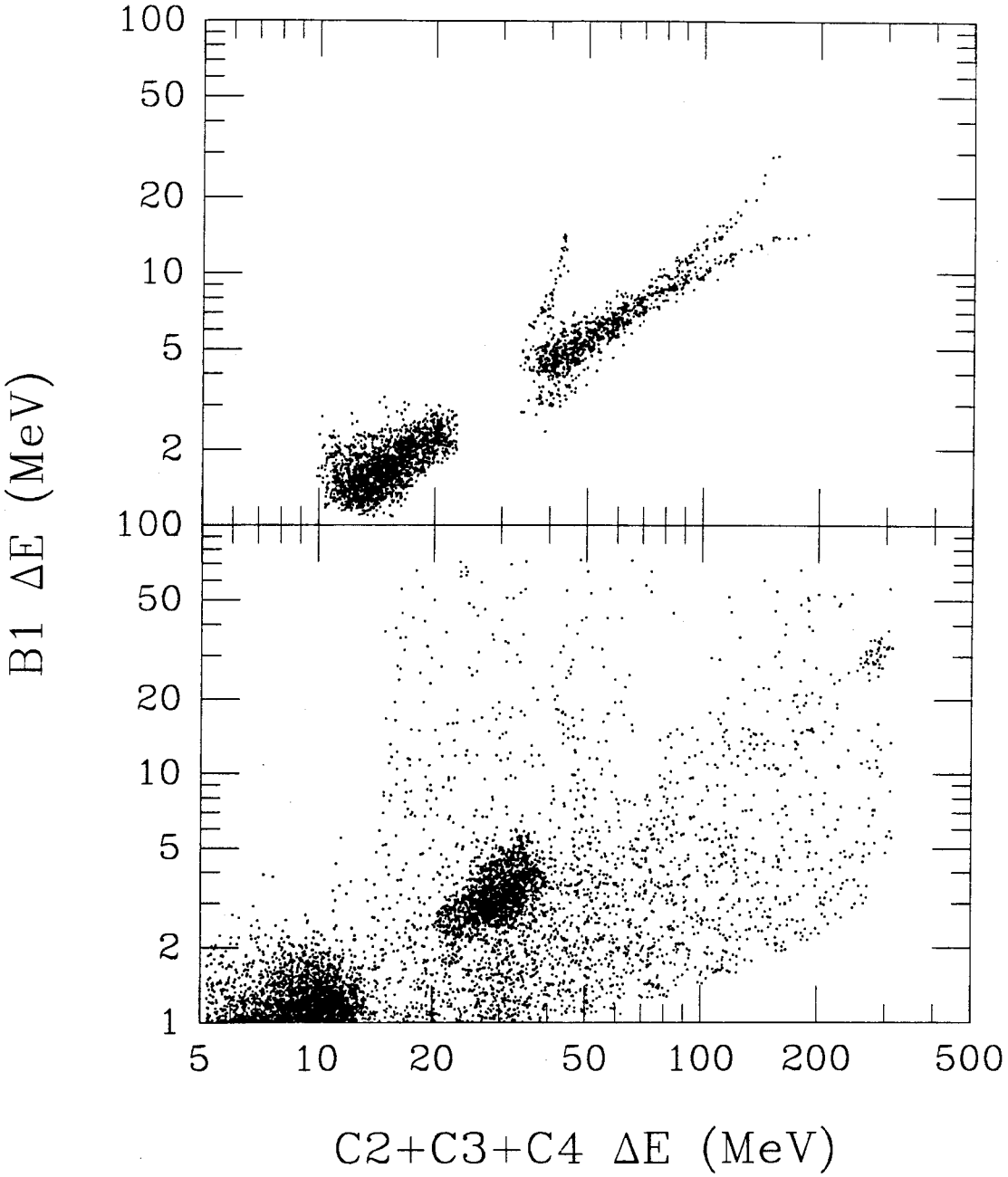
100
50
20
10
5
2
100
50
20
10
5
2
1
5
10
20
50
100
200
500
B1 ΔE (MeV)
C2+C3+C4 ΔE (MeV)

Figure 2.23

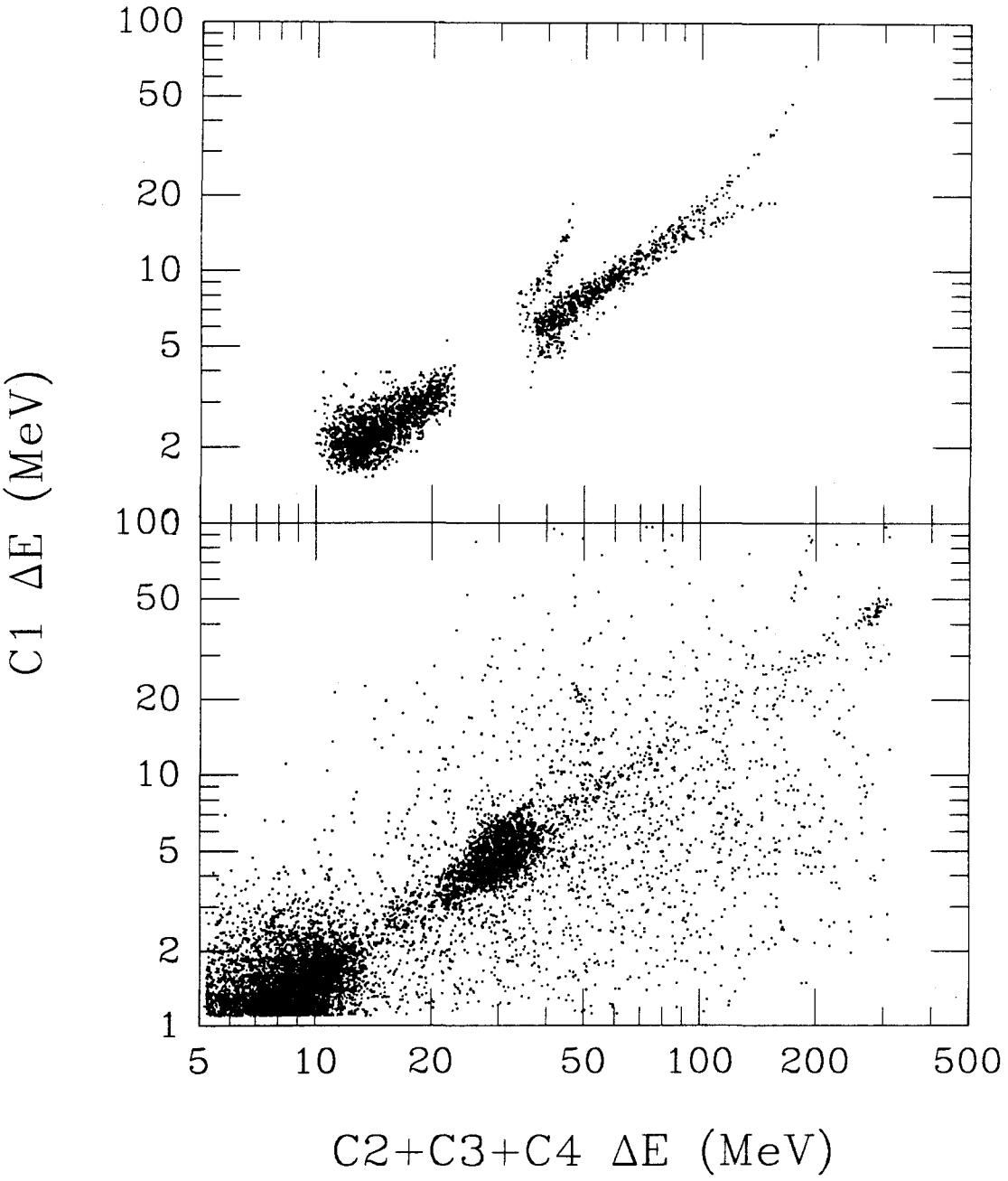
100
50
20
10
5
2
100
50
20
10
5
2
1
5
10
20
50
100
200
500
C1 ΔE (MeV)
C2+C3+C4 ΔE (MeV)

2.4.3.1. Secondaries

A problem appeared when the low energy (79 - 87 MeV) Penetrating hydrogen was analyzed. In the same energy region, the flux of particles coming from the A side of the telescope was 15% to 40% higher than the flux from the B side. The percentage difference decreased (although the absolute difference increased) as the integral fluxes increased (approaching solar minimum). This is apparently due to the trigger conditions used in the Penetrating mode. Each Penetrating event is required to trigger detectors C1, B1, and B2 (although B2 is not pulse-height analyzed). Particles coming from the B side of the telescope encounter only a small amount of mass, 50 μm equivalent silicon from an aluminized mylar window, in the short distance they travel before they hit detector B1.

Particles from the other direction encounter several times the mass (window, detector A1, and detector A2) before they hit detector C1, which is nearly 7 cm from the front of the detector on this side. Also in this extra 7 cm, the geometry of the B1 and C1 trigger encompasses a substantial amount of mass from the aluminum structure surrounding the telescope. Thus any particles that fragment above C1 and send only a proton into the stack will appear identical to a primary hydrogen. Also a primary proton of initially higher energy can enter the side of the telescope, lose energy in the aluminum structure, and register as a proton in this energy range.

This problem is small for the B side, and for the A-Stopping and B-Stopping events because the first detector in the trigger is close to the front of the telescope, and the pulse-height measurement in this first detector can be used to discriminate against this type of event. However, detector A1 could not be added into the trigger requirement for Penetrating particles because high energy protons deposit insufficient energy

in the thin A1 detector.

This does not seem to be a problem for helium events because the directional asymmetry for the lowest energy helium Penetrating events is less than 3% of the total flux. This is probably because the flux of primary cosmic rays heavier than helium is small compared to the helium flux and so relatively few secondary helium events are generated. Most of the secondary hydrogen, on the other hand, is probably generated by the primary helium flux, which is relatively large. The problem is avoided in the 79 MeV to 87 MeV energy bin for hydrogen by using only the value of flux entering from the B end of the telescope. All other energy bins for hydrogen and helium are the combined measurements from both directions.

Yet because the higher energy hydrogen fluxes must include particles from both the A and the B side, the question arises as to whether or not this population of events adds significant background to the high energy hydrogen fluxes. The directional asymmetry in the higher energy region cannot be directly measured; however, the contribution of the secondaries can be estimated by using the measured value of the secondary flux at 79 to 87 MeV from the difference of the two directions and an estimate of the spectral shape of these secondaries.

In order to obtain an estimate of the spectral shape of this population of secondaries, analysis was done on similar lower energy secondary events. As mentioned in §2.4.1, secondary events created in the first detector are visible in the scatter plot of the ΔE in the other two detectors for both stopping modes (Figures 2.12 and 2.17). For the A-Stopping direction, this population is not quite the same as that causing the excess in the Penetrating A-side flux because these events must trigger detectors A1 and A2. However, the higher energy penetrating events similar to these stopping events would be included in the excess penetrating flux, so one could reasonably expect similar

spectral shapes.

To determine the energy spectrum of A-Stopping secondaries, analysis was restricted to those events that were not accepted as good hydrogen by the three-dimensional analysis of §2.4.1, which are shown in the lower panel of Figure 2.11. Then cuts on the value of $\Delta E_{C1+C2+C3}$ were used to divide the events into regions for which the tracks were roughly linear, which corresponds to splitting the track into energy bins. Histograms along the direction perpendicular to the track in ΔE space were made for each of the energy bins. Figure 2.24 is the histogram of the region that corresponds to proton kinetic energies of 10 MeV to 14 MeV. The peaks of ^1H, ^2H, and ^3H are clearly visible although the deuterium and tritium are not in the same range of initial kinetic energies as the protons. The background was interpolated linearly between its values above and below the isotope peaks and subtracted to give the number of events in the peak, which was then used to calculate the flux. Figure 2.25 shows the derived energy spectra for the A-Stopping secondary proton events. Because the isotopes are mixed in the Penetrating mode, if the deuterium and tritium peak counts are included without any consideration as to their correct energy range, the secondary fluxes on Figure 2.25 would go up by $\sim$35% but the spectral shape would remain the same. Also on Figure 2.25 is the energy spectra for the B-Stopping secondary proton events obtained with a similar analysis.

The energy spectrum for A-Stopping is relatively flat at low energies, but steepens at the higher energies. It is approximately proportional to $E^{-0.8}$ between 25 MeV and 60 MeV. This is very similar to the $E^{-0.85}$ slope of the B-Stopping secondaries from 30 to 72 MeV, which indicates that the spectral shape may be the same. The flux of the B-Stopping secondaries is higher than the A-Stopping because the B-Stopping particles have had to pass through more than 11 times the mass. However, the fact that the

ratio of the fluxes is only ~5 instead of the expected 11 indicates that the A-Stopping secondaries include particles outside the nominal geometry factor for the trigger. These are probably particles that fragment in the side of the telescope, send a proton into the stack, and trigger A1 with another particle. Although this type of event also occurs in the B direction, the effect is relatively smaller.

In any case, taking an $E^{-0.8}$ spectrum for the secondaries and a flux level set by the difference of the two directions in the 79-87 MeV energy bin gives at maximum an 8% contribution for these particles in the 150-175 MeV energy bin during solar maximum, which decreases to ~3-4% at solar minimum. The absolute secondary flux increases with increasing galactic flux (decreasing modulation) but its relative contribution decreases, which is reasonable if the secondary flux is roughly proportional to the integral flux of higher energy particles.

Yet, using a spectral shape of $E^{-0.8}$ is likely to overestimate the contribution because the energy spectrum probably continues to steepen as energy increases. Therefore the analysis in this dissertation will use a correction that is proportional to E^{-1}, which will decrease the observed flux of protons above 150 MeV by less than 7%.

2.4.4. Problems with Method

Although this analysis works well as it stands now, there are still quite a few improvements that could be made. The penetrating analysis was done first and so lacks some of the refinements of the later work. Its selection cuts should be made diagonal in σ^2_E and $\sigma^2_{\Delta E}$ as in the A-Stopping and B-Stopping modes.

The analysis in all three modes still suffers from some common faults. The normalization of the variances is slightly different from mode to mode, and it is not exactly correct in any of them. They should be normalized by the width of their distribution,

Figure 2.24

Histogram of background events from Figure 2.11 (bottom) in a limited region of the track (6.86 (MeV) $<$ C1+C2+C3 Δ E $\leq$ 11.73 (MeV)), which corresponds to a proton initial kinetic energy of between 10 and 14 MeV. The x-axis is the direction perpendicular to the track (in arbitrary units). The dashed line shows the background, which was subtracted in order to get particle counts in the peaks.

Figure 2.24

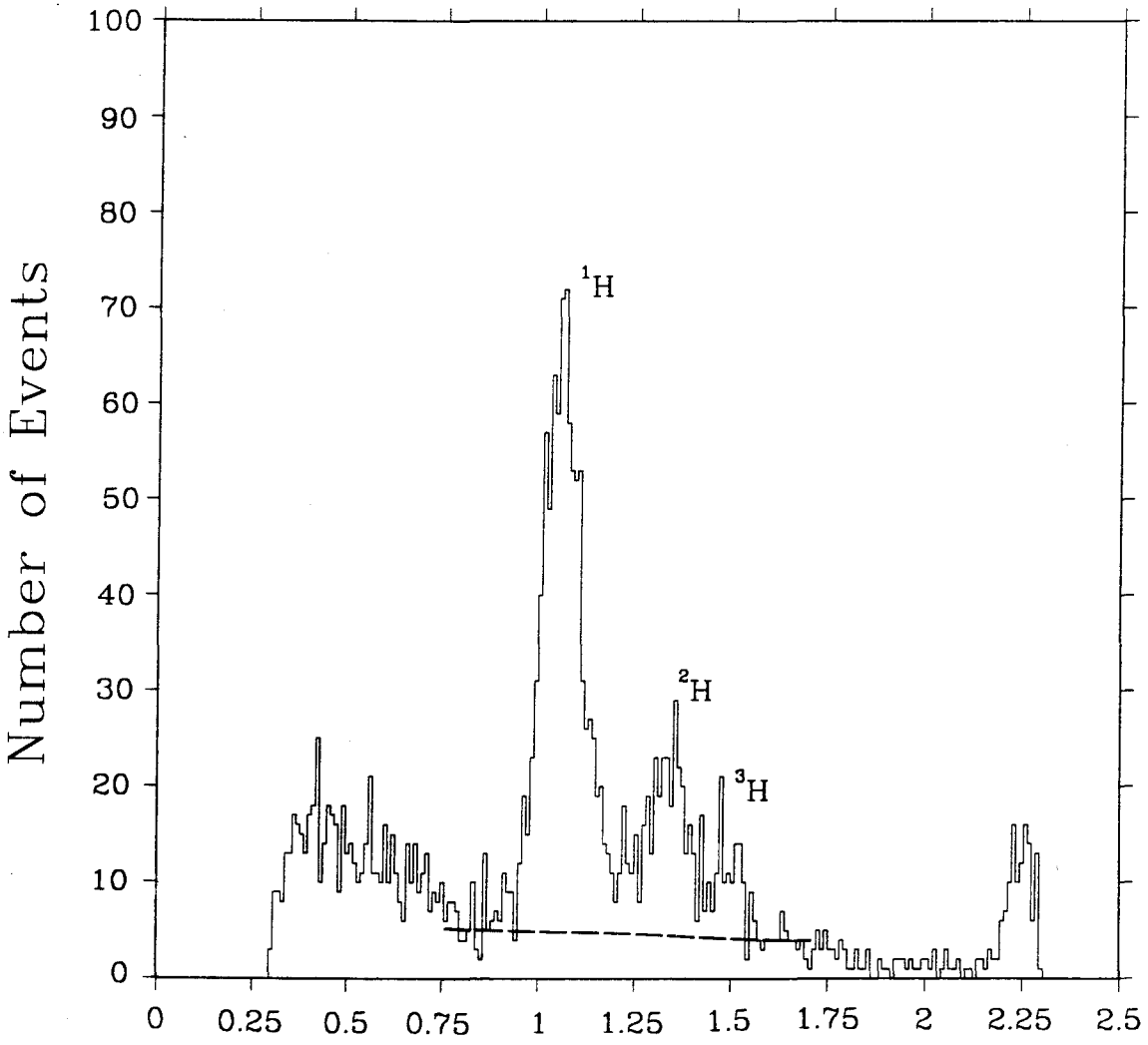
Number of Events
100
90
80
70
60
50
40
30
20
10
0
^{1}H
^{2}H
^{3}H
0
0.25
0.5
0.75
1
1.25
1.5
1.75
2
2.25
2.5
Direction Perpendicular to
Track (Arbitrary Units)

Figure 2.25

Derived energy spectra for A-Stopping and B-Stopping secondary proton events. The A-Stopping energy spectra have also been multiplied by 4.6 (open squares) to show the similarity in shape for the A-Stopping and B-Stopping energy spectra.

Figure 2.25

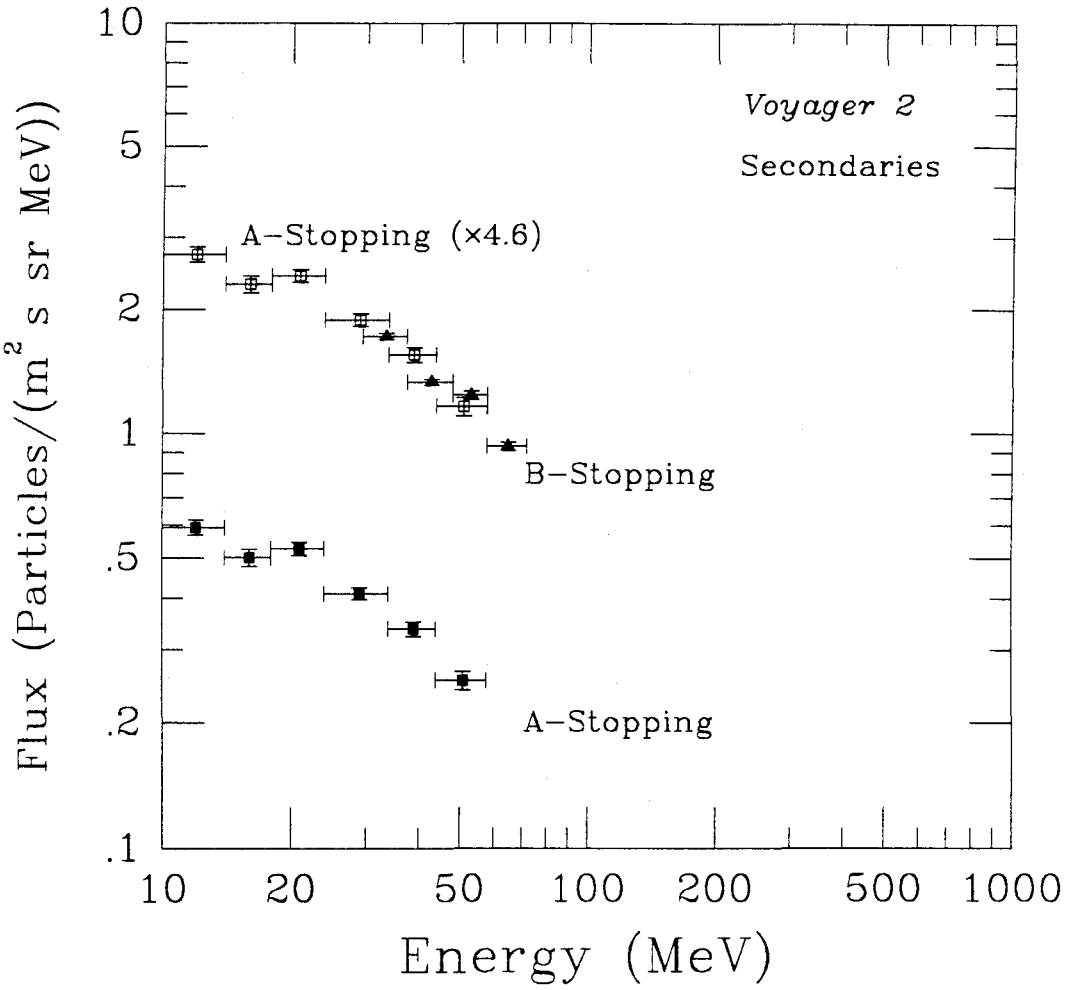
Voyager 2
Secondaries
A–Stopping (×4.6)
B–Stopping
A–Stopping
Flux (Particles/(m² s sr MeV))
Energy (MeV)
10
5
2
1
.5
.2
.1
10
20
50
100
200
500
1000

which is a function of energy. The normalization only approximates these widths. Also, the value, E_{avg} should be replaced by the analytically calculated closest point on the theoretical curve.

There is also some question about the detector thicknesses, because the thicknesses of the B and C detectors have been taken to be more than 10% larger than the nominal values in many cases. But then a multiplicative factor is necessary in order to fit the theoretical track to the center of the particle distribution. If the theoretical calculation is correct, then this may indicate that there may be uncertainties remaining in the assumed detector thicknesses used (Table 2.2). But as mentioned earlier, this only has second-order effects on the analysis.

However, all of these effects are at the few-percent level, and the analysis appears to work quite well, and so the solution of these problems has been left for future work.

2.5. Flux Calculations

The differential energy flux, $\frac{dJ}{dE}$, for particles of given Z and A is given by:

$$\frac{dJ(E)}{dE} = \frac{N}{dA \cdot d\Omega \cdot dt \cdot dE} \quad . \tag{2.9}$$

N is the number of particles that pass within a solid angle, $d\Omega$, hitting an area normal to the incoming direction, dA, within a time interval, dt, and with an energy in the range dE. In practice the flux must be calculated for finite times, energy ranges and a finite geometry factor ($A\Omega$). The geometry factor is the integral of $dA \cdot d\Omega$.

The *Voyager* telescopes, however, do not pulse-height analyze every event that successfully triggers a given mode, so the detector efficiency must also be factored in. The efficiency is directly calculated from *Voyager* rate data. Each trigger mode has a

dead-time-independent rate scalar (Rate) that counts all events that trigger, and a separate counter (PHA) to record the number of events that are successfully pulse-height analyzed. The formula for flux, dJ/dE, (in particles $m^{-2}\,s^{-1}\,sr^{-1}\,(MeV/nucleon)^{-1}$) is then given by:

$$\frac{dJ}{dE} = \frac{N \cdot Rate}{A\Omega \cdot \Delta E \cdot t \cdot PHA} \quad , \tag{2.10}$$

where N is the number of analyzed events in the energy bin. Statistical uncertainties in the flux are calculated from the number of particles in the bin, because the statistical uncertainties of Rate and PHA are much smaller.

The flux, dJ/dE, represents the differential flux at the median energy of the particles in the bin. This energy is close to the center point energy of the bin, but depends on the distribution, or spectral slope, of the particles for that energy bin. In the analysis, the spectral slope is approximated by the fluxes of the two adjacent energy bins taken at their midpoint. The median energy is then calculated from this slope.

The geometry factors are calculated for particles that stop in the center of the range of stopping locations for that energy bin. In calculating these geometry factors, the areas of the detectors have been multiplied by a factor, 0.94, to allow for the fact that 6% of the area of the detectors, at the edge, gives an incorrect value of of ΔE due to edge effects (Cook 1981). The *Voyager* HET geometry factors range from 7.8×10^{-5} m^2 sr to 1.66×10^{-4} m^2 sr, depending upon the range of the particle.

Because the ratios of *Voyager 1* and *Voyager 2* fluxes are very useful, the relative normalization of the fluxes of *Voyager 1* HET 2 and *Voyager 2* HET 1 was calculated. Shortly after launch in 1977 the two spacecraft were spatially close, and so should have registered the same flux. Four time periods were chosen in late 1977 and early 1978 when the solar activity was low and the electronics were stable. The calculated fluxes

were compared for wide energy bins in each of the three trigger modes. Both the A-Stopping and B-Stopping modes had the fluxes for hydrogen and helium agree to within 3%. This is less than other uncertainties and so the A-Stopping and B-Stopping flux calculation was not changed. For the Penetrating mode, the Helium fluxes for the two spacecraft were different by 7%, and the *Voyager 2* hydrogen flux was 20% higher than *Voyager 1*. For all the subsequent observations, the *Voyager 2* hydrogen Penetrating fluxes have been decreased by 20% and the *Voyager 2* helium Penetrating fluxes have been reduced by 7% so that the *Voyager 2* fluxes are normalized to those of *Voyager 1* (see Christian 1989).

Chapter 3

Observations

3.1. 1987 Solar Minimum

The effects of solar activity propagate out through the heliosphere with the solar wind at $\sim$400 - 600 km/s. The period of minimum solar activity for the recent solar cycle reached the two *Voyager* spacecraft in August 1987. Although *Voyager 1* is further from the sun ($\sim$32 AU in August 1987) than *Voyager 2* ($\sim$24 AU), solar minimum actually occurred at *Voyager 1* first because its position, $\sim 29^\circ$ above the ecliptic, puts it in a region of higher solar wind speed.

This is important to the topic of anomalous cosmic rays because solar minimum is the time of minimum solar modulation and therefore maximum cosmic ray fluxes. Both the galactic cosmic ray component and the anomalous cosmic rays reached their highest fluxes at the same time, but the changing modulation level had a much greater effect on the fluxes of the ACR than on the galactic cosmic rays (Mewaldt, Stone, and Vogt 1975; McDonald *et al.* 1981). Therefore the ratio of the anomalous cosmic rays to the GCR component was also at its maximum, making this the optimum time to study the difficult question of ACR hydrogen. However, the energy spectra of helium and other elements will be presented first to illustrate the spectral changes occurring during this time period and to facilitate the understanding of the hydrogen energy spectra.

3.1.1. Helium

Helium energy spectra for the two time periods 1985/261 - 365 and 1987/209 - 313 are shown for *Voyager 1* in Figure 3.1 and *Voyager 2* in Figure 3.2. The separate peaks of the ACR and GCR components are clearly visible, especially in the 1987 energy spectra. Helium is a very important part of this story because it is the only element other than hydrogen for which both the anomalous cosmic ray and galactic cosmic ray components have their spectral peak in the energy range analyzed by the *Voyager* CRS instruments. The solar energetic particle component is negligible for the energies plotted. Between these two time periods the anomalous cosmic ray peak has risen a factor of 5 in flux for *Voyager 1* and a factor of 10 for *Voyager 2*. The *Voyager 2* ACR helium flux is twice that of *Voyager 1* during this time despite the fact that *Voyager 1* is further from the sun and the radial gradient for cosmic rays is positive. This is again a consequence of *Voyager 1* being out of the ecliptic, because the anomalous cosmic ray components show a large negative latitudinal gradient during this time period (Cummings, Stone, and Webber 1987). The large increase in the anomalous cosmic ray component should be contrasted with the galactic cosmic ray component in which the fluxes have risen less than a factor of 2 between the 1985 and 1987 periods for both *Voyager 1* and *Voyager 2*.

Over the 1985 to 1987 interval, the energy of the peak fluxes of anomalous cosmic ray helium have shifted down in energy from $\sim$40 MeV/nucleon during 1985 to $\sim$22 MeV/nucleon during 1987. This is easily understandable in the framework of a simple, spherically symmetric (Fisk 1971) modulation theory that includes diffusion, convection, and adiabatic deceleration. Particles with higher rigidities (and thus higher energies) are not as heavily modulated as the lower rigidity particles and therefore are not as affected by the decrease in modulation.

This shifting of the peak energy also occurs for the galactic cosmic ray energy spectrum, although in Figures 3.1 and 3.2 it is not as noticeable because the effect is smaller. Careful examination of the effects of modulation on the ACR and GCR energy spectra requires that the two components be separated, as has been done in Figures 3.1 and 3.2. This can be easily achieved because the anomalous cosmic ray components of the elements for which the peak of the ACR energy spectrum can be observed (He, N, O, and Ne) have essentially the same shape (Cummings and Stone 1987). To separate the ACR and GCR energy spectra, first an estimate of the galactic energy spectrum is subtracted from the energy region ($\sim$7 - 74 MeV/nucleon) in which the anomalous flux dominates to obtain an estimated ACR energy spectrum. The galactic estimate used is a flux-proportional-to-energy (see §1.1.1) spectrum normalized to the total flux at $\sim$190 MeV/nucleon, which should be predominantly galactic. Then an ACR energy spectrum is obtained from a least-squares fit between a generic anomalous energy spectrum and the estimated ACR energy spectrum allowing the generic ACR energy spectrum to shift in both energy and flux. This ACR energy spectrum is subtracted from the total energy spectrum to obtain the galactic component.

The generic anomalous energy spectrum is illustrated in Figure 3.3 (from Cummings and Stone 1987), which shows *Voyager 2* ACR energy spectra of He, N, O, and Ne for the time period 1985/274 - 1986/254. The energy and flux scales of the He, N, and Ne energy spectra have been shifted to normalize them to the ACR O energy spectrum.

Figure 3.1

Voyager 1 helium energy spectra from the time periods 1985/261 - 365 (solid squares) and 1987/209 - 313 (open squares). The dashed curves show the shape of the anomalous cosmic ray energy spectra, and the dotted curves represent the galactic cosmic ray energy spectra.

Figure 3.1

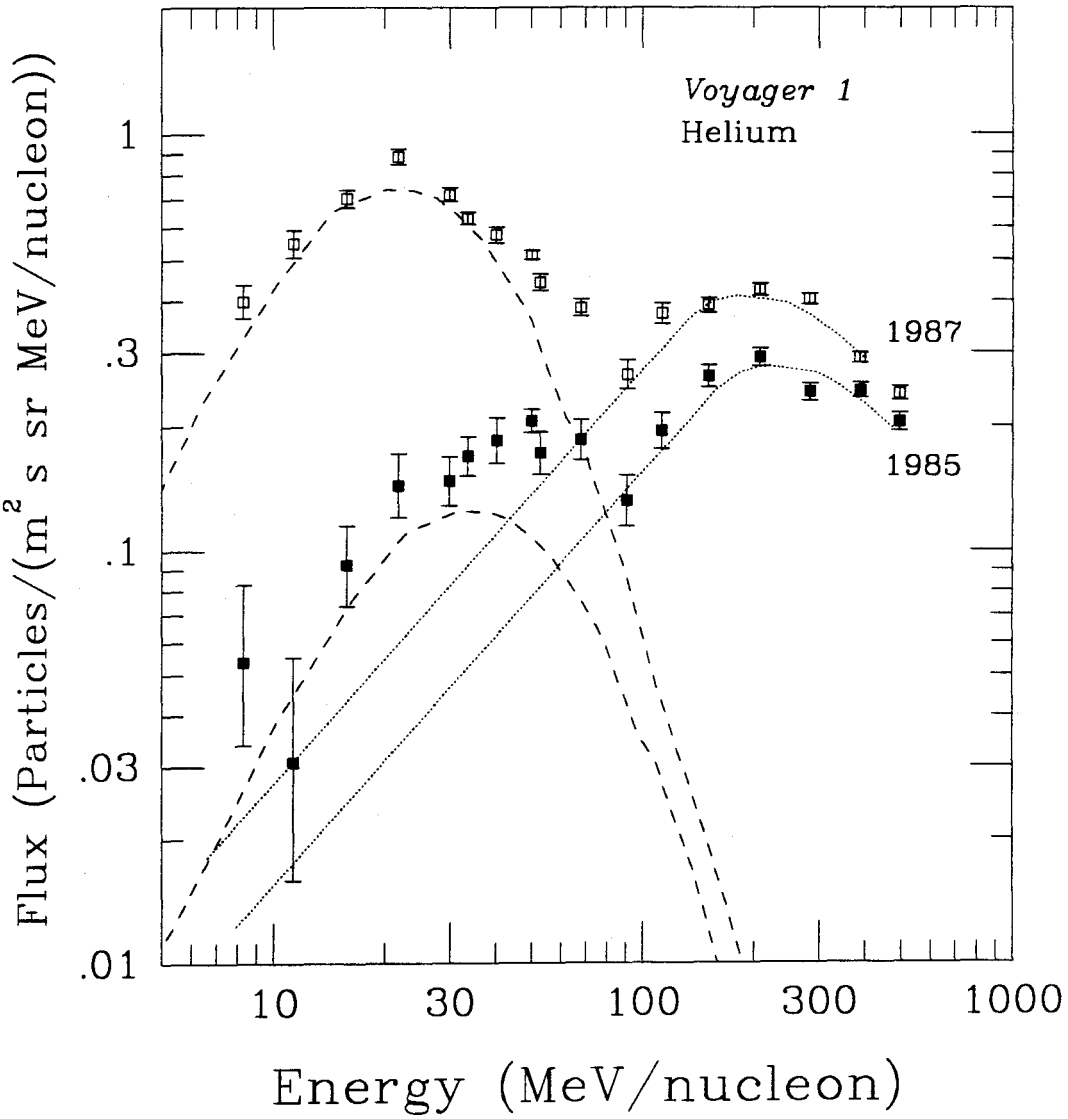
Voyager 1
Helium
1987
1985
Flux (Particles/(m² s sr MeV/nucleon))
1
.3
.1
.03
.01
10
30
100
300
1000
Energy (MeV/nucleon)

Figure 3.2

Voyager 2 helium energy spectra from the time periods 1985/261 - 365 (solid squares) and 1987/209 - 313 (open squares). The dashed curves show the shape of the anomalous cosmic ray energy spectra, and the dotted curves represent the galactic cosmic ray energy spectra.

Figure 3.2

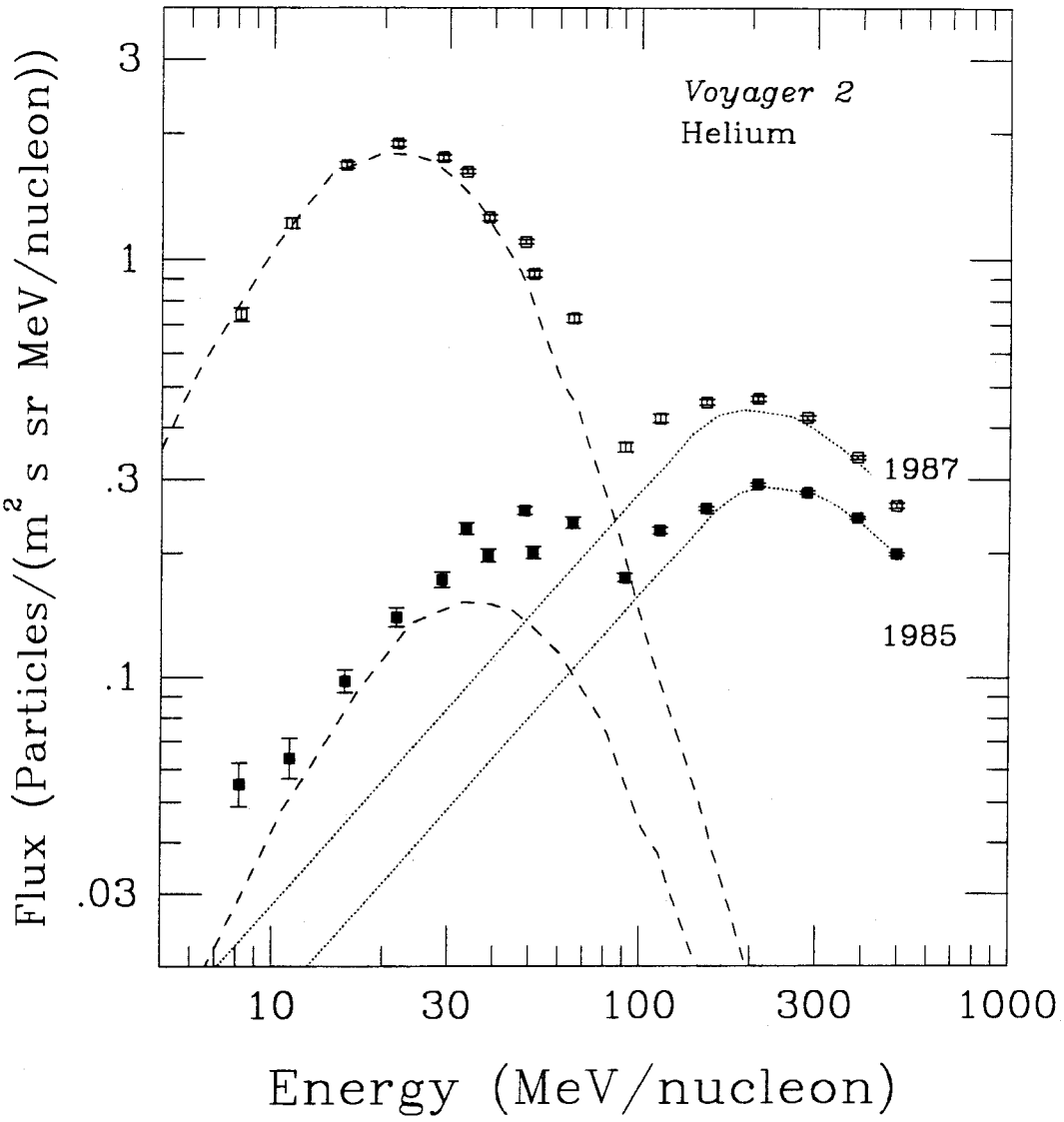
Voyager 2
Helium
1987
1985
3
1
.3
.1
.03
10
30
100
300
1000
Flux (Particles/(m² s sr MeV/nucleon))
Energy (MeV/nucleon)

Figure 3.3

ACR energy spectra of helium, nitrogen, oxygen, and neon from *Voyager 1* and *Voyager 2* combined. The helium, nitrogen, and neon energy spectra have been shifted in flux and energy to match the oxygen energy spectrum and demonstrate the common ACR spectral shape. (From Cummings and Stone (1987).)

Figure 3.3

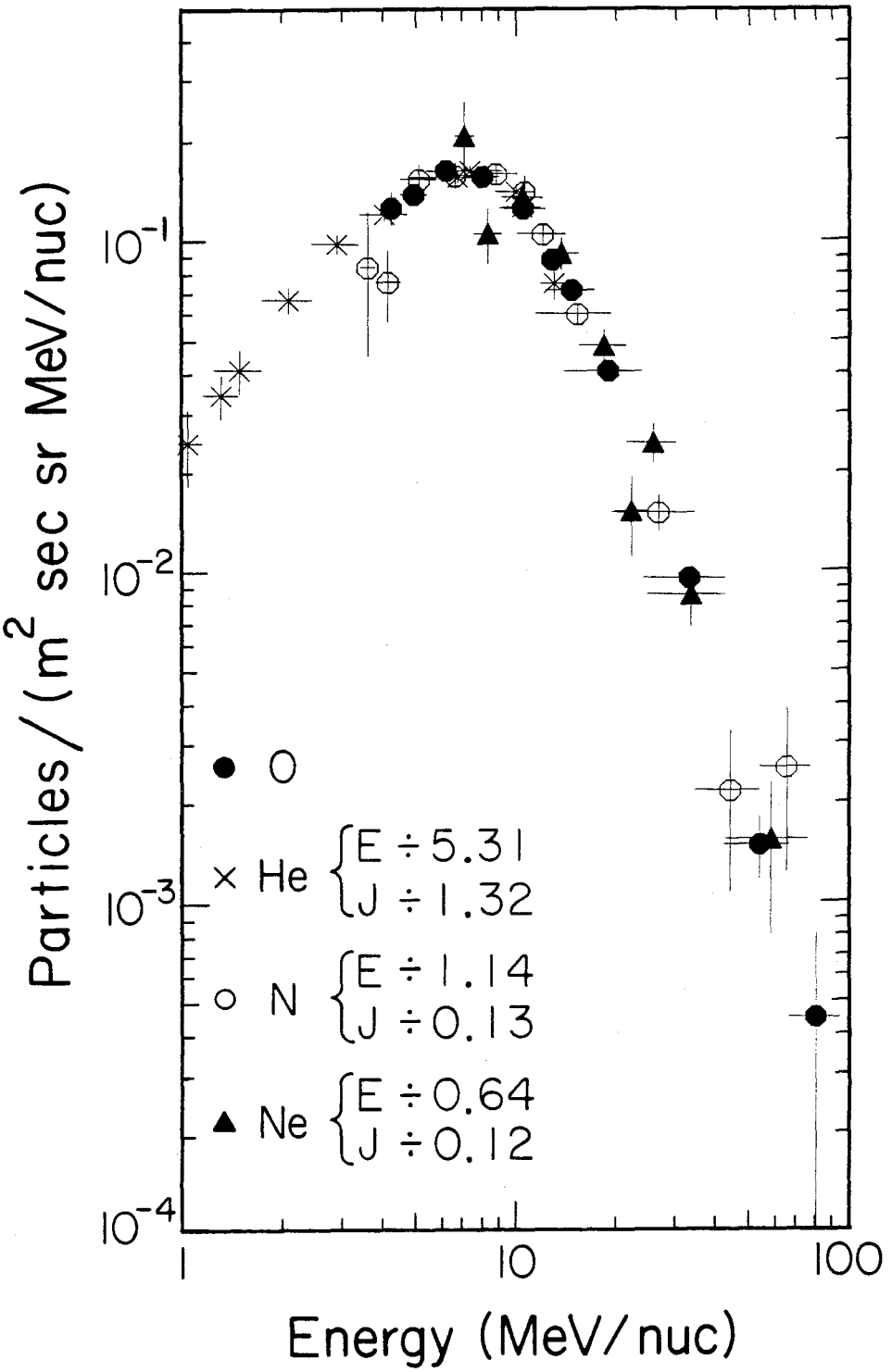
Particles/(m² sec sr MeV/nuc)
10⁻¹
10⁻²
10⁻³
10⁻⁴
1
10
100
Energy (MeV/nuc)
● O
× He {E ÷ 5.31 J ÷ 1.32
○ N {E ÷ 1.14 J ÷ 0.13
▲ Ne {E ÷ 0.64 J ÷ 0.12

3.1.2. Other Elements

Voyager 1 and *Voyager 2* also show large increases of the anomalous cosmic ray fluxes relative to the GCR fluxes for elements other than helium. This has allowed the recent detection of ACR components of carbon and argon (Cummings and Stone 1987). The fact that all of these ACR components have similar spectral shapes at different energies is very important to the subsequent discussion of anomalous cosmic ray hydrogen.

If the input energy spectra at the modulation boundary are similar power laws for the different elements, then simple modulation theory would predict that characteristic spectral features, such as spectral peaks, should occur at an energy for each species for which the particles have the same diffusion coefficient, κ (see Cummings, Stone, and Webber 1984). As shown in Cummings, Stone, and Webber (1984), this implies the location of the peaks of the energy spectra scale as

$$f_E \propto \left(\frac{A}{Z} \right)^{-2\gamma/(\gamma+1)} , \qquad (3.1)$$

where A is the particle's mass, Z is the charge state, and γ comes from the conventional assumption that $\kappa \propto \beta R^{\gamma}$ with β the particle velocity and R the rigidity. For a singly-ionized anomalous cosmic ray component the energy of the spectral peaks should scale as a power of the mass.

At *Voyager 2* in the middle of 1987, nitrogen, oxygen, and neon have clearly distinguishable ACR spectral peaks (Figure 3.4), as well as helium (Figure 3.2). The energy spectra in Figure 3.4 are dominated by anomalous cosmic rays with the galactic components visible as increases in flux above $\sim$60 MeV/nucleon. The position (in MeV/nucleon) of these peaks, as determined by a least-squares fit to the common

spectral shape, is plotted versus particle mass in Figure 3.5 along with the least-squares fit power law through the four points. This is very useful for the analysis of anomalous cosmic ray hydrogen because, by extrapolating the scaling of Figure 3.5 to hydrogen, we would predict that, if there were an observable ACR hydrogen component in the middle of 1987, the peak of its energy spectra would be at $\sim 124 \pm 2$ MeV.

3.2. Hydrogen

Proton energy spectra for *Voyager 1* (Figure 3.6) and *Voyager 2* (Figure 3.7) are shown for the 1985/261 - 365 and 1987/209 - 313 time periods. It is clear that there are not two distinct peaks for the anomalous and galactic proton components. The single peak has long been thought to be galactic cosmic rays. The question then becomes whether there are any changes in the predominantly galactic energy spectrum that might be attributed to an increase of an anomalous cosmic ray hydrogen component relative to the galactic component during solar minimum.

The hydrogen energy spectra in Figures 3.8 and 3.9 are the same as those in Figures 3.6 and 3.7, but with the fluxes divided by energy to flatten the energy spectra and accentuate the differences in shape. The curves, which have been drawn through the two 1985 energy spectra, are also scaled up in flux to match the 1987 energy spectra at the highest energy and illustrate the change in spectral slope that has occurred between the two time periods. These spectra differ from our previously published spectra (Christian *et al.* 1988) primarily due to improved normalization between the two spacecraft (see §2.5). These changes are as large as $\sim$13% for Voyager 2 Penetrating (high energy) fluxes, but in most cases are only a few percent. The secondary subtraction has also been improved (see § 2.4.3.1), and the new energy bins have slightly different limits. These changes have not made any qualitative difference to the subsequent analysis.

Figure 3.4

Oxygen, nitrogen, and neon energy spectra at *Voyager 2* during the time period 1987/105 - 313. The energy spectra are dominated by anomalous cosmic rays at the low energies. Galactic cosmic rays are responsible for the increase in flux above ~60 MeV/nucleon.

Figure 3.4

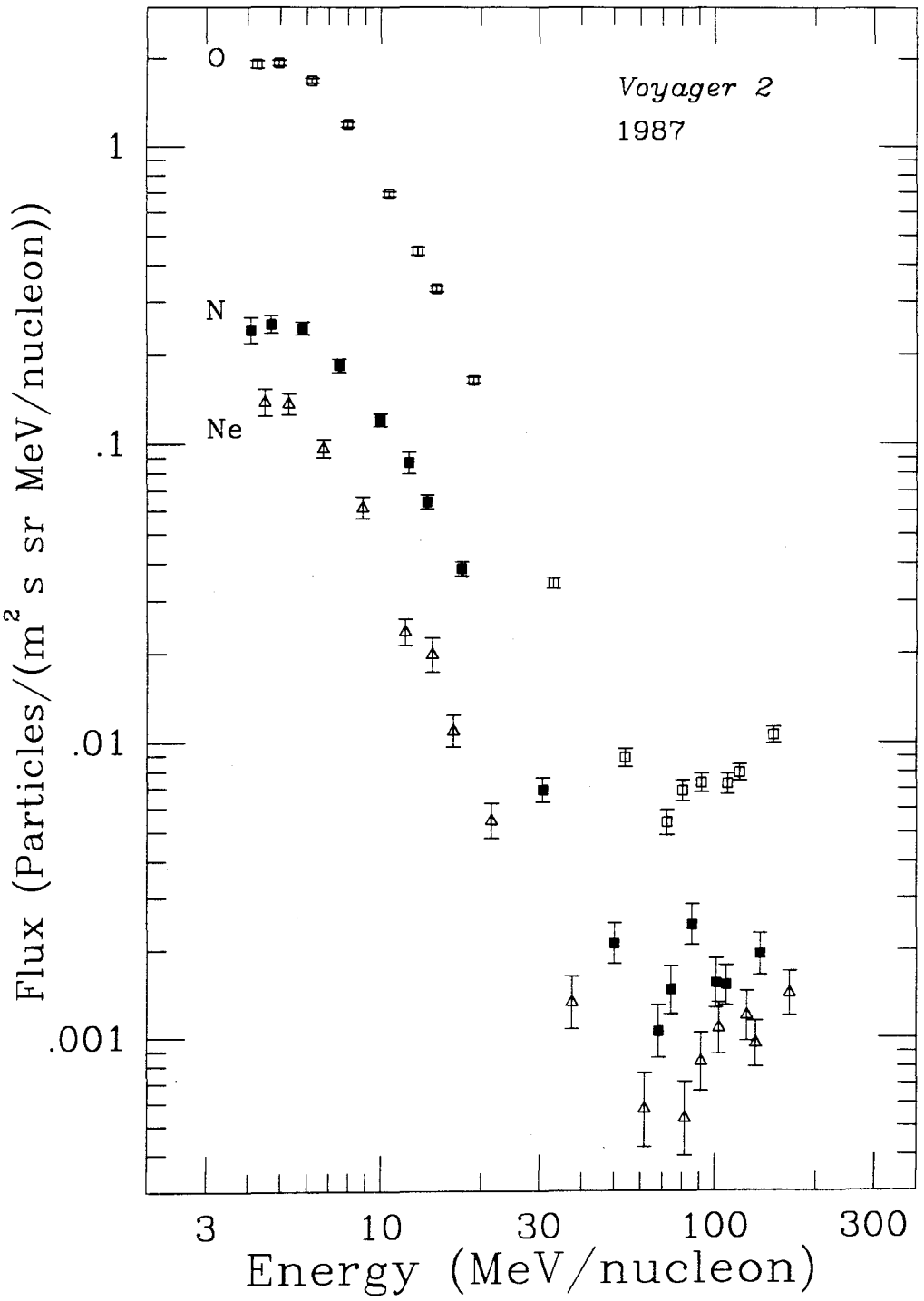
O
N
Ne
Voyager 2
1987
1
.1
.01
.001
Flux (Particles/(m² s sr MeV/nucleon))
3
10
30
100
300
Energy (MeV/nucleon)

Figure 3.5

Energy of peak anomalous cosmic ray flux vs. mass, A. The dashed line is the least-squares fit to the four data points. The expected energy of the hydrogen (A = 1) ACR peak is 124±2.

Figure 3.5

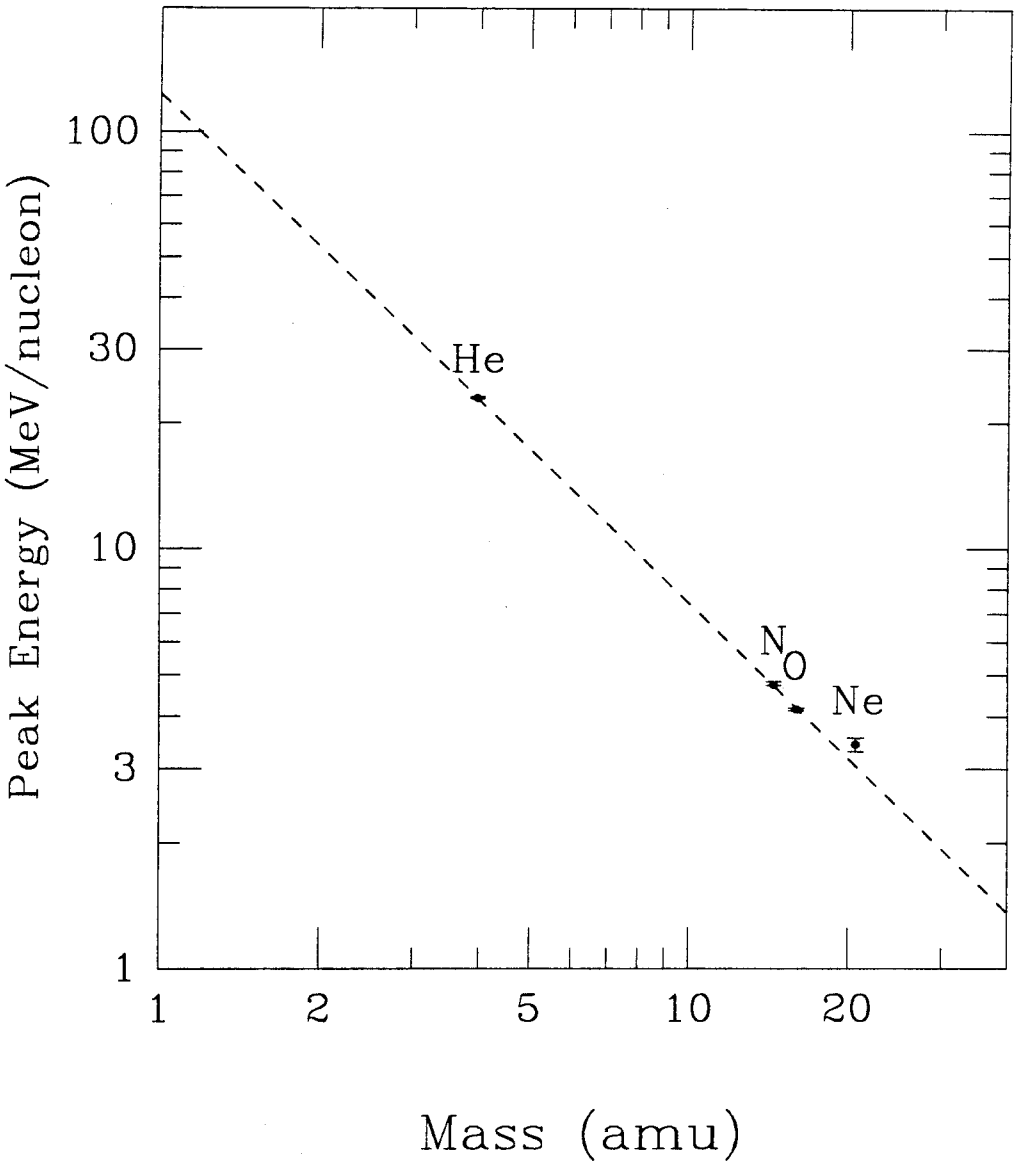

Figure 3.6

Voyager 1 hydrogen energy spectra for the time periods 1985/261 - 365 (solid squares) and 1987/209 - 313 (open squares).

Figure 3.6

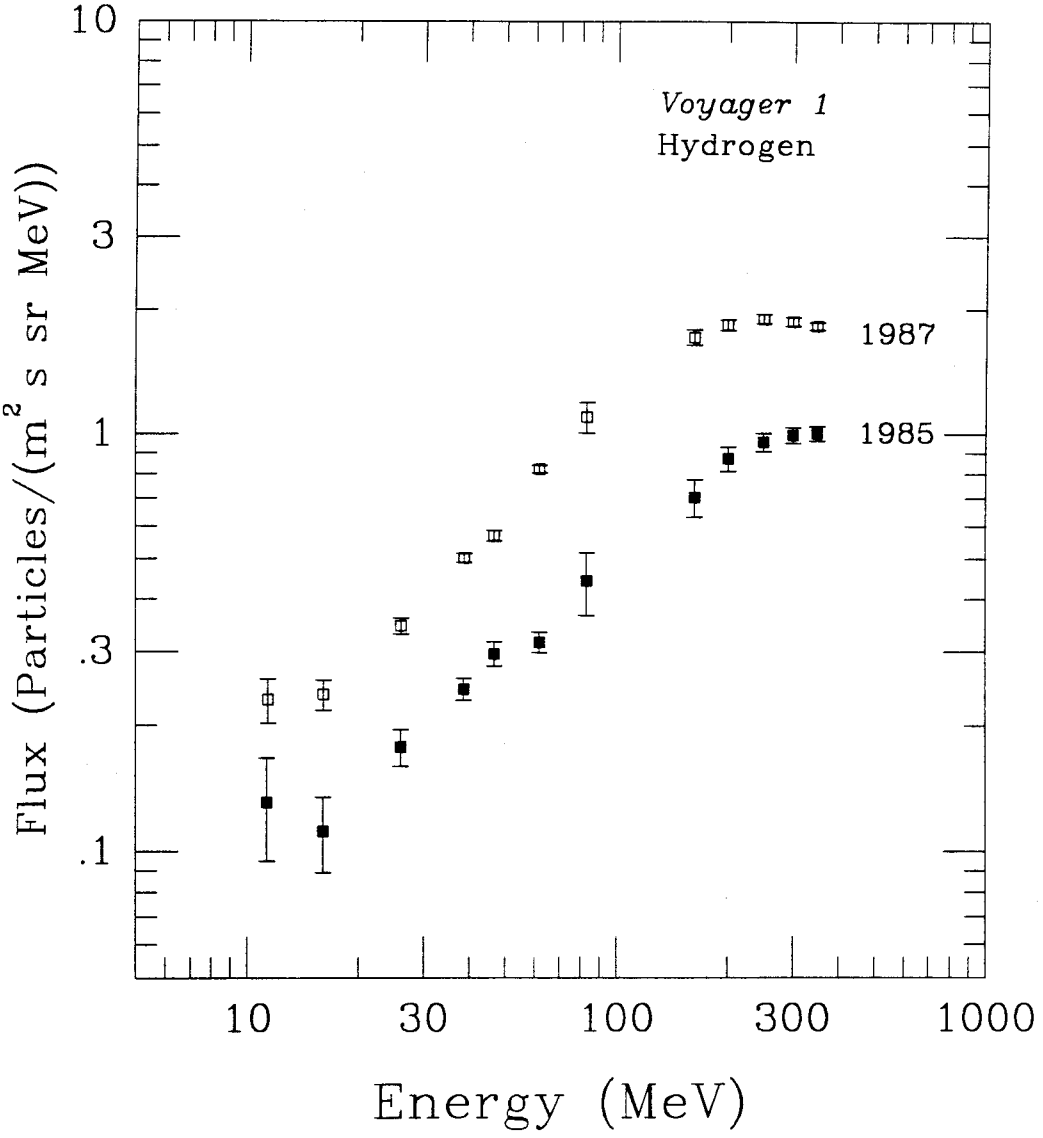
Voyager 1
Hydrogen
1987
1985
Flux (Particles/(m² s sr MeV))
10
3
1
.3
.1
10
30
100
300
1000
Energy (MeV)

Figure 3.7

Voyager 2 hydrogen energy spectra for the time periods 1985/261 - 365 (solid squares) and 1987/209 - 313 (open squares).

Figure 3.7

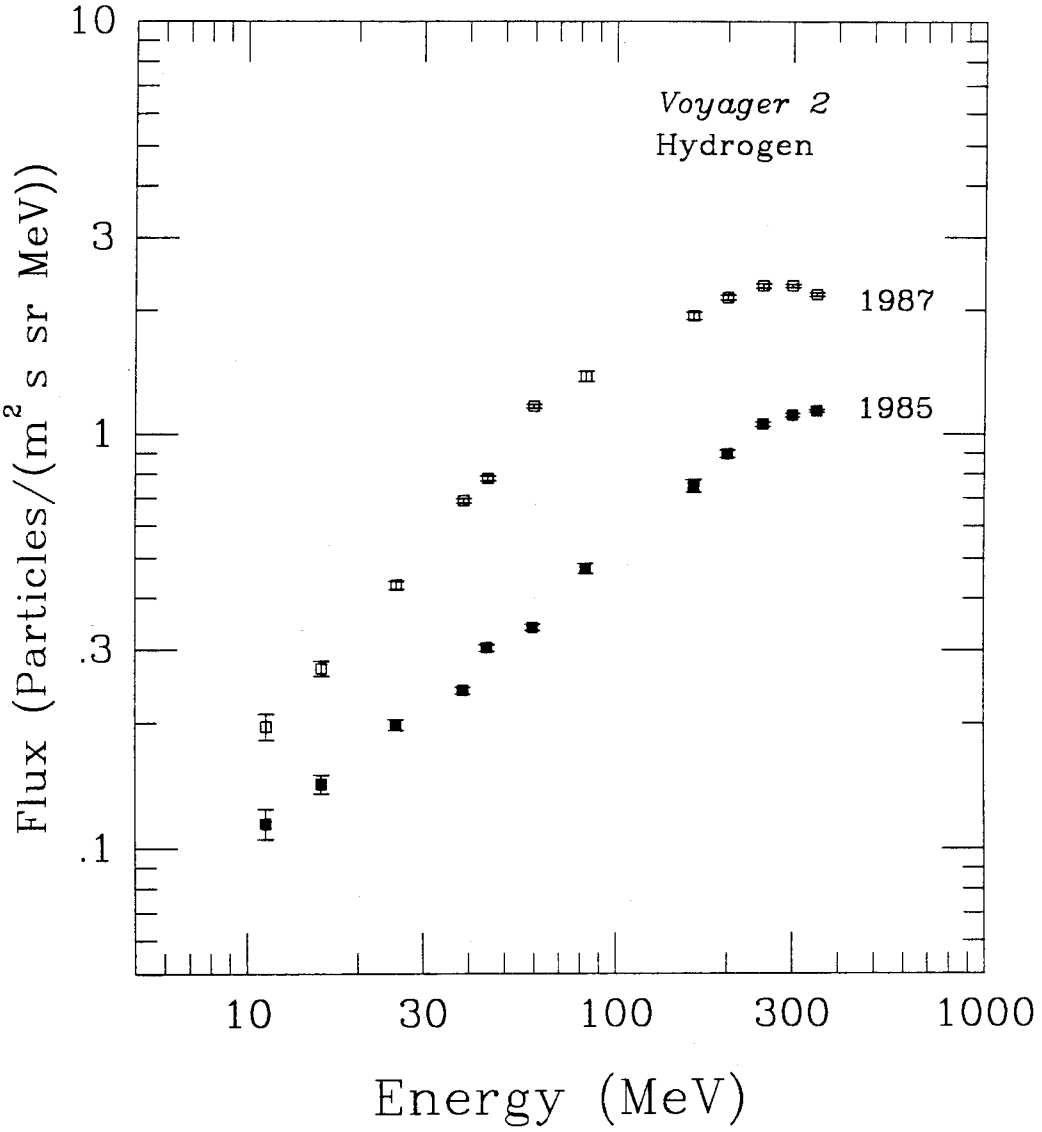
Voyager 2
Hydrogen
1987
1985
Flux (Particles/(m² s sr MeV))
10
3
1
.3
.1
10
30
100
300
1000
Energy (MeV)

Figure 3.8

The *Voyager 1* energy spectra of Figure 3.6 with the fluxes divided by energy to flatten the energy spectra. The dashed curve is the shape of the 1985 energy spectrum (solid curve) scaled up to match the 1987 energy spectrum and illustrates the change in spectral shape that has occurred.

Figure 3.8

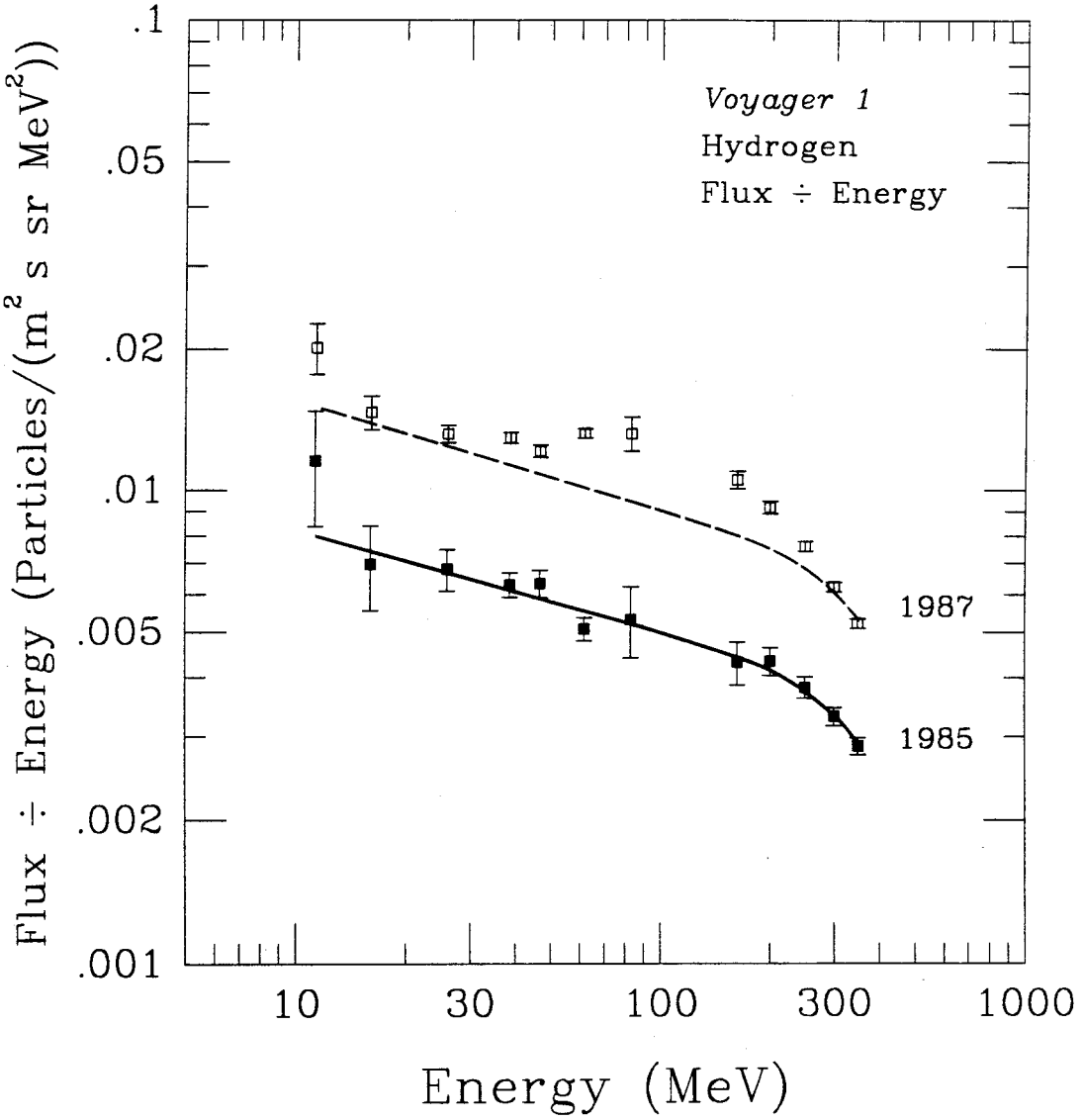
Voyager 1
Hydrogen
Flux ÷ Energy
1987
1985
.1
.05
.02
.01
.005
.002
.001
10
30
100
300
1000
Flux ÷ Energy (Particles/(m² s sr MeV²))
Energy (MeV)

Figure 3.9

The *Voyager 2* energy spectra of Figure 3.7 with the fluxes divided by energy to flatten the energy spectra. The dashed curve is the shape of the 1985 energy spectrum (solid curve) scaled up to match the 1987 energy spectrum and illustrates the change in spectral shape that has occurred.

Figure 3.9

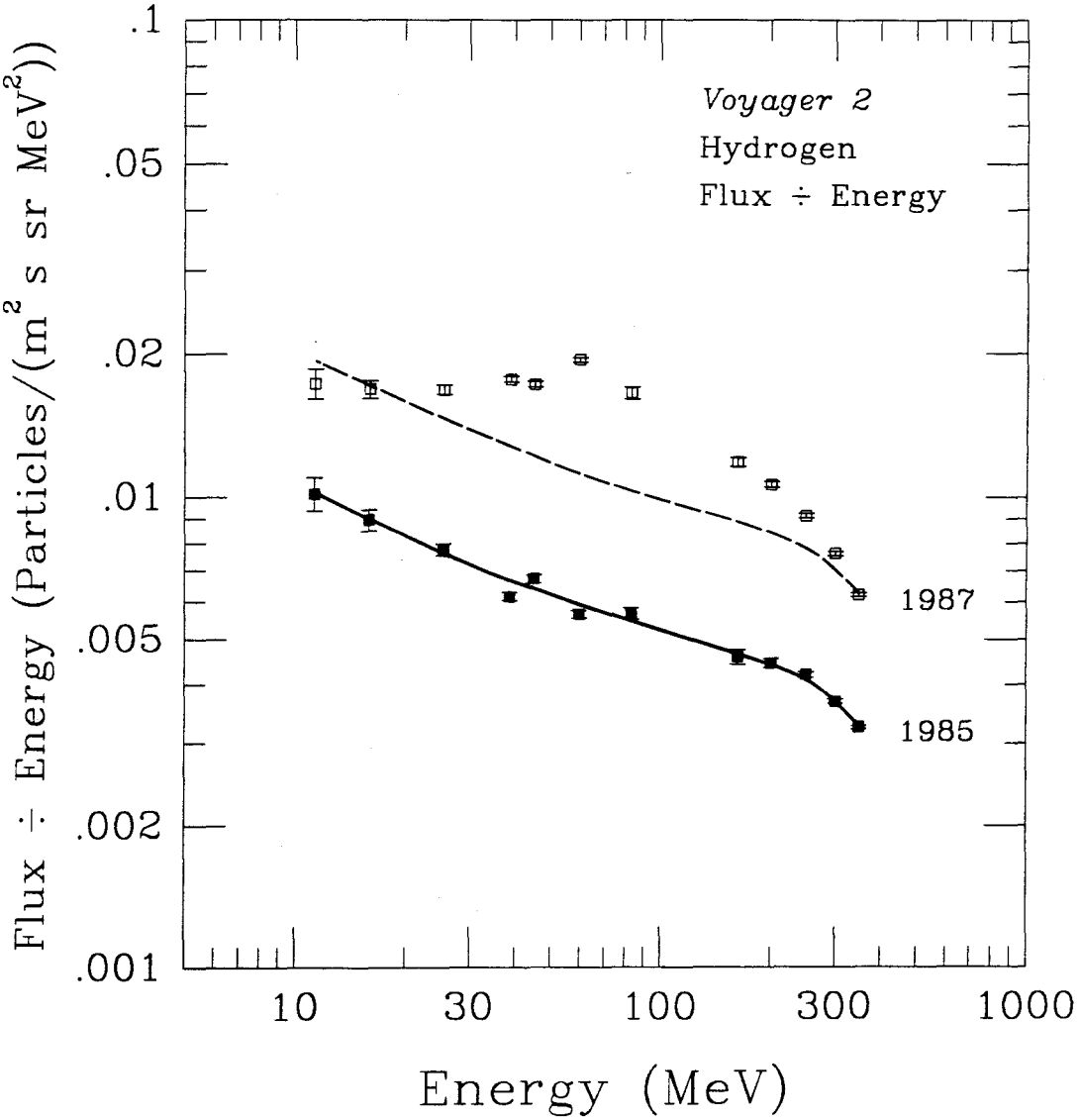
Voyager 2
Hydrogen
Flux ÷ Energy
1987
1985
.1
.05
.02
.01
.005
.002
.001
10
30
100
300
1000
Flux ÷ Energy (Particles/(m² s sr MeV²))
Energy (MeV)

The major difference between the two time periods in the energy spectra of Figures 3.8 and 3.9 is an increase in flux resulting from a decrease in the solar modulation level between 1985 and 1987. Both *Voyager 1* and *Voyager 2* energy spectra show a change in shape, which is more pronounced in *Voyager 2*. There are two different processes that might contribute to the spectral change.

As stated earlier (§3.1.1), a decrease in modulation also causes a shift in the energy of the peak. Simple modulation theory would predict that the overall shape of the energy spectrum should remain the same although shifted in energy. Thus, the downward shift of the peak might be due to modulation effects, but *Voyager 2* shows changes that are inconsistent with the possibility that the 1985 and 1987 energy spectra are the same shape. Even so, it will be important to explore any contributions of more complex modulation effects to the spectral shape changes.

Because the spectral change can be characterized as an excess of flux in the region around $\sim$100 MeV, the other possibility is that some of this excess is the result of an increase in the contribution of anomalous cosmic ray hydrogen in this energy region. Several different methods of estimating the amount of ACR hydrogen in these energy spectra were used.

3.2.1. First Estimate of ACR Hydrogen

The first and simplest approximation is to assume that all of the shape change seen in Figures 3.8 and 3.9 is due to an increase in an anomalous hydrogen component. During the 1985 time period the anomalous component should be a factor of 5 to 10 smaller than during 1987. Assuming this ACR contribution is small in the 1985 *Voyager 1* and *Voyager 2* energy spectra, these 1985 energy spectra can be used as an

estimate of the pure galactic spectral shape at the two spacecraft in 1987 as well as in 1985.

Assuming that the galactic energy spectrum has increased in flux between 1985 and 1987, but has not had the spectral peak shift down in energy (as it should), then the dashed curves in Figures 3.8 and 3.9 are estimates of the galactic flux in 1987. Then subtracting this estimate of the GCR flux from the observed 1987 flux gives a measure of the excess flux. Notice that, although the dashed curves in Figures 3.8 and 3.9 are normalized to the 1987 energy spectra at the highest energy (350 MeV), they also pass through the observed energy spectra at the lower energies ($\sim$20 MeV). This indicates that the excess can be characterized by a peak in the intermediate energies. Figure 3.10 shows this estimate of the ACR energy spectrum in *Voyager 1*, as well as the observed 1987 hydrogen energy spectrum and the assumed galactic energy spectrum (dotted line) as derived from the *Voyager 1* 1985 energy spectrum. The dashed line is the least-squares fit of the anomalous spectral shape to the excess. Figure 3.11 shows the same for *Voyager 2*. The peak ACR hydrogen fluxes (as given by the fit to the ACR shape) are 0.241$\pm$0.029 particles/m^2 s sr MeV at $\sim$158 MeV for *Voyager 1* and 0.505$\pm$0.010 particles/m^2 s sr MeV at $\sim$117 MeV for *Voyager 2*.

In our published paper on the evidence for anomalous cosmic ray hydrogen (Christian, Cummings, and Stone 1988), we referred to this estimate as an upper estimate because it underestimates the modulation induced effects in the spectral shape change. However, as stated in Christian, Cummings, and Stone (1988), this approach might be expected to underestimate the anomalous cosmic ray hydrogen flux by 10% to 20%, because the 1985 energy spectra should include an anomalous component, which is $\sim$20% of the flux in 1987 for *Voyager 1* and $\sim$10% for *Voyager 2*, as is the case for the anomalous cosmic ray helium shown in Figures 3.1 and 3.2. A further underestimate

Figure 3.10

First estimate of ACR hydrogen (solid squares) in *Voyager 1* for the time period 1987/209 - 313. The open squares show the observed hydrogen energy spectrum for this time period. The dotted curve shows the estimated galactic energy spectrum obtained by shifting the observed *Voyager 1* 1985/261 - 365 up in flux to match the 1987 energy spectrum at the highest energy (350 MeV). The dashed curve is the least-squares fit of the anomalous cosmic ray spectral shape to the first estimate points.

Figure 3.10

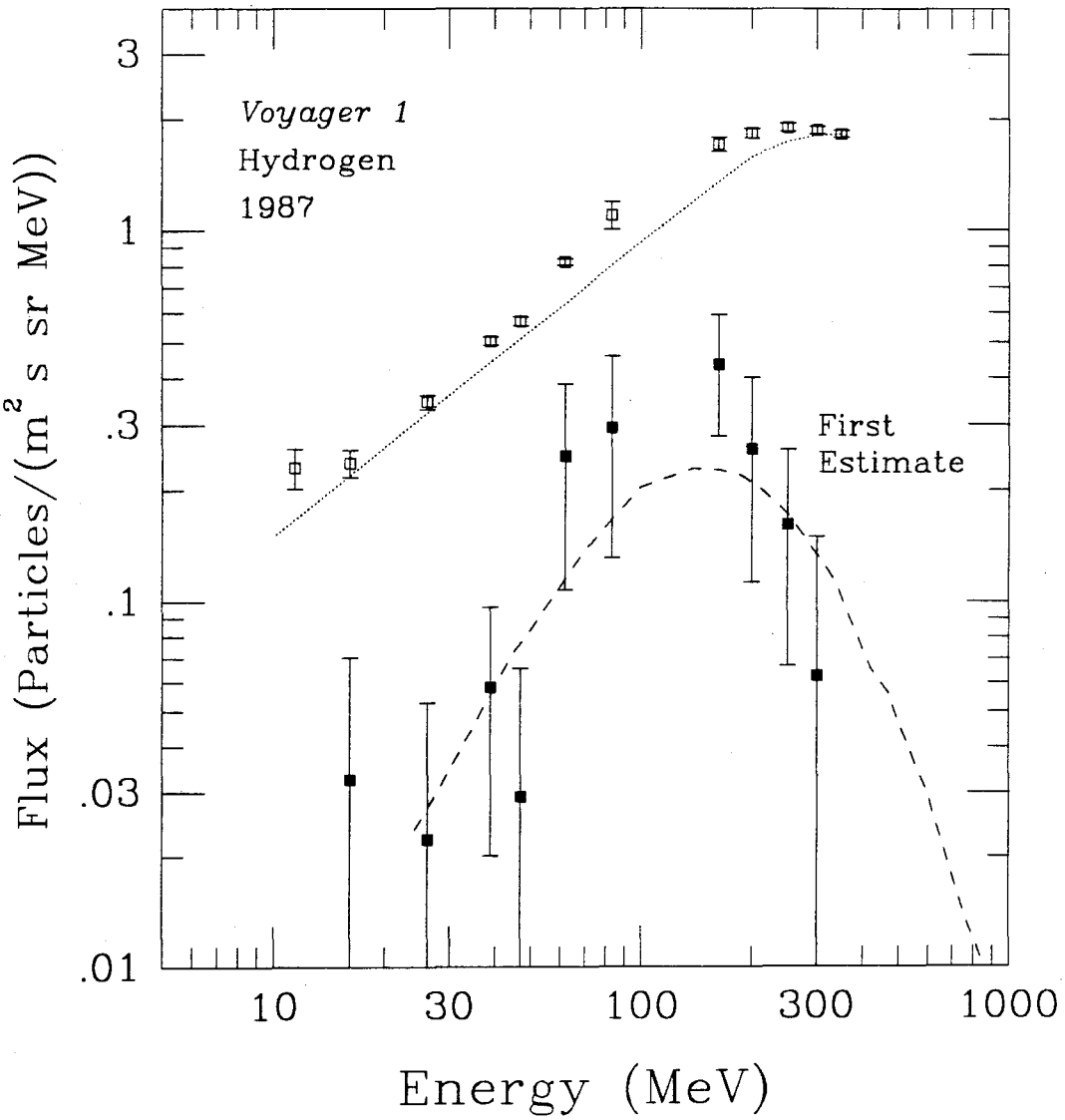
Voyager 1
Hydrogen
1987
First
Estimate
Flux (Particles/(m² s sr MeV))
3
1
.3
.1
.03
.01
10
30
100
300
1000
Energy (MeV)

Figure 3.11

First estimate of ACR hydrogen (solid squares) in *Voyager 2* for the time period 1987/209 - 313. The open squares show the observed hydrogen energy spectrum for this time period. The dotted curve shows the estimated galactic energy spectrum obtained by shifting the observed *Voyager 2* 1985/261 - 365 up in flux to match the 1987 energy spectrum at the highest energy (350 MeV). The dashed curve is the least-squares fit of the anomalous cosmic ray spectral shape to the first estimate points.

Figure 3.11

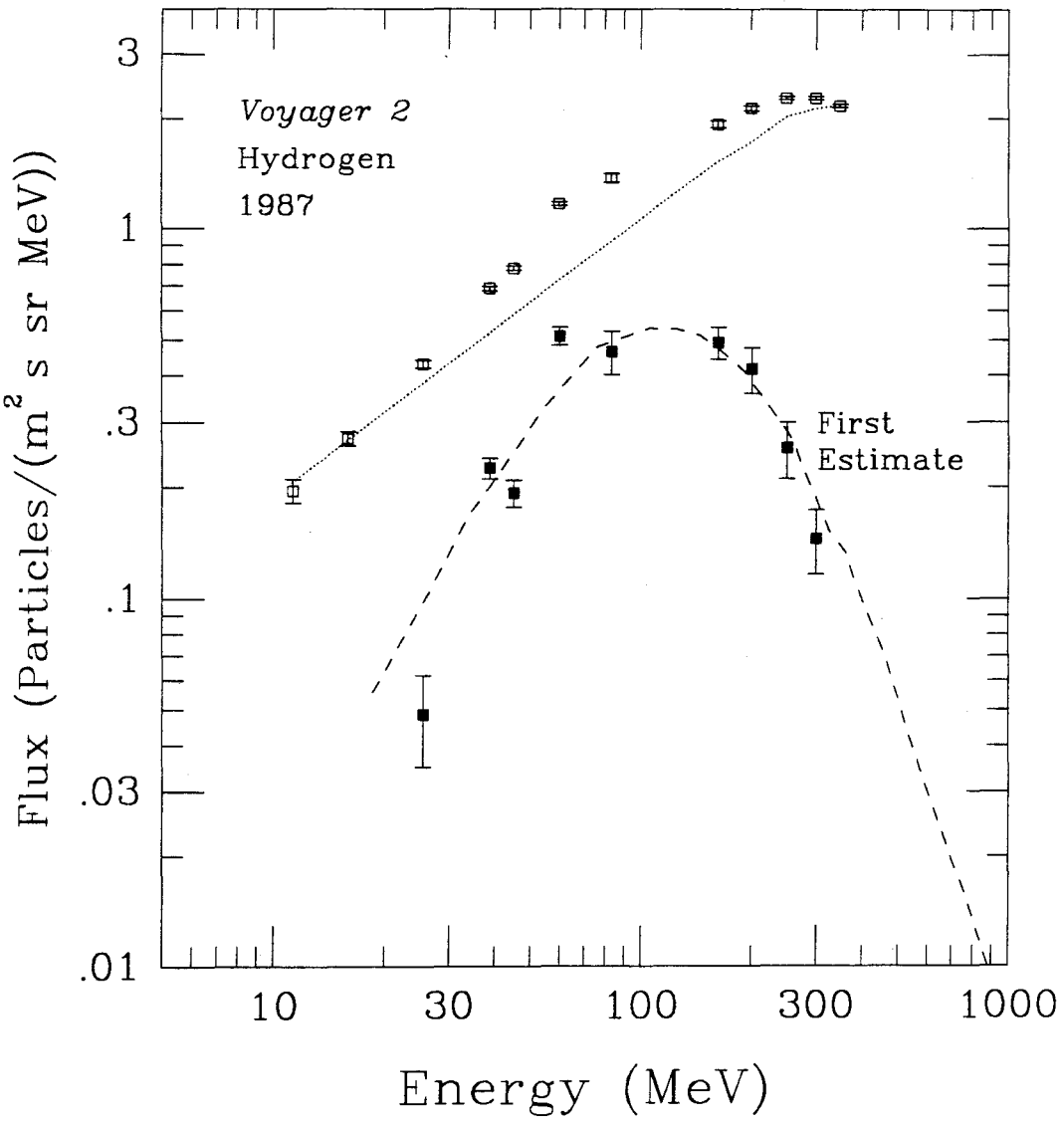
Voyager 2
Hydrogen
1987
First
Estimate
Flux (Particles/(m² s sr MeV))
3
1
.3
.1
.03
.01
10
30
100
300
1000
Energy (MeV)

might be expected because there is likely an unknown anomalous contribution to the 1987 flux at the normalizing energy of 350 MeV. Therefore the term "upper estimate" is really a misnomer, and this dissertation will refer to ACR energy spectra derived with this method as "first estimate" energy spectra.

3.2.2. Lower Estimate of ACR Hydrogen

Although modulation theory is not understood well enough to allow accurate calculation of energy spectra, other observational evidence can be used to estimate the modulation induced changes in the energy spectra. For example, the peaks in the galactic cosmic ray helium energy spectra in Figures 3.1 and 3.2 have shifted downward in energy by $\sim 15\%$ between the 1985 and the 1987 time periods on both *Voyager 1* and *Voyager 2*. This is not to say that the energy spectra of *Voyager 1* and *Voyager 2* are affected by the changing level of solar modulation to the same extent. The spatial separation of the two spacecraft generally results in a difference in the response of the energy spectra to changing modulation. However, the two time periods 1985/261 - 365 and 1987/209 - 313 were picked because the energy shift of the helium GCR energy spectra in this interval was approximately the same for both *Voyagers*.

Because *Voyager 1* has a lower contribution of ACR to the energy spectra of other elements, as shown in the spectra of helium in Figures 3.1 and 3.2, a lower estimate of the anomalous cosmic ray component of hydrogen in *Voyager 2* can be obtained by assuming that there is negligible ACR hydrogen in the *Voyager 1* energy spectra, and thus all of the shape change seen in *Voyager 1* is due to modulation effects. Then a least-squares fit of the *Voyager 1* 1985 energy spectrum to that of 1987 results in an energy shift of $\sim 22\%$ (Figure 3.12). Notice that the shape of the shifted 1985 energy spectrum and the 1987 energy spectrum are similar, but there is still a small systematic

excess from 60 - 200 MeV. If the same energy shift is assumed for the *Voyager 2* GCR hydrogen energy spectra, then an upper estimate of the *Voyager 2* 1987 GCR hydrogen energy spectrum can be made by shifting the *Voyager 2* 1985 energy spectrum downward 22% in energy and normalizing it in flux to the *Voyager 2* 1987 energy spectrum at the highest energy.

Subtracting this shifted energy spectrum from the observed *Voyager 2* 1985 hydrogen energy spectrum results in a lower estimate of the ACR hydrogen flux in *Voyager 2*. This lower estimate is shown for *Voyager 2* in Figure 3.13. The observed 1987 proton energy spectrum is also shown for reference, as is the assumed GCR energy spectrum derived from the 1985 energy spectrum shifted up in flux but down 22% in energy. The dashed line is the fit of the generic anomalous energy spectrum to the lower estimate and gives a peak flux of 0.183 ± 0.010 particles/m^2 s sr MeV at an energy of $\sim$106 MeV, although it is clear that the lower estimate is not well characterized by the shape of the other anomalous components.

However, this method of determining a lower estimate has some major problems. It underestimates the possible anomalous cosmic ray hydrogen flux in 1987 because it assumes that there was no anomalous contribution to the 1985 energy spectrum, there was negligible anomalous flux in the *Voyager 1* 1987 energy spectrum, and that the ACR contribution to the flux at the normalizing energy is also negligible. More importantly, the fact that the assumed galactic cosmic ray energy spectrum in Figure 3.13 is higher than the observed energy spectrum at low energies shows a basic inconsistency in this method. The subtraction of this assumed GCR flux from the observed flux gives negative fluxes below $\sim$25 MeV, which is impossible. If the underlying galactic energy spectrum has retained the same shape between 1985 and 1987, as appears to be the case for *Voyager 1* (Figure 3.12), then clearly the energy shift and flux normalization used in

Figure 3.12

Observed *Voyager 1* hydrogen energy spectrum for the time period 1987/209 - 313. The dotted curve shows the *Voyager 1* 1985/261 - 365 hydrogen energy spectrum shifted downwards in energy by 22% (least-squares fit gives 22±1%) and upwards in flux to match the 1987 energy spectrum.

Figure 3.12

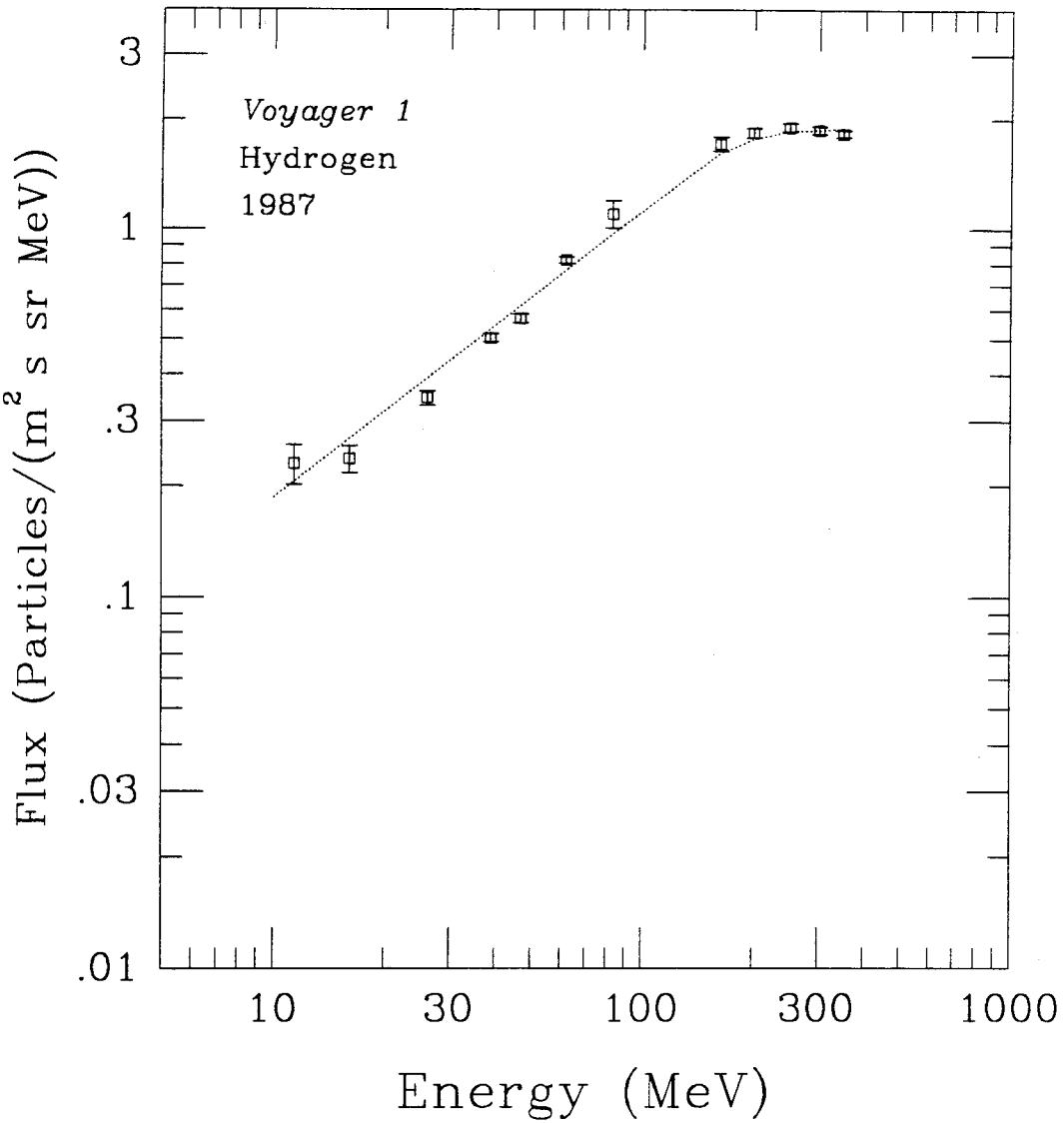
Voyager 1
Hydrogen
1987
Flux (Particles/(m² s sr MeV))
3
1
.3
.1
.03
.01
10
30
100
300
1000
Energy (MeV)

Figure 3.13

Lower estimate of ACR hydrogen for *Voyager 2* 1987/209 - 313 (solid squares). The open squares show the observed *Voyager 2* hydrogen energy spectrum for this time period. The dotted curve illustrates the estimated galactic energy spectrum obtained by shifting the *Voyager 2* 1985/261 - 365 observed hydrogen energy spectrum downwards 22% in energy (as per *Voyager 1*) and upwards in flux. Note that the difference in shape between the 1985 and 1987 energy spectra causes the galactic energy spectrum estimated by this method to be higher in flux than the observed energy spectrum at lower energies. The dashed curve is the least-squares fit of the ACR spectral shape to the lower estimate points.

Figure 3.13

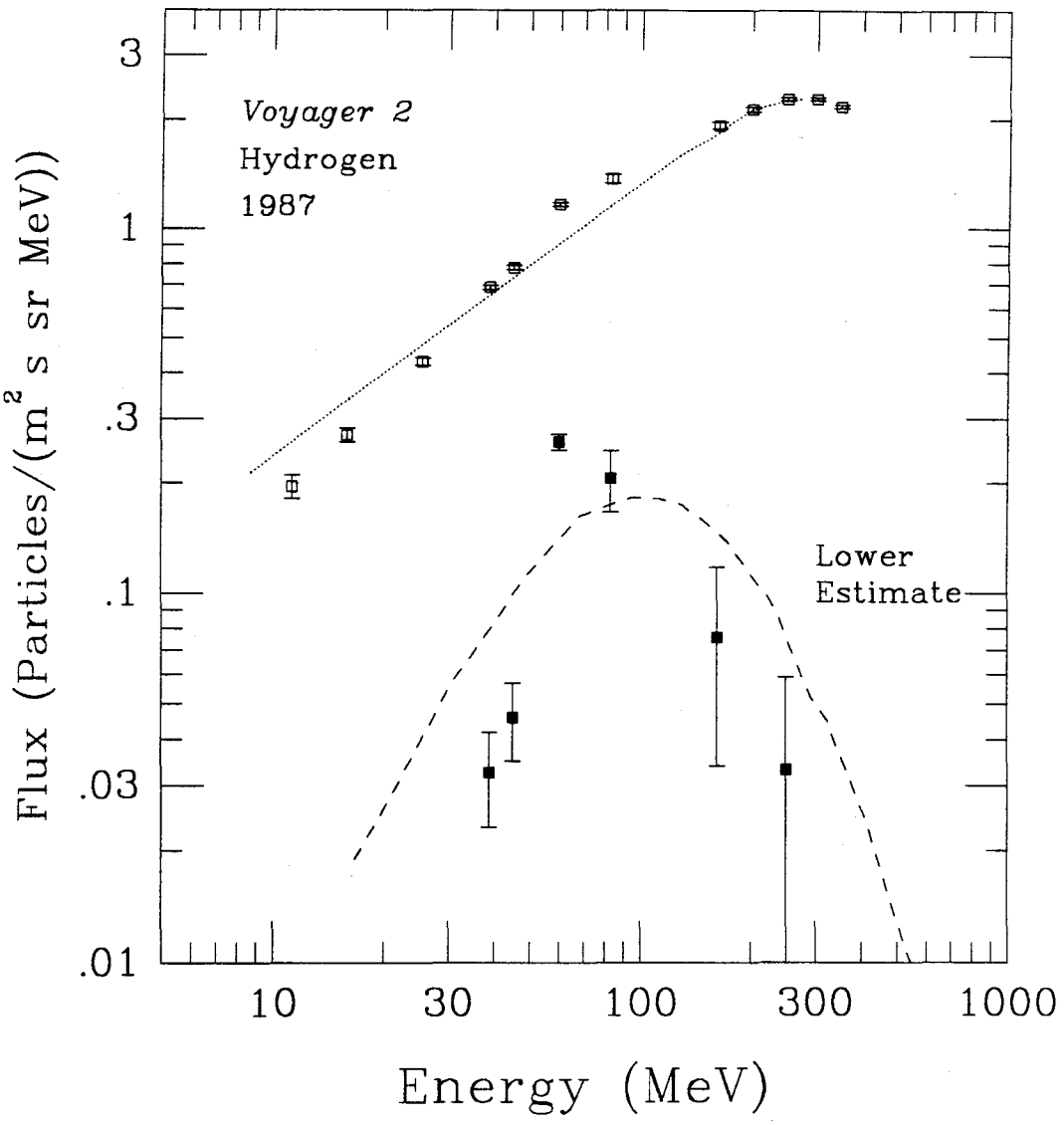
Voyager 2
Hydrogen
1987
Lower
Estimate
Flux (Particles/(m² s sr MeV))
3
1
.3
.1
.03
.01
10
30
100
300
1000
Energy (MeV)

Figure 3.13 overestimates the galactic energy spectrum. However, it is interesting to note that even with this overestimation of the galactic energy spectrum, there is still an excess of flux at $\sim$75 MeV although the shape of the peak is not similar to that of the anomalous components.

If we assume that the 1985 energy spectrum shifted downwards 22% in energy is a reasonable estimate of the underlying galactic energy spectrum, then an explanation for the negative fluxes is that the shift up in flux used is too large. This would be true if there was a non-negligible contribution of ACR hydrogen to the flux at the highest energy, 273 MeV (350 MeV $\times$ 0.78). If the assumed galactic energy spectrum is shifted down in flux until it is no longer above the observed energy spectrum at any point, we obtain an excess (Figure 3.14) that is actually larger than the first estimate of §3.2.1. As with the first estimate, the shape of the excess is similar to the shape of the other ACR components, and gives a peak flux of 0.697$\pm$0.012 at $\sim$146 MeV.

3.2.3. ACR Estimate from Fit of GCR + ACR Energy Spectrum

A different approach to the estimation of the anomalous cosmic ray hydrogen contribution to the energy spectra was also used. If it was assumed that the spectral shapes of both the ACR and GCR components are known, then we can determine the combination of these two shapes, which replicates the shape of the 1987 hydrogen energy spectrum. Because all the known anomalous cosmic ray components have similar shapes, it will be assumed that this common shape (Figure 3.3) applies to the hydrogen ACR component as well.

The spectral shape of the galactic cosmic ray component will come from the hydrogen energy spectrum during the 1985/261 - 365 time period. As explained earlier, the amount of anomalous cosmic ray hydrogen present in the 1985 energy spectrum

should be negligible.

The sum of these two shapes is then fit to the observed energy spectrum allowing the GCR and ACR components to individually shift in both flux in energy. This fit is shown in Figure 3.15 (solid curve) superimposed on the *Voyager 2* 1987 observed energy spectrum. Also shown are the individual GCR (dotted line) and ACR (dashed line) components. The peak ACR hydrogen flux is 0.834±0.012 particles/(m^2 sec sr MeV) and the peak energy is at 134±2 MeV, not very different from the 124 MeV extrapolated from the high Z data in §3.1.2.

When this same method was used on the *Voyager 1* 1987/209-313 hydrogen energy spectrum (Figure 3.6) using the *Voyager 1* 1985 energy spectrum as the galactic shape, a peak ACR hydrogen flux of 0.256±0.021 particles/(m^2 sec sr MeV) was obtained; however, the ACR component peaks at 203±5 MeV. This is significantly higher than expected. In order to reduce problems such as this, the fit was recalculated with some restriction in the parameter space.

The first fit had four parameters: the flux normalization of the ACR component, the energy of the ACR component peak, the flux normalization of the GCR component, and the energy of the GCR component peak. The first two should remain free parameters because they are the goal of this exercise. As seen earlier, the flux normalization of the galactic component is dependent upon the ACR contribution even at the highest energies measured. However, there is an indirect way to calculate the expected peak energy of the GCR component.

It is possible to fit the assumed hydrogen galactic energy spectrum derived from the 1985/261-365 time period to the observed hydrogen energy spectra from other time periods just as was done in §3.2.2 (Figure 3.12). This gives the energy of the hydrogen galactic peak, assuming there is negligible ACR hydrogen. The peak energy of the

Figure 3.14

ACR hydrogen estimate (solid squares) obtained by shifting the assumed galactic energy spectrum of Figure 3.13 downwards in flux (shown by dotted curve) until it no longer lies above the observed 1987 hydrogen energy spectrum (open squares). The dashed curve is the least-squares fit of the ACR spectral shape to the points of the estimate.

Figure 3.14

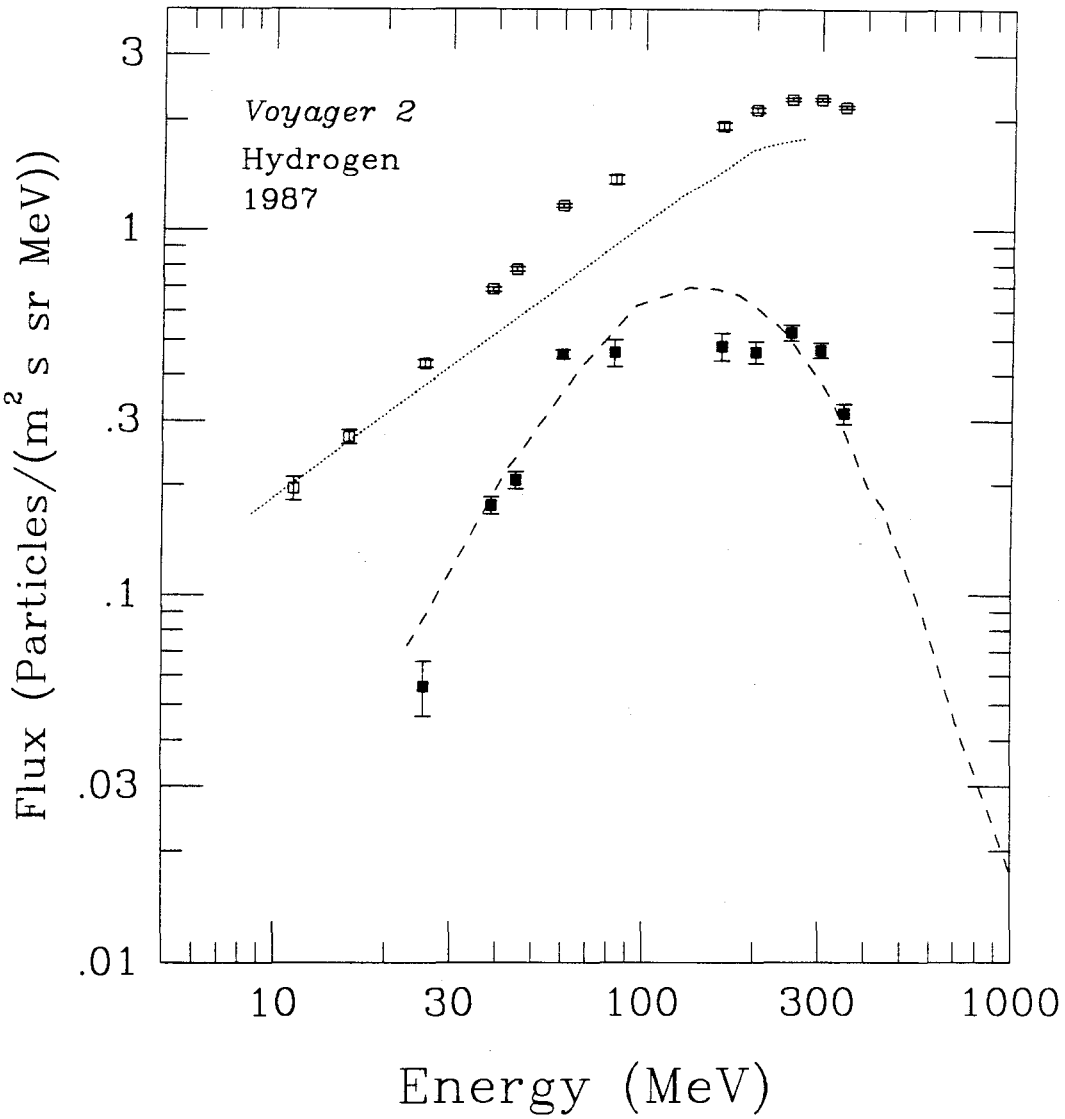
Voyager 2
Hydrogen
1987
Flux (Particles/(m² s sr MeV))
3
1
.3
.1
.03
.01
10
30
100
300
1000
Energy (MeV)

Figure 3.15

Four-parameter fit of GCR + ACR energy spectra (solid curve) to the observed 1987 *Voyager 2* hydrogen energy spectrum (open squares). The dotted curve and the dashed curve show the decomposition of the solid curve into the galactic and anomalous components, respectively.

Figure 3.15

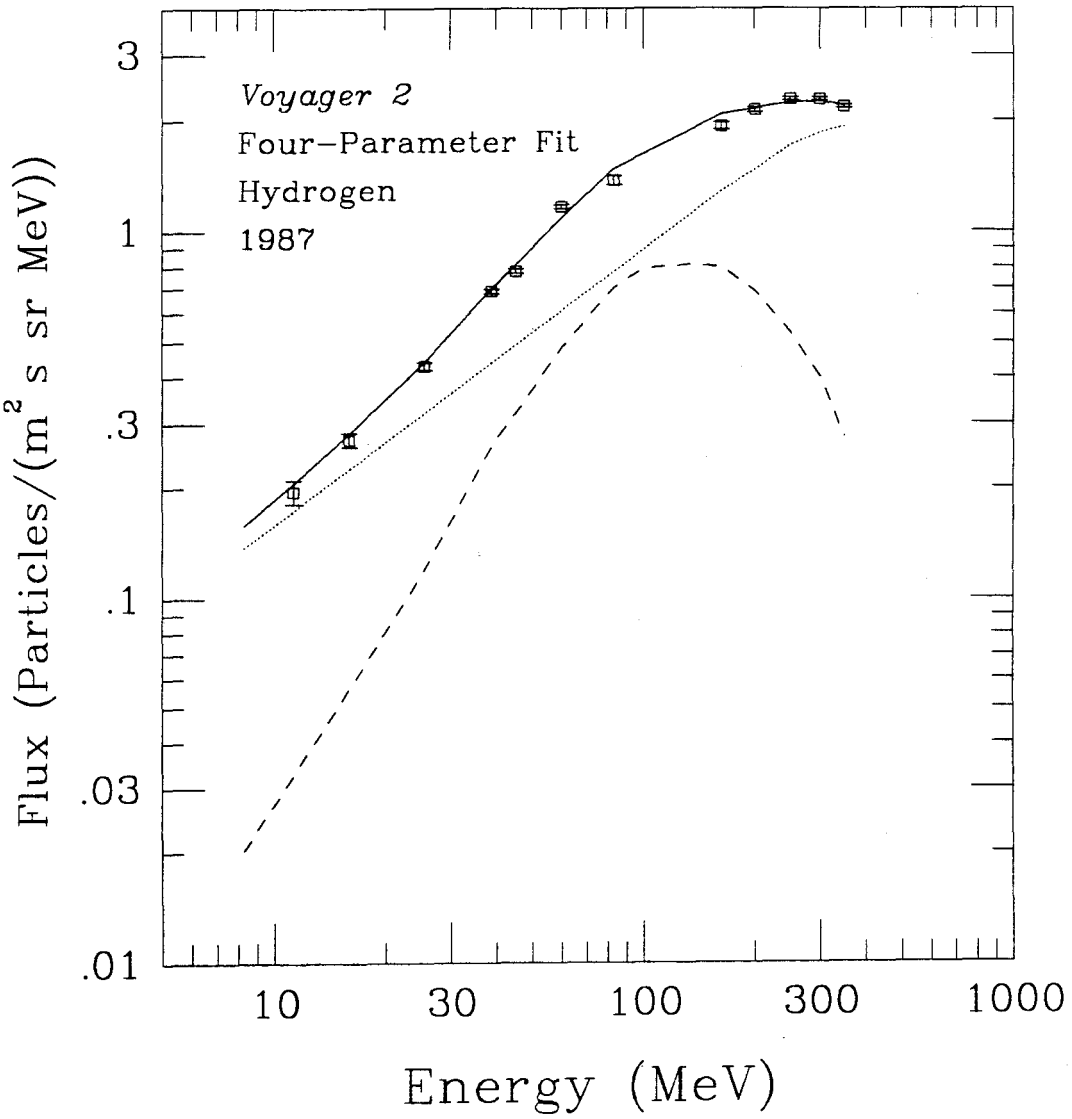
Voyager 2
Four-Parameter Fit
Hydrogen
1987
Flux (Particles/(m² s sr MeV))
3
1
.3
.1
.03
.01
10
30
100
300
1000
Energy (MeV)

helium galactic component can be determined in a similar way. The ability to remove the anomalous cosmic ray contribution from the observed energy spectrum (see §3.1.1) means that helium lacks the ACR complication that is present in the hydrogen spectra. The two values, hydrogen peak energy and helium peak energy, should be correlated, because their modulation history should be very similar. Therefore, an independent method of obtaining the hydrogen peak energy is to determine the correlation between it and the helium peak energy, and then use the easily determined helium peak energy to calculate the hydrogen peak energy for the same time period.

A crossplot of the normalized hydrogen peak energy (with the 1985/261 - 365 time period defined as 1) and the normalized helium peak energy is shown in Figure 3.16 for a series of 104 day periods between the middle of 1983 and the middle of 1988. The earliest time periods fall in the upper right corner, and as time continues the points move downward and to the left, as expected from simple modulation theory. From the middle of 1987 on (open symbols), the apparent hydrogen peak energy undergoes large changes relative to the shift of the helium peak energy, and this effect is larger in *Voyager 2* (squares) than in *Voyager 1* (triangles). This corresponds to the change in shape seen in the observed hydrogen energy spectra. The flux excess at energies slightly less than the peak energy causes the apparent peak energy to shift down. However, it is during these time periods that this fitting method is inappropriate due to the change in spectral shape.

During the earlier time periods (solid symbols) the observed spectra are similar in shape and there is no excess flux. Assuming a linear correlation between the hydrogen and helium energy shift for these time periods, the results are given in the dashed line on Figure 3.16. Thus the normalized peak energy for hydrogen, E_H, can be estimated as $1.027 \times E_{He} - 0.010$.

For the 1987/209 - 313 time period, the galactic helium energy spectrum has shifted down ~16% (normalized helium peak energy = 0.84) because the 1985 time period on *Voyager 1*, and ~13% (normalized helium peak energy = 0.87) on *Voyager 2*. Thus the estimated normalized hydrogen energy peaks are 0.85 and 0.88 for *Voyager 1* and *Voyager 2* respectively. The three-parameter GCR + ACR fit to the *Voyager 1* observed hydrogen energy spectrum with the hydrogen energy shift set to 0.85 is shown in Figure 3.17. This gives an estimate of 0.42±0.02 for the ACR hydrogen peak flux at an energy of 179±7 MeV.

3.2.4. Hydrogen ACR Component

The peak fluxes of the anomalous cosmic ray hydrogen from all the estimates for *Voyager 1* and *Voyager 2* are plotted in Figure 3.18. Except for the lower estimate (estimate 2 in Figure 3.18), which clearly underestimates the ACR hydrogen flux, it is difficult to determine which of the estimate should be taken as correct. The fact that the estimates differ by more than the calculated uncertainties shows that the uncertainties in the methods are larger than the uncertainties calculated for the individual methods. Even so, all of the estimations give similar values of excess flux, and the excesses peak at similar energies.

For the subsequent analysis, the lower estimate of §3.2.2 (estimate 2 in Figure 3.18) will be disregarded, but all the other estimates will be given equal weight. The assumed value of the peak flux of anomalous cosmic ray hydrogen will then be taken at the midpoint of a range, which includes all the estimates, and the uncertainty will span the entire range. This is shown in the last column on Figure 3.18. Thus the value for the ACR hydrogen peak flux will be 0.33±0.12 particles/m^2 s sr MeV for

Figure 3.16

Normalized peak energy of the observed hydrogen energy spectra vs. the normalized peak energy of the galactic helium energy spectra. Both *Voyager 1* (triangles) and *Voyager 2* (squares) are plotted. The solid symbols show the points that were used to calculate a linear relationship (shown by the dashed line).

Figure 3.16

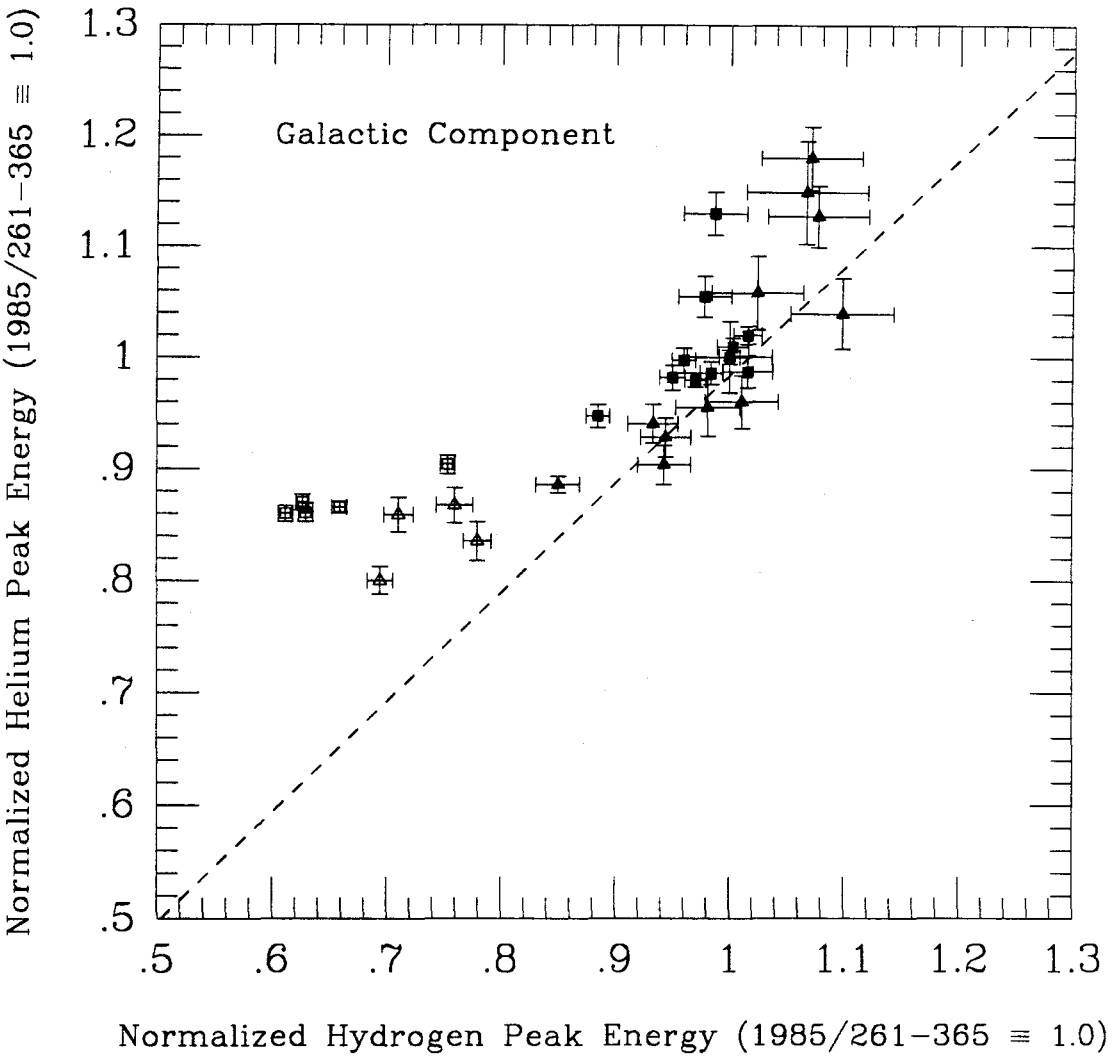
Galactic Component
Normalized Helium Peak Energy (1985/261-365 ≡ 1.0)
Normalized Hydrogen Peak Energy (1985/261-365 ≡ 1.0)
1.3
1.2
1.1
1
.9
.8
.7
.6
.5
.5
.6
.7
.8
.9
1
1.1
1.2
1.3

Figure 3.17

Three-parameter fit of GCR + ACR energy spectra (solid curve) to the observed 1987 *Voyager 1* hydrogen energy spectrum (open squares). The dotted curve and the dashed curve show the decomposition of the solid curve into the galactic and anomalous components respectively. Unlike the fit in Figure 3.15, the peak energy of the galactic component is not a parameter, but is determined from the peak energy of the helium galactic energy spectrum.

Figure 3.17

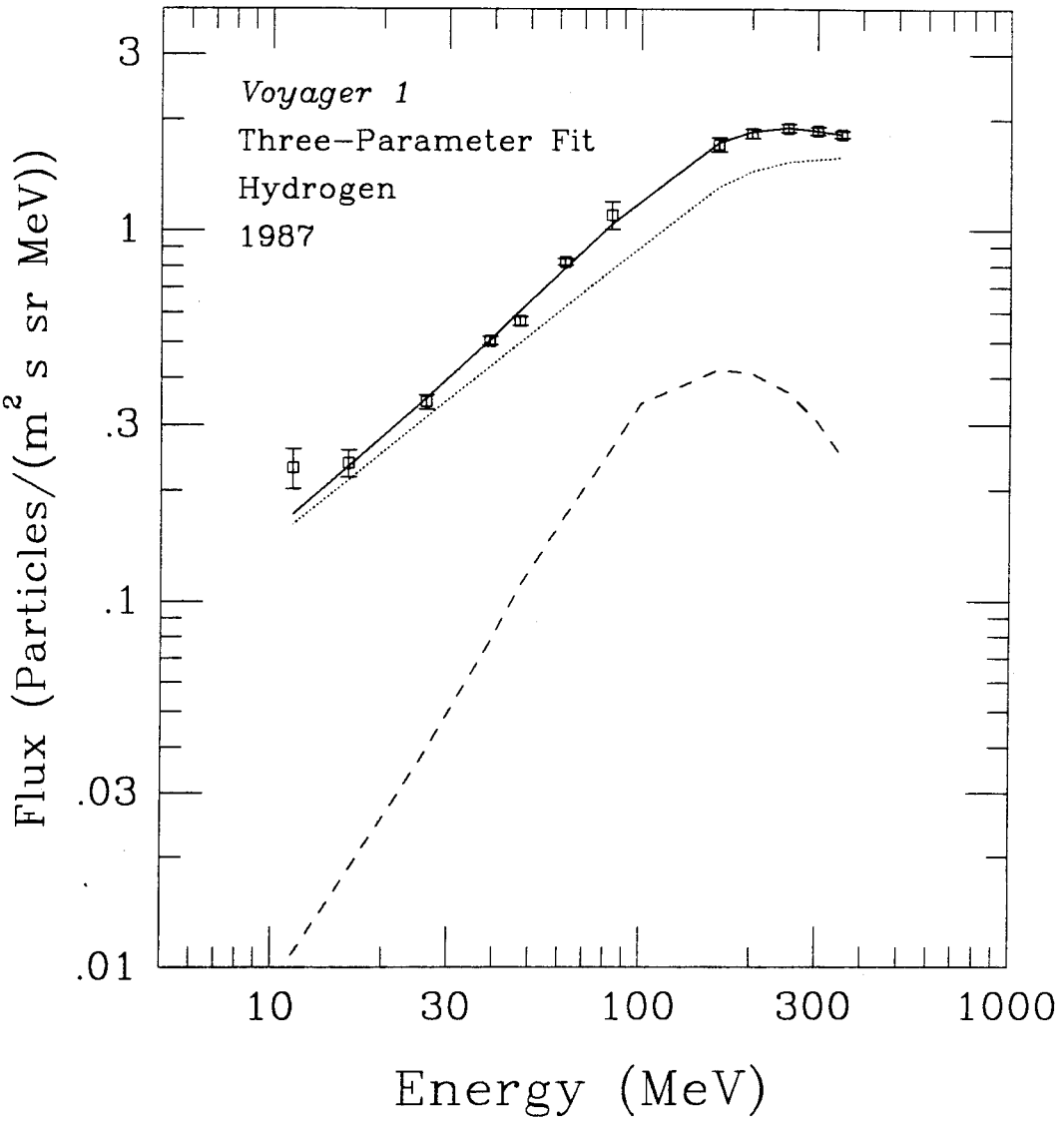
Voyager 1
Three-Parameter Fit
Hydrogen
1987
Flux (Particles/(m² s sr MeV))
3
1
.3
.1
.03
.01
10
30
100
300
1000
Energy (MeV)

Figure 3.18

Comparison of the various 1987 hydrogen ACR estimates for *Voyager 1* (open squares) and *Voyager 2* (solid squares). The first estimates of §3.2.1 are in column 1. The lower estimates of §3.2.2 for *Voyager 2* are in columns 2 and 3, with estimate 2 corresponding to normalization at the highest energy and estimate 3 corresponding to the normalization that does not give negative fluxes. Estimate 4 is the four-parameter GCR + ACR fit, and estimate 5 is the three-parameter GCR + ACR fit, both from §3.2.3. The last column is a range that includes all of the other estimates except for 2, which clearly underestimates the ACR hydrogen flux. The points in the last columns are at the midpoint of the range.

Figure 3.18

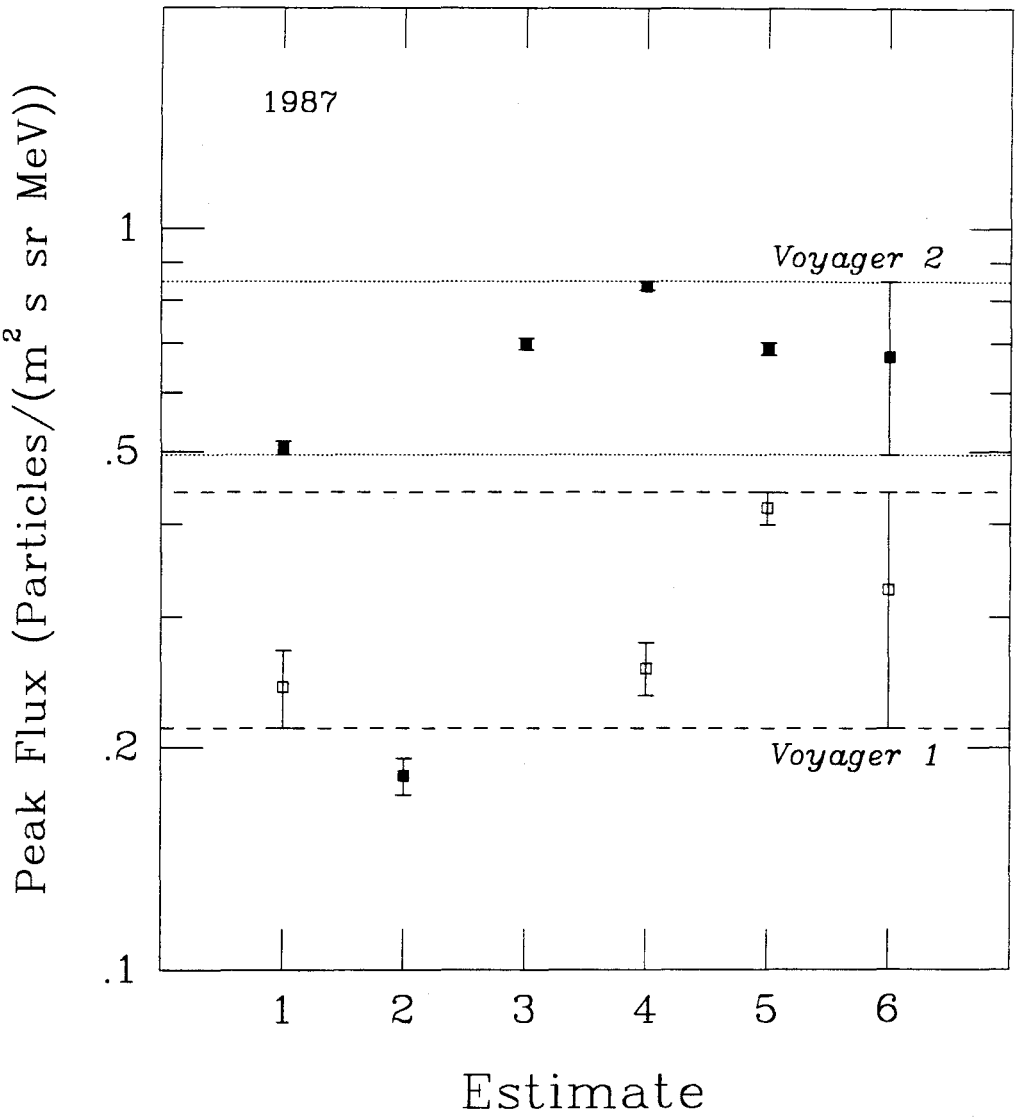
1987
Voyager 2
Voyager 1
Peak Flux (Particles/(m² s sr MeV))
1
.5
.2
.1
1
2
3
4
5
6
Estimate

Voyager 1 and 0.67±0.18 particles/m^2 s sr MeV for *Voyager 2*. Note that the ratio of the *Voyager 2* peak flux to the *Voyager 1* peak flux is close to 2, which is consistent with all the ACR components of all the other elements. Our previously published (Christian *et al.* 1988) upper estimates (now called first estimates) were $\sim$ 0.3 particles/m^2 s sr MeV for *Voyager 1* and $\sim$ 0.6 particles/m^2 s sr MeV for *Voyager 2*, which fall within the new ranges.

3.2.5. After Solar Minimum

Following this 1987 time period, nearly a year's worth of data has been acquired and analyzed. During this year the solar activity has been increasing, and correspondingly, so has the level of solar modulation. The increase in solar modulation has caused the expected decrease in fluxes for both the galactic and anomalous components, and the relative contribution of anomalous flux has also decreased. Just as the *Voyager 1* energy spectra were less affected by the decrease in solar modulation because of *Voyager 1*'s position above the ecliptic (§3.1.1), the energy spectra are also less affected by the increase in modulation. This can be seen by comparing the 1988/105-209 helium energy spectra of *Voyager 1* (Figure 3.19) and *Voyager 2* (Figure 3.20) to the helium energy spectra of Figures 3.1 and 3.2.

These changes have to be examined closely in the hydrogen energy spectra because of the mixing of the anomalous and galactic cosmic rays. Figure 3.21 is the *Voyager 1* hydrogen energy spectrum divided by energy for the time period 1988/105 - 209. The dashed curve is the shape of the 1985/261 - 365 *Voyager 1* energy spectrum shifted up in flux to match the 1988 energy spectrum at the highest energy (350 MeV) as was done in Figure 3.8. The dotted curve illustrates the hydrogen spectral shape during the 1987/209 - 313 time period and has been shifted downwards in flux to again match the

1988 energy spectrum at 350 MeV.

The excess flux in 1988 relative to the 1985 energy spectrum is comparable or slightly less than the flux excess observed in 1987 for the energy range $\sim$40 MeV to 350 MeV. This is consistent with *Voyager 1* energy spectra for other elements that show an ACR component in 1988, which have not been as reduced in flux level as the ACR components of *Voyager 2*.

The *Voyager 2* 1988 flux-divided by energy plot is Figure 3.22. There is still an excess flux relative to the 1985 energy spectrum, but the excess is noticeably less than that of the 1987 time period. This is again consistent with the changes seen in the other anomalous components.

Estimates of the ACR contribution to the energy spectra of Figures 3.21 and 3.22 have been calculated using both the first estimate approach (§3.2.1) and the GCR + ACR fit (§3.2.3). Figure 3.23 shows the new values obtained for the assumed ACR flux in both *Voyager 1* and *Voyager 2* for this 1988 time period, as well as the range of estimates obtained from the 1987 energy spectra. It can be seen that both the *Voyager 1* and *Voyager 2* ACR hydrogen fluxes have decreased, and that the *Voyager 2* ACR contribution has decreased by a larger amount to the point, so that it is now similar to *Voyager 1*. This is exactly the trend expected for an ACR component. The ACR component of helium, for example, has decreased by a factor of $\sim$2 for *Voyager 1* between 1987 and 1988, but by a factor of $\sim$5 for *Voyager 2*, resulting in similar fluxes of ACR helium during the 1988 time period.

The galactic components of hydrogen and helium show similar trends during this portion of the solar cycle. The *Voyager 2* galactic fluxes have decreased at a faster rate than *Voyager 1* (although not as fast as the anomalous fluxes) to the point where the *Voyager 1* galactic fluxes for the 1988 time period are actually slightly higher than in

Figure 3.19

Voyager 1 helium energy spectrum from the time period 1988/105 - 209. The dashed curve shows the shape of the anomalous cosmic ray energy spectrum, and the dotted curve represents the galactic cosmic ray energy spectrum.

Figure 3.19

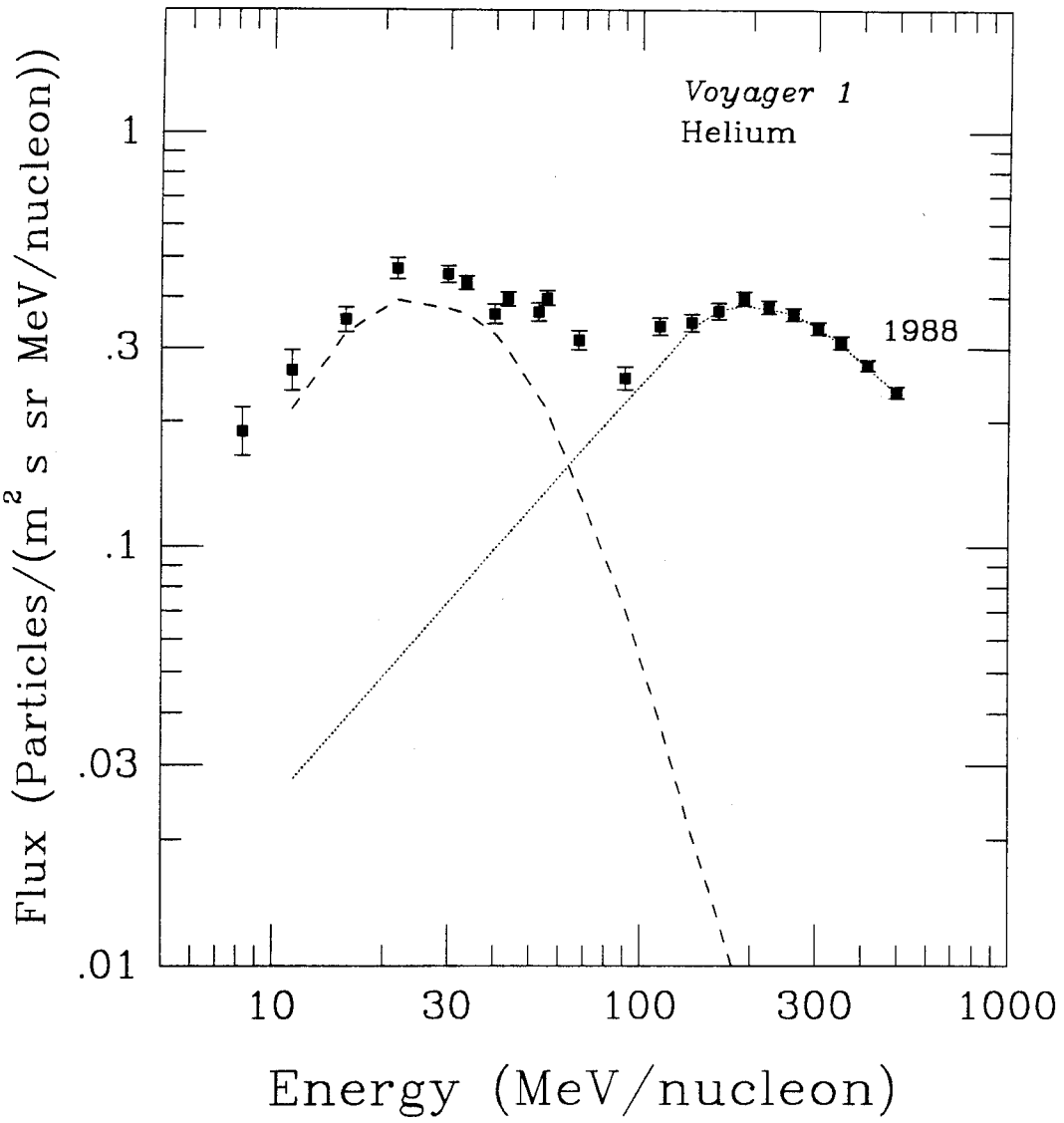
Voyager 1
Helium
1988
1
.3
.1
.03
.01
10
30
100
300
1000
Flux (Particles/(m² s sr MeV/nucleon))
Energy (MeV/nucleon)

Figure 3.20

Voyager 2 helium energy spectrum from the time period 1988/105 - 209. The dashed curve shows the shape of the anomalous cosmic ray energy spectrum, and the dotted curve represents the galactic cosmic ray energy spectrum.

Figure 3.20

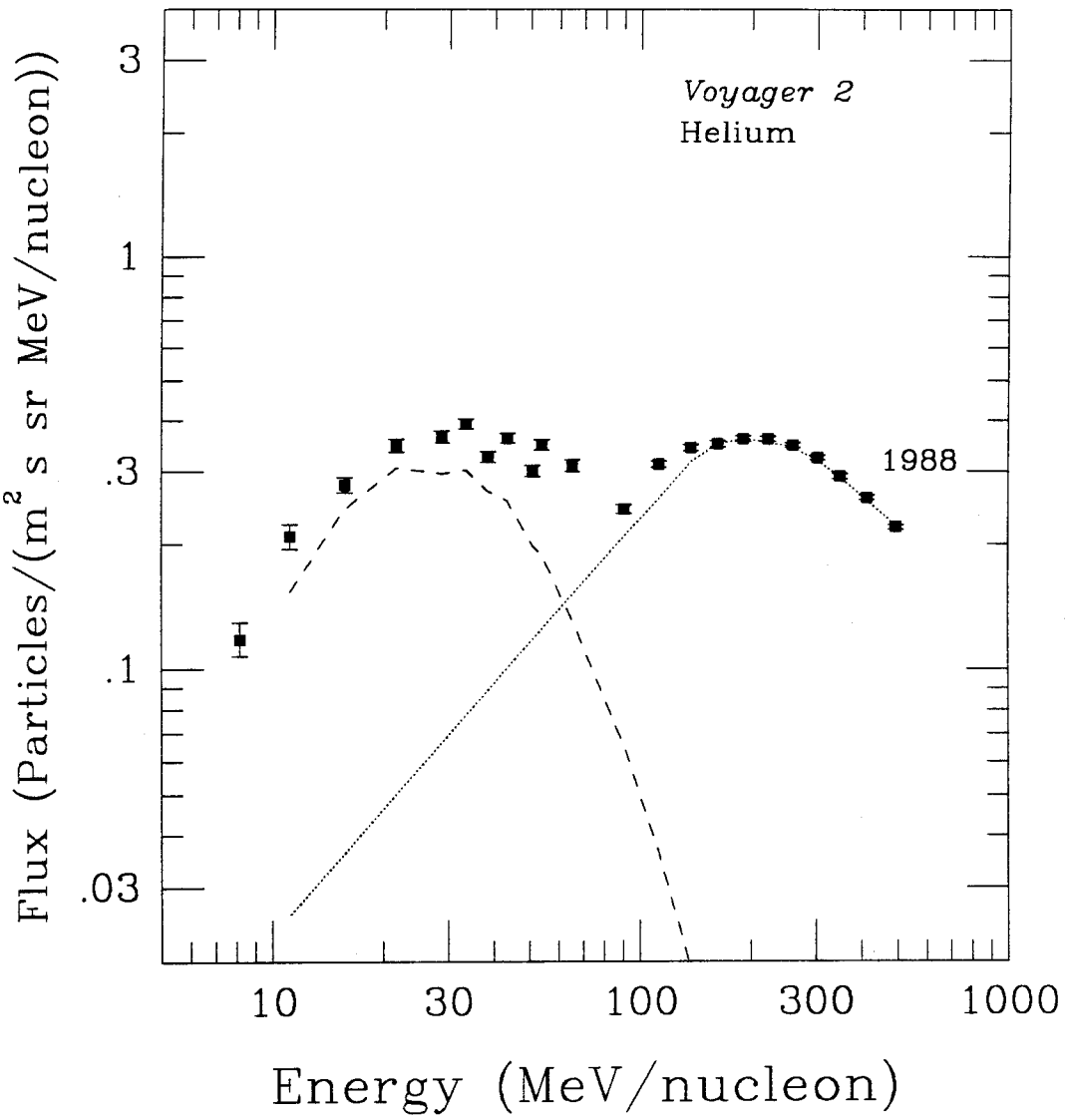
Voyager 2
Helium
1988
3
1
.3
.1
.03
10
30
100
300
1000
Flux (Particles/(m² s sr MeV/nucleon))
Energy (MeV/nucleon)

Figure 3.21

Voyager 1 hydrogen energy spectrum from the period 1988/105-209 with the fluxes divided by energy to flatten the energy spectrum. The dashed and dotted curves represent the shape of the 1985 and 1987 hydrogen energy spectrum respectively, scaled to match the 1988 energy spectrum at the highest measured energy.

Figure 3.21

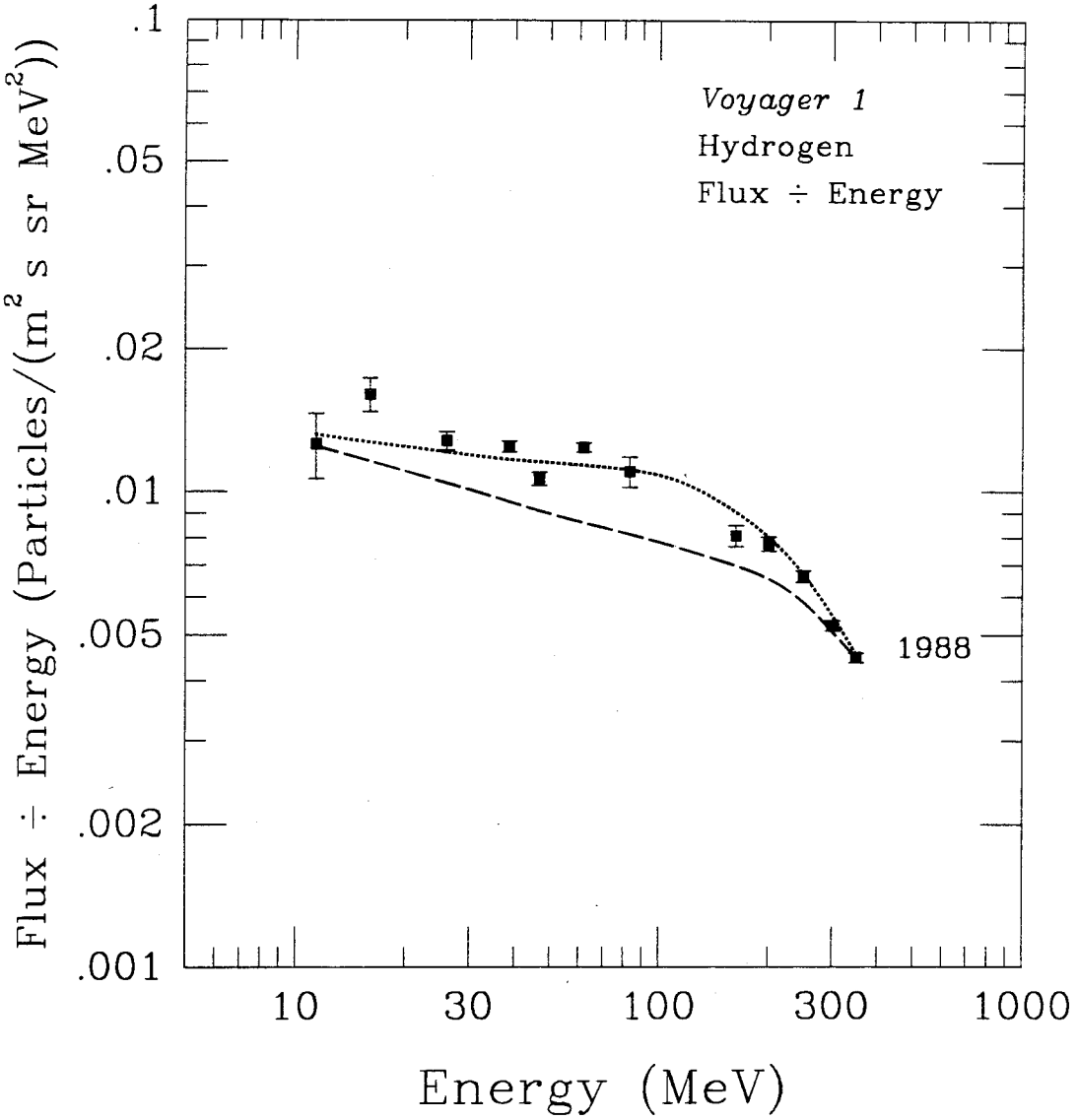
Voyager 1
Hydrogen
Flux ÷ Energy
1988
Flux ÷ Energy (Particles/(m² s sr MeV²))
.1
.05
.02
.01
.005
.002
.001
10
30
100
300
1000
Energy (MeV)

Figure 3.22

Voyager 2 hydrogen energy spectrum from the period 1988/105-209 with the fluxes divided by energy to flatten the energy spectrum. The dashed and dotted curves represent the shape of the 1985 and 1987 hydrogen energy spectrum respectively, scaled to match the 1988 energy spectrum at the highest measured energy and illustrate the change in spectral shape that has occurred.

Figure 3.22

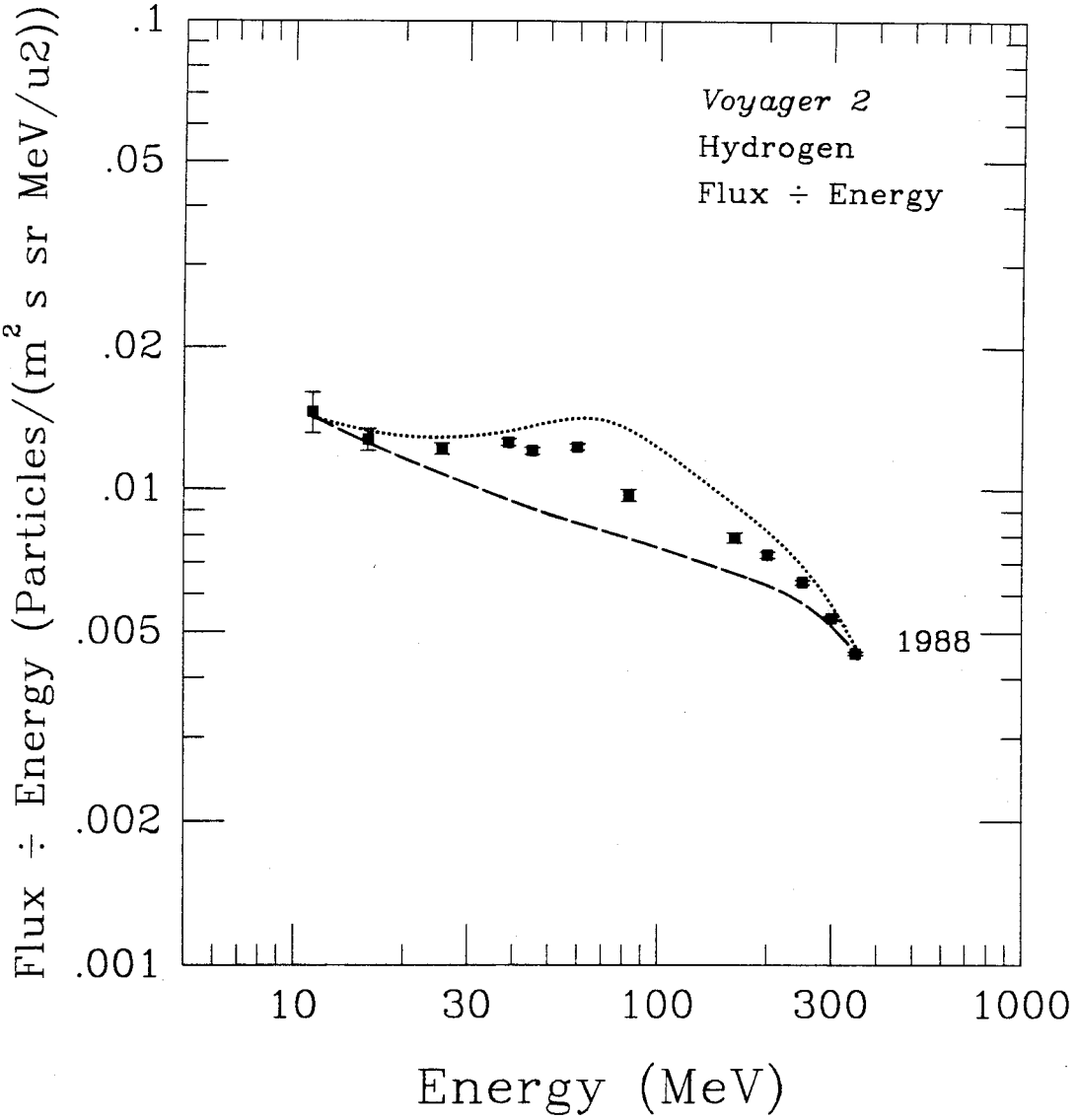
Voyager 2
Hydrogen
Flux ÷ Energy
1988
Flux ÷ Energy (Particles/(m² s sr MeV/u2))
.1
.05
.02
.01
.005
.002
.001
10
30
100
300
1000
Energy (MeV)

Figure 3.23

Comparison of the 1988 hydrogen ACR estimates for *Voyager 1* (open squares) and *Voyager 2* (solid squares). The first estimates are in column 1 (see §3.2.1). Estimate 2 is the four-parameter GCR + ACR fit, and estimate 3 is the three-parameter GCR + ACR fit (see §3.2.3). The fourth column contains ranges that include all three estimates, with the symbols plotted at the median of the range. On the far right are the 1987 estimate ranges from Figure 3.18 for comparison.

Figure 3.23

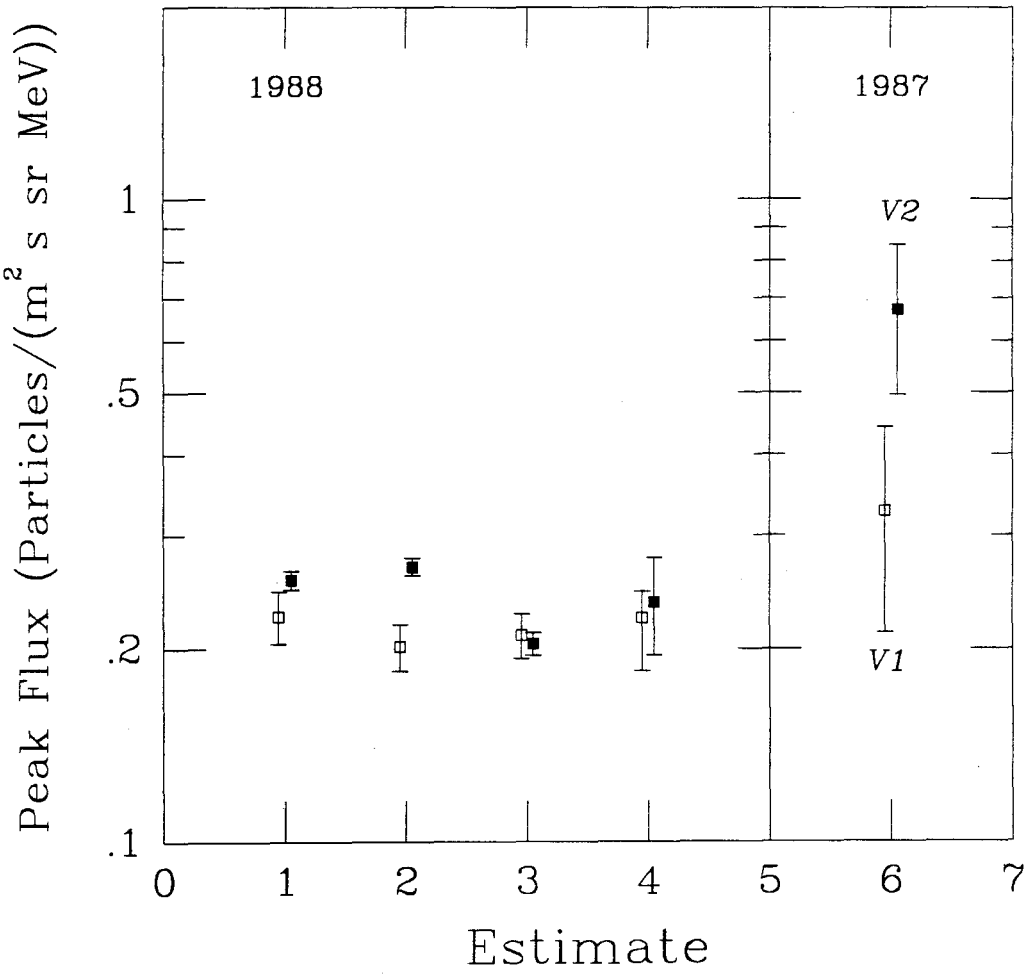
1988
1987
V2
V1
Peak Flux (Particles/(m² s sr MeV))
1
.5
.2
.1
0
1
2
3
4
5
6
7
Estimate

Voyager 2. Because the galactic and anomalous components show similar trends, the 1988 observations do not clearly distinguish between the two possible causes of the hydrogen flux excess: modulation and ACR hydrogen. However, the rate of the decrease in the excess flux is more characteristic of the anomalous components than of the galactic cosmic rays.

3.3. Carbon

In order to further investigate the possibility that the spectral changes of Figures 3.8, 3.9, 3.21, and 3.22 might be due to a peculiar modulation effect rather than to anomalous cosmic ray hydrogen, we have examined the spectral shapes of other galactic cosmic ray nuclei. As described in §3.1.2, any spectral shape change due to modulation will occur at a different energy for heavier nuclei than for hydrogen. However, because the fully ionized nuclei heavier than hydrogen have approximately the same mass per charge, Equation (3.1) indicates that the heavier elements will all exhibit spectral features at the same energy per nucleon. To get the scaling of these features, the spectral peaks of hydrogen from Figures 3.5 and 3.6 can be compared to those of helium in Figures 3.1 and 3.2. Thus, for *Voyager 2* in 1987, the maximum GCR hydrogen flux in Figure 3.7 occurs at $\sim$280 MeV, while the maximum GCR helium flux occurs at $\sim$210 MeV/nucleon in Figure 3.2. As a result, if the excess hydrogen flux at 100 MeV was due to modulation, a similar excess would be expected at $\sim$75 MeV/nucleon for heavier galactic cosmic ray nuclei. However, most of the heavier elements, such as helium, have large anomalous contributions to the flux at 75 MeV/nucleon. Carbon is the only sufficiently abundant heavier nucleus that is relatively free of contamination by the anomalous component at this energy (Cummings and Stone 1987).

Figures 3.24 and 3.25 have, correspondingly, the *Voyager 1* and *Voyager 2* carbon flux-divided-by-energy spectra for the time periods 1985/261 - 1986/105, 1987/105 - 313, and 1988/1 - 209. The time periods are double the length of those for hydrogen to reduce the statistical uncertainty for the less abundant carbon. Averaging over these longer time periods for hydrogen would dilute the observed spectral shape change seen in hydrogen by only 10% to 15%. The dashed curves show that, except for an increase in the ACR component at low energies (Cummings and Stone 1988), these energy spectra are consistent with there being no change in the shape of the galactic cosmic ray energy spectrum at ~75 MeV/nucleon between 1985 and 1988. Comparison of Figures 3.24 and 3.25 to Figures 3.8, 3.9, 3.21, and 3.22 thus suggests that the excess flux in *Voyager 1* and *Voyager 2* hydrogen is not solely the result of the modulation of a purely galactic cosmic ray energy spectrum.

3.4. Previous Solar Cycle

There is another aspect that should be examined to further the understanding of the problem of ACR hydrogen. Although the solar modulation was too intense for observations of the hydrogen and helium ACR components during the years just prior to 1985, the eleven years of *Voyager* flight allow us some observations during the previous period of minimum modulation. There are several problems with the analysis of data from shortly after launch. The radial gradients for both anomalous and galactic cosmic rays are positive (i.e., the flux increases with radius) and the ACR radial gradient is larger than the GCR radial gradient, resulting in a lesser contribution of the anomalous cosmic rays in observations close to the sun. Also, the two *Voyager* launches in 1977 were after the period of minimum solar activity in 1976, which also

Figure 3.24

Voyager 1 carbon energy spectra from the time periods 1985/261 - 1986/105, 1987/105 - 313, and 1988/1 - 209 with the fluxes divided by energy to flatten the galactic portion of the energy spectrum (>30 MeV/nucleon). The 1987 fluxes have been multiplied by 3 and the 1988 fluxes by 10 to separate the time periods. The dashed curves show that the energy spectra are consistent with there being no change in the galactic cosmic ray spectral shape in this energy range.

Figure 3.24

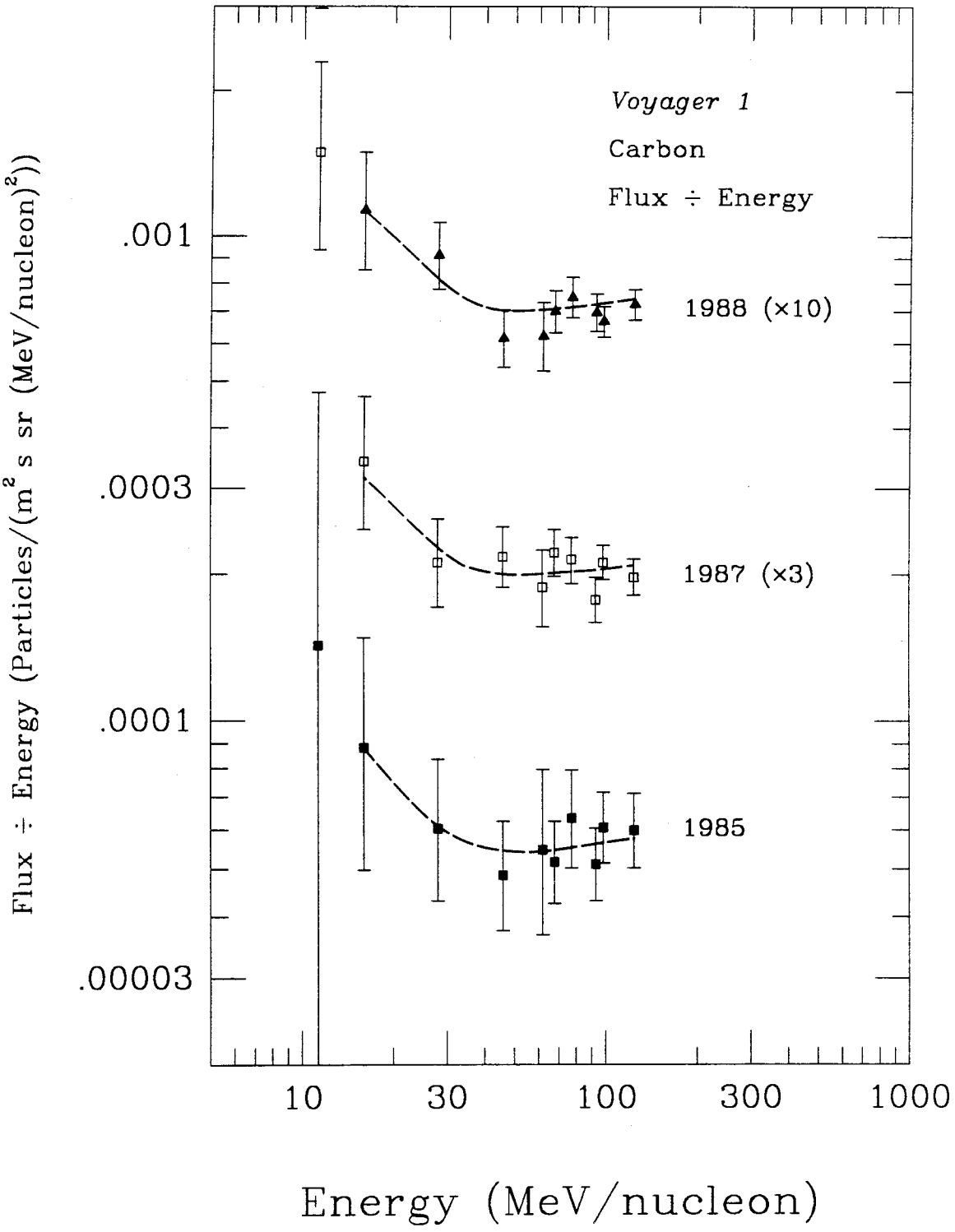
Voyager 1
Carbon
Flux ÷ Energy
1988 (×10)
1987 (×3)
1985
.001
.0003
.0001
.00003
10
30
100
300
1000
Flux ÷ Energy (Particles/(m² s sr (MeV/nucleon)²))
Energy (MeV/nucleon)

Figure 3.25

Voyager 2 carbon energy spectra from the time periods 1985/261 - 1986/105, 1987/105 - 313, and 1988 - 209 with the fluxes divided by energy to flatten the galactic portion of the energy spectrum (>30 MeV/nucleon). The 1987 fluxes have been multiplied by 3 and the 1988 fluxes by 10 to separate the time periods. The dashed curves show that the energy spectra are consistent with there being no change in the galactic cosmic ray spectral shape in this energy range.

Figure 3.25

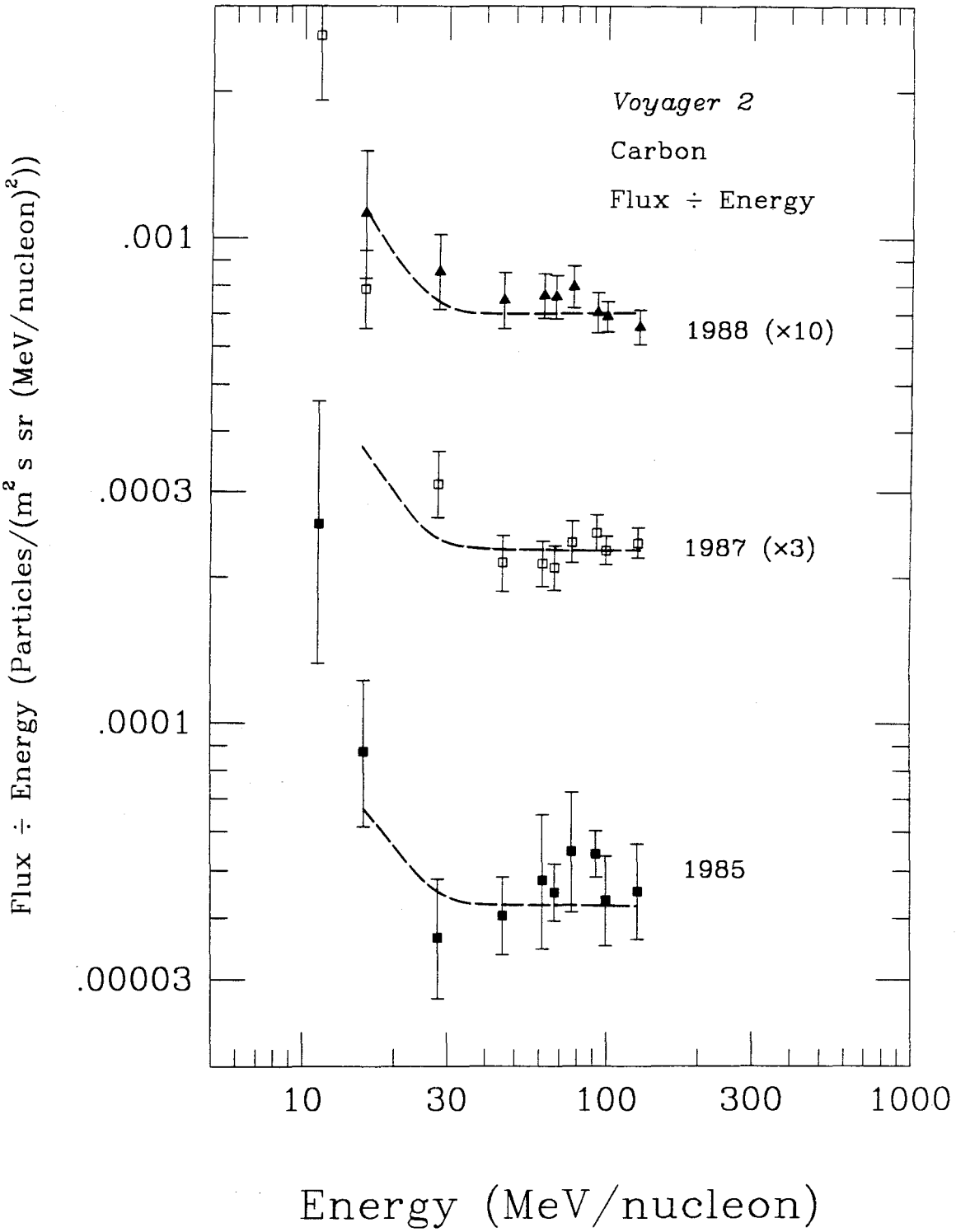
Voyager 2
Carbon
Flux ÷ Energy
1988 (×10)
1987 (×3)
1985
.001
.0003
.0001
.00003
10
30
100
300
1000
Flux ÷ Energy (Particles/(m² s sr (MeV/nucleon)²))
Energy (MeV/nucleon)

reduces the observed fluxes of both the anomalous and galactic components.

In addition to the decrease in cosmic ray intensities, the contribution of solar energetic particles is much larger when the *Voyagers* were close to the sun. The flux of solar energetic particles also changes on short time scales due to solar flares and other energetic events. This restricts the use of long integration times, and so the following analysis will use accumulation time periods of 26 days, and only for the most abundant elements: hydrogen and helium. The shorter time periods result in larger statistical uncertainties. However, because the *Voyagers* are spatially close, they observe similar energy spectra, and statistics can be improved by adding together the energy spectra from both *Voyagers.*

3.4.1. Helium

Figure 3.26 shows helium energy spectra for *Voyager 1* plus *Voyager 2* during the time periods 1977/335 - 361 and 1978/353 - 1979/14. During the 1977 time period the two *Voyagers* were at a radial distance of $\sim$1.7 AU and at about the same longitude with *Voyager 1* at $\sim 2^\circ$ N Heliographic latitude and *Voyager 2* at $\sim 5.5^\circ$ N latitude. At the beginning of 1979 *Voyager 1* was at 4.9 AU and *Voyager 2* was at 4.5 AU and the latitudes were -5° for *Voyager 1* and -4° for *Voyager 2.* The separation of the energy spectra into ACR and GCR components proceeded as described in §3.1.1. Once again it is clear that the anomalous cosmic rays are affected by a changing modulation to a greater extent than the galactic cosmic rays.

However, even though the 1977 time period has the minimum modulation level for *Voyager* during the early part of the flight, that level of modulation is only slightly less than the 1985 time period of Figures 3.1 and 3.2. Because of this, neither the absolute fluxes nor the relative contributions of the ACR fluxes approach the level seen in 1987.

This should make the detection of the small anomalous cosmic ray hydrogen component extremely difficult.

3.4.2. Hydrogen

The large SEP component is easy to see in the combined *Voyager 1* and *Voyager 2* hydrogen energy spectra for the time periods 1977/335 - 361 and 1978/353 - 1979/14 (Figure 3.27). These two periods were picked because the solar component was relatively small, but the SEPs still dominate the flux below $\sim$25 MeV. The solar energetic particle component was removed by fitting the energy spectra between 7.5 MeV and 75 MeV to the sum of the two power laws, one for the SEPs and one for the low energy portion of the GCR energy spectrum. Even though the solar energetic particle energy spectra are well fit by a power law, the energies with an SEP contribution of more than 50% will be left out of the subsequent analysis due to uncertainties in the SEP subtraction.

Figure 3.28 shows the 1977 and 1979 standard flux-divided-by-energy spectra for the hydrogen non-SEP component in both *Voyagers*. There is an excess in the lower energies in the 1977 (less modulated) energy spectra, but unfortunately the solar energetic particles restrict the energy range that can be analyzed. This makes it impossible to tell whether this excess is due to a separate peak, in which case there would be no excess at the lower energies, or whether this excess is the expected increase in lower rigidity particles caused by the decrease in solar modulation. Along with the dashed line in Figure 3.28 representing the 1978/1979 energy spectra shifted up in flux is a dotted line that shows the 1978/1979 energy spectra shifted up in flux, but shifted down 14% in energy to represent the shifting of the energy spectra. The solid line shows that the 1977 and 1978/1979 energy spectra may be similar in shape at slightly different

Figure 3.26

Combined *Voyager 1* and *Voyager 2* helium energy spectra for the time periods 1977/335 - 361 and 1978/353 - 1979/14. The dashed curves show the shape of the anomalous cosmic ray energy spectra, and the dotted curves represent the galactic cosmic ray energy spectra.

Figure 3.26

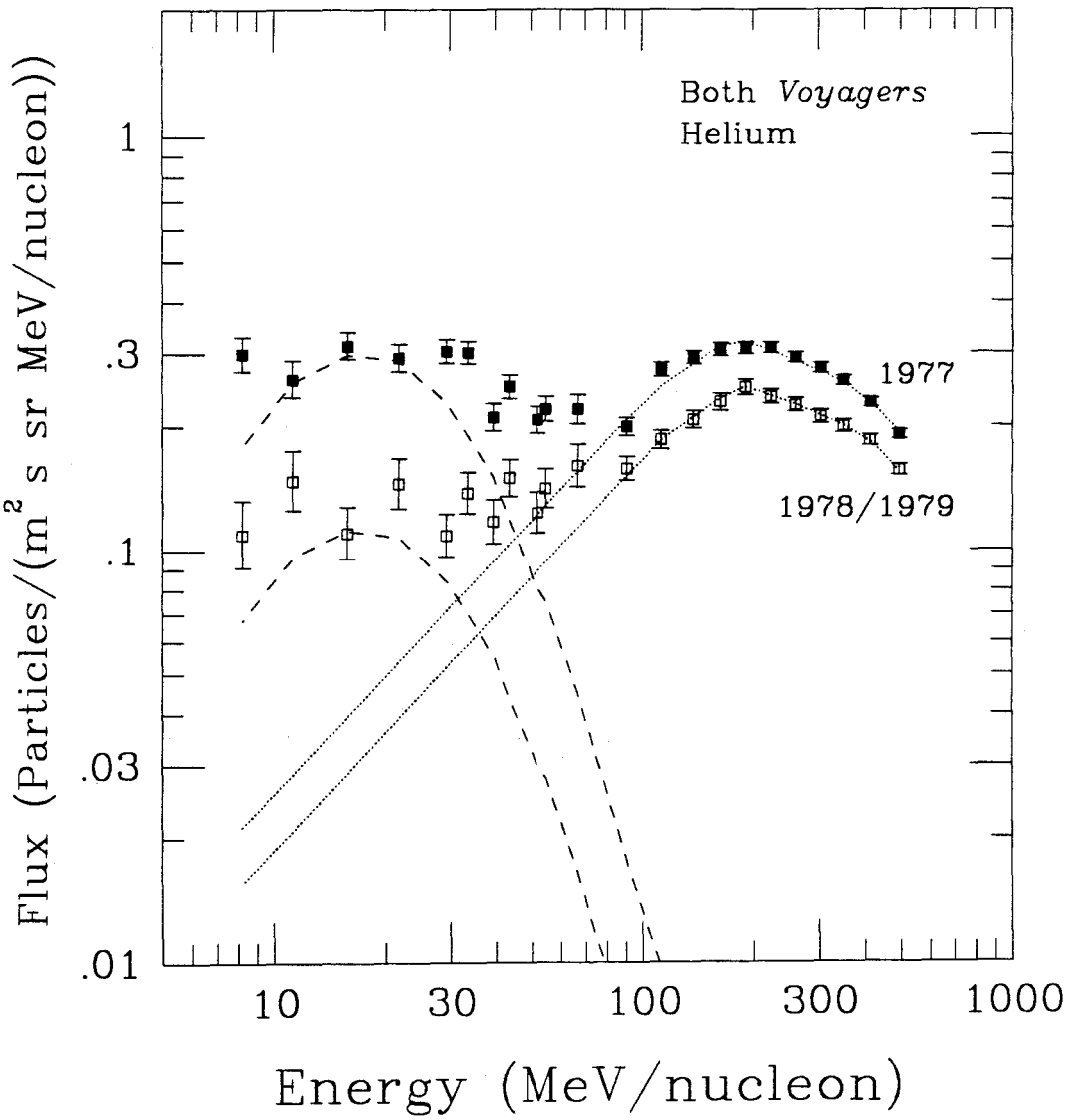
Both *Voyagers*
Helium
1977
1978/1979
Flux (Particles/(m^2 s sr MeV/nucleon))
1
.3
.1
.03
.01
10
30
100
300
1000
Energy (MeV/nucleon)

Figure 3.27

Combined *Voyager 1* and *Voyager 2* hydrogen energy spectra for the time periods 1977/335 - 361 and 1978/353 - 1979/14.

Figure 3.27

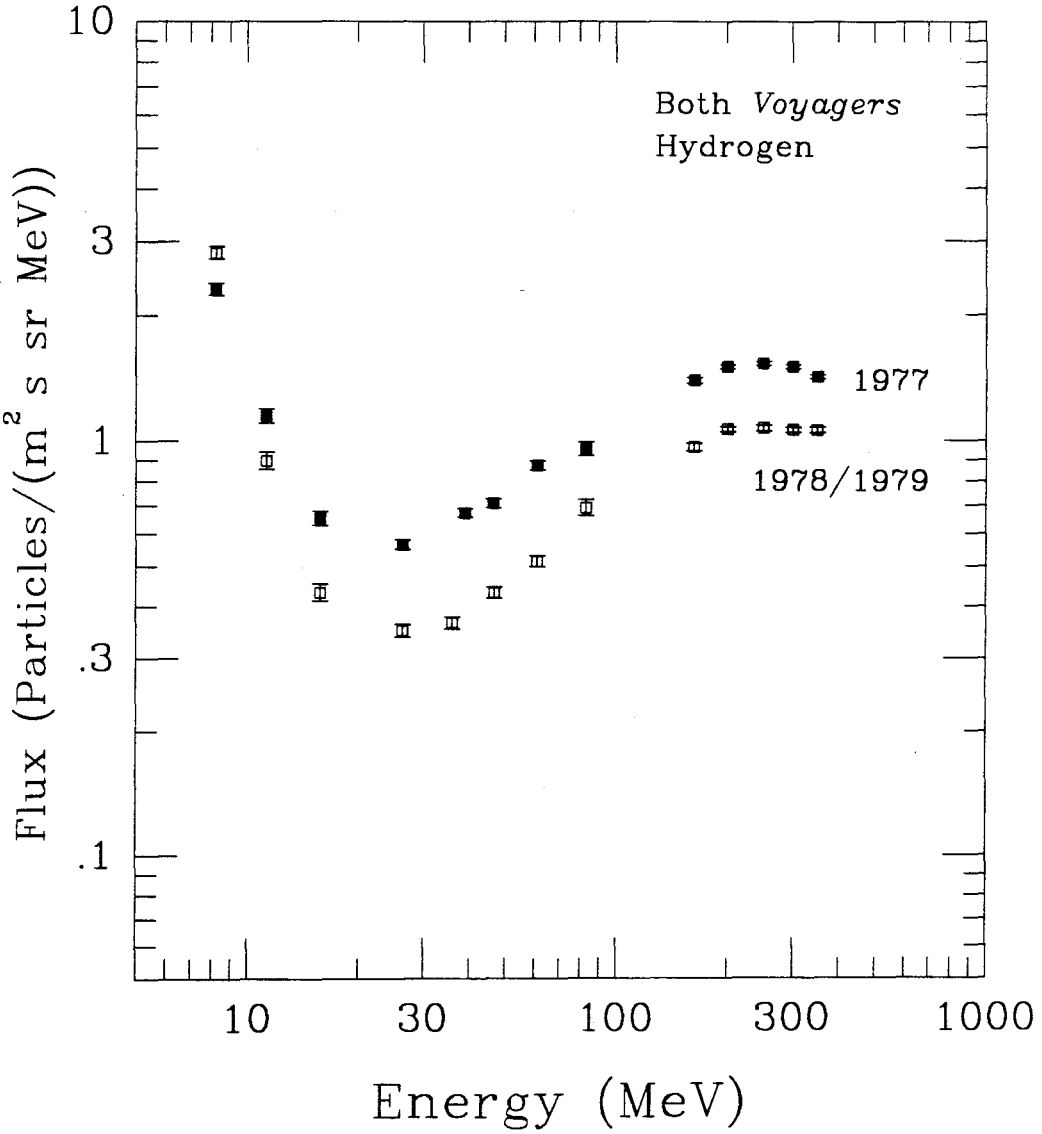
Both *Voyagers*
Hydrogen
1977
1978/1979
Flux (Particles/(m^2 s sr MeV))
Energy (MeV)
10
3
1
.3
.1
10
30
100
300
1000

Figure 3.28

Hydrogen energy spectra from Figure 3.27 with the fluxes divided by energy to flatten the energy spectra. The dashed curve represents the shape of the 1978/1979 energy spectrum scaled up to match the 1977 energy spectrum at the highest energy. The dotted curve is the 1978/1979 spectral shape shifted down 14% in energy and then up in flux to match the 1977 energy spectrum.

Figure 3.28

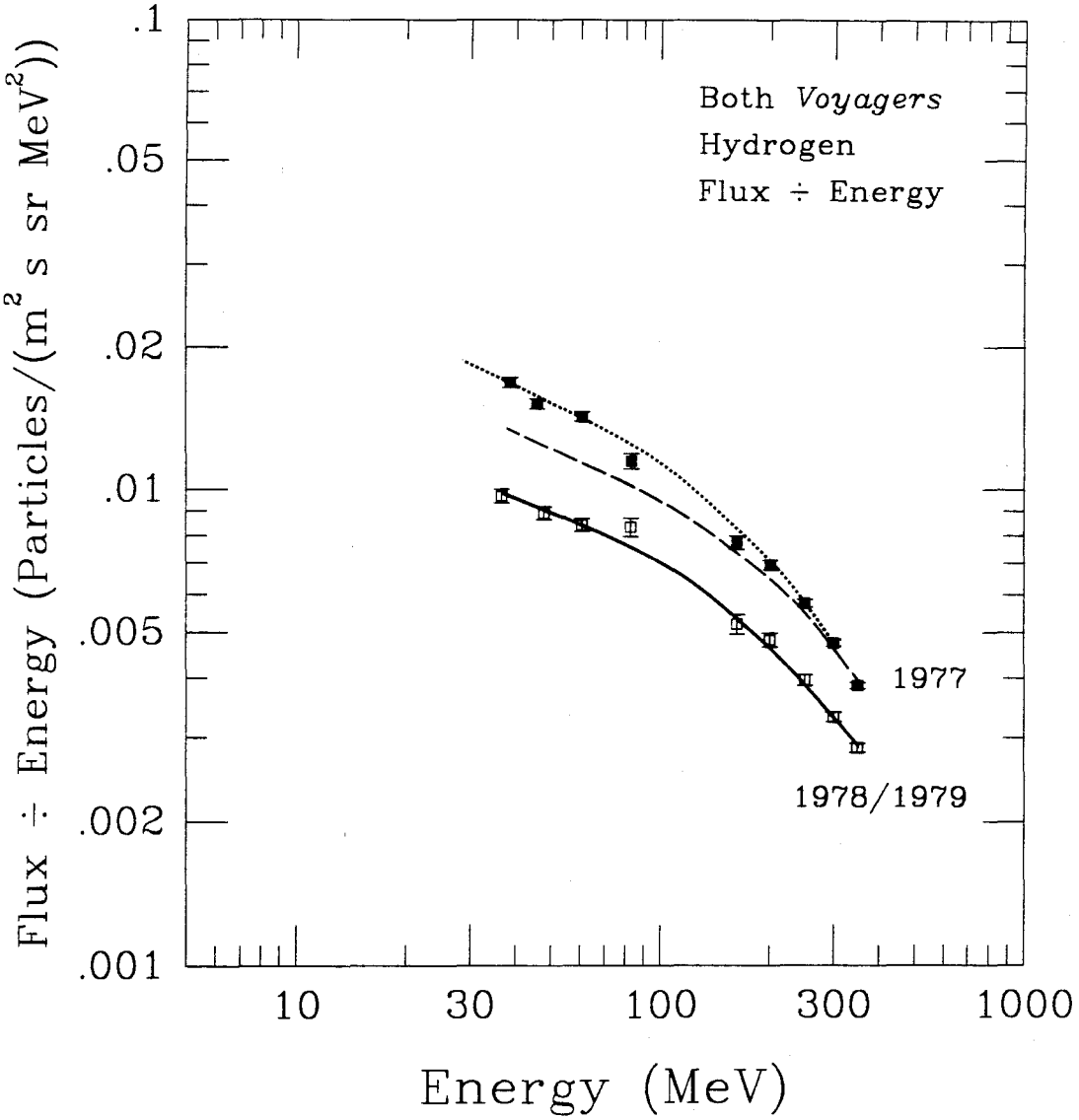
Both *Voyagers*
Hydrogen
Flux ÷ Energy
1977
1978/1979
.1
.05
.02
.01
.005
.002
.001
10
30
100
300
1000
Flux ÷ Energy (Particles/(m² s sr MeV²))
Energy (MeV)

Figure 3.29

First estimate of ACR hydrogen (solid squares) in the sum of both *Voyagers* for the time period 1977/335 - 361. The open squares are the observed hydrogen energy spectrum for this time period. The dotted curve shows the estimated galactic energy spectrum obtained by shifting the observed 1978/353 - 1979/14 up in flux to match the 1977 energy spectrum at the highest energy (350 MeV). The dashed curve is the least-squares fit of the ACR spectral shape to the first estimate points.

Figure 3.29

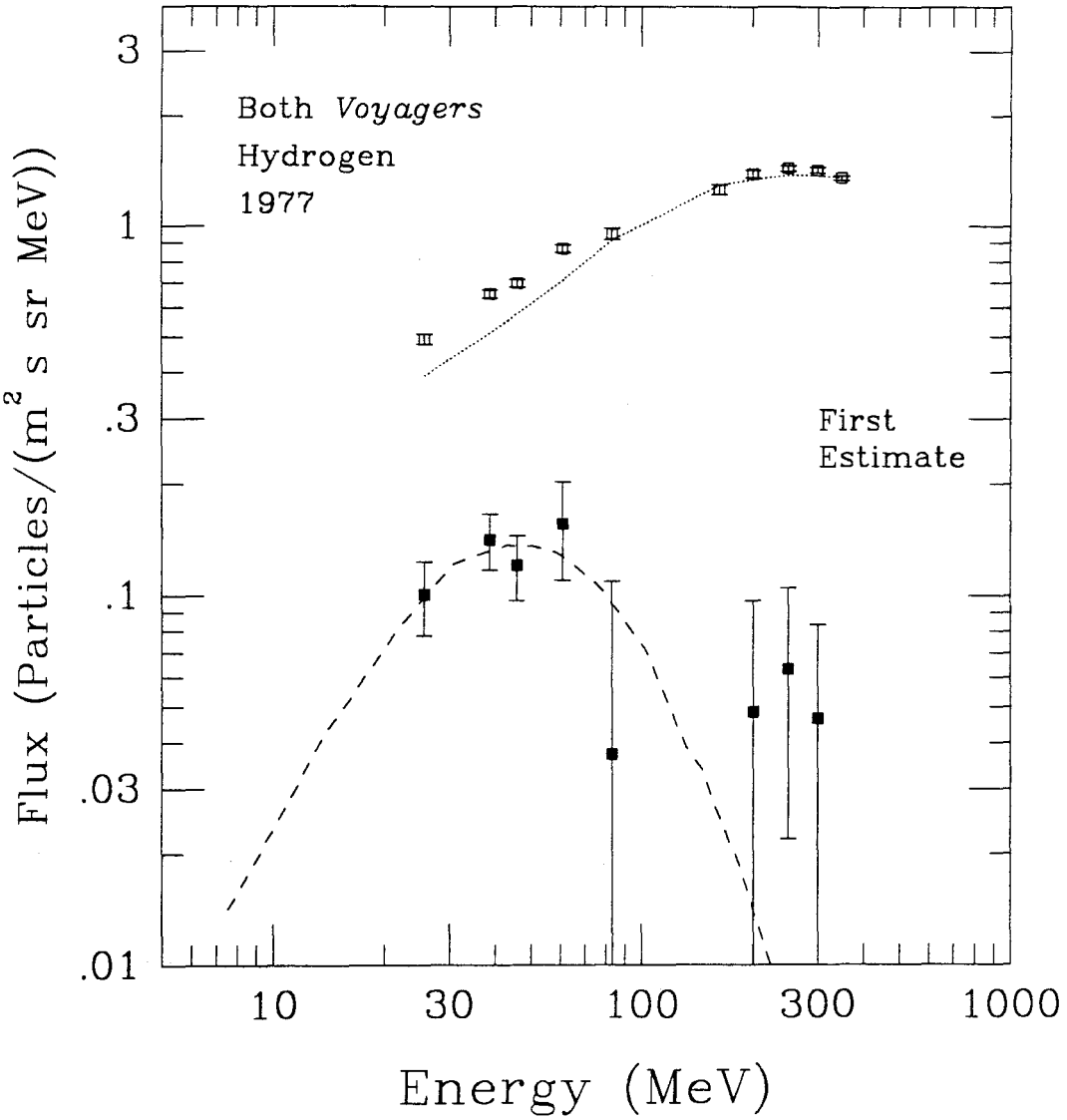
Both *Voyagers*
Hydrogen
1977
First
Estimate
Flux (Particles/(m^2 s sr MeV))
3
1
.3
.1
.03
.01
10
30
100
300
1000
Energy (MeV)

Figure 3.30

Four-parameter fit of GCR + ACR energy spectra (solid curve) to the observed 1977 *Voyager 1* + *Voyager 2* hydrogen energy spectrum (open squares). The dotted curve and the dashed curve show the decomposition of the solid curve into the galactic and anomalous components.

Figure 3.30

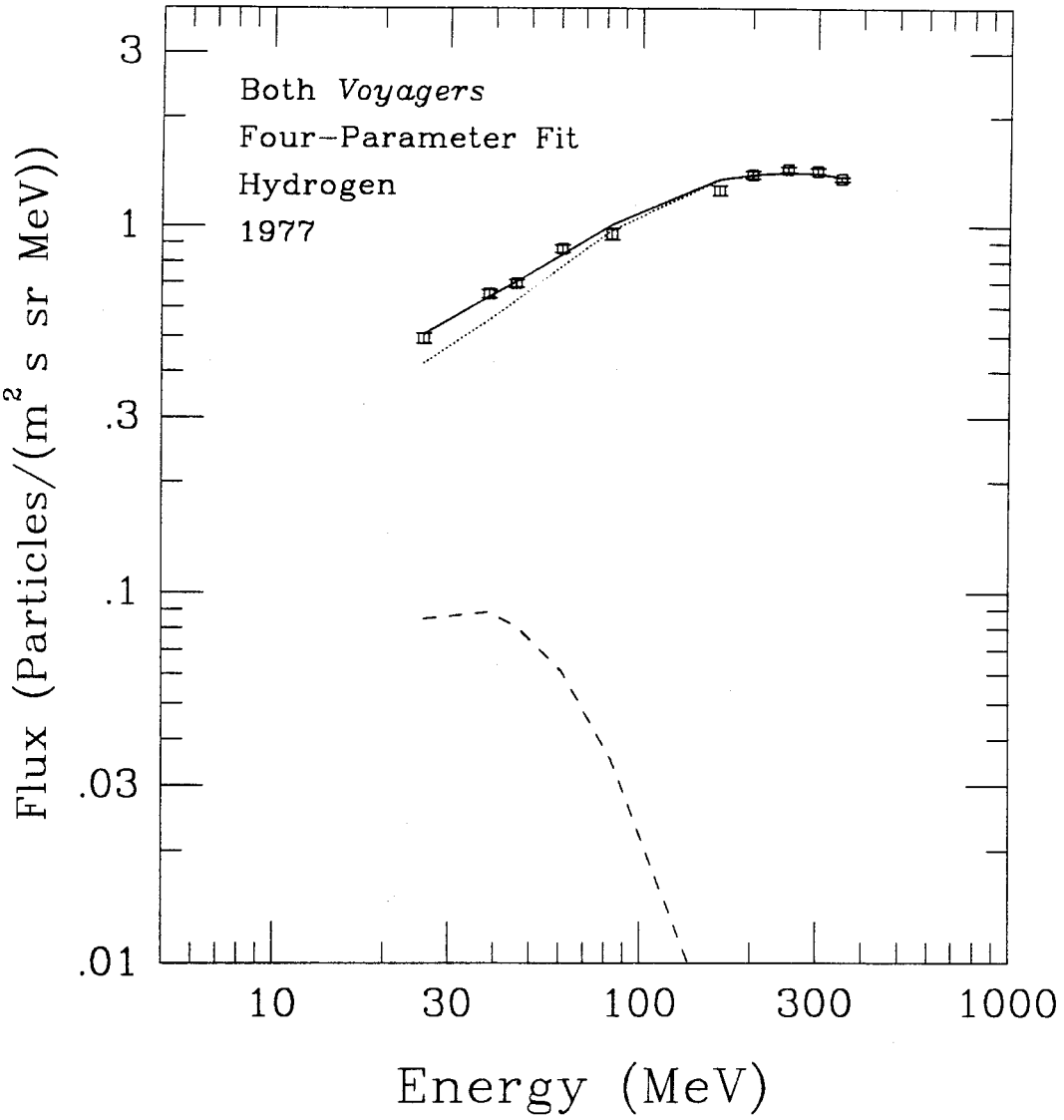
Both *Voyagers*
Four-Parameter Fit
Hydrogen
1977
3
1
.3
.1
.03
.01
10
30
100
300
1000
Flux (Particles/(m^2 s sr MeV))
Energy (MeV)

energies, whereas the 1985 and 1987 *Voyager 2* energy spectra of Figure 3.9 are clearly different shapes independent of any energy shift.

Assuming that some of the excess is due to anomalous hydrogen, a first estimate for this ACR component in 1977 can be calculated as in §3.2.1. This first estimate is shown in Figure 3.29 as well as the 1977 observed energy spectrum and the fit of the anomalous spectral shape to the first estimate. The excess is small, as expected, and is not as recognizable as a peak as the first estimates for the 1987 and 1988 time periods. This plot supports the same conclusion as arrived at from Figure 3.28. The spectral shape change seen between the 1977 and 1978/1979 time periods is consistent with a similar energy spectrum, which has been shifted in flux and energy, and is not well characterized by an excess peak at $\sim$100 MeV.

A four-parameter GCR + ACR fit, as described in §3.2.3, can be obtained for the 1977 observed hydrogen energy spectrum using the 1979 time period to give the shape of the galactic component. This fit is shown in Figure 3.30. This fit results in only an ACR contribution with a peak flux of $\sim$0.07 particles/m^2 s sr MeV at an energy of $\sim$43 MeV. This contribution is small and the peak energy occurs in a region where the SEP subtraction is still important, and so this ACR hydrogen value cannot be taken as significant.

This leaves the 1987/209 - 313 solar minimum data as presenting the clearest evidence for a hydrogen excess, which is consistent with a contribution of anomalous cosmic ray hydrogen to the observed hydrogen cosmic ray flux. The data from near the earlier solar minimum does not contradict this hypothesis, but neither does it add much evidence to support it.

Chapter 4

Discussion

4.1. Anomalous Cosmic Ray Hydrogen

Because the *Voyager 2* 1987 : 209 - 313 hydrogen energy spectrum shows the largest and most significant excess, it will be assumed that this time period gives the best estimate of the possible ACR hydrogen component. In order to account for the fact that modulation effects are a likely cause of at least some of the excess, and to allow for the uncertainties in the method of estimation, the median of the range of estimates in Figure 3.18 will be used as a measure of the anomalous cosmic ray hydrogen flux at *Voyager 2*, with an uncertainty that spans the entire range. Because solar modulation changes this value with time and spacecraft position, more interesting is the comparison of this flux with that observed for other elements at *Voyager 2* during the same time period. When this peak anomalous hydrogen flux 0.67 ± 0.18 particles/m^2 s sr MeV is compared with the peak anomalous helium flux, 1.80 ± 0.01 particles/(m^2 s sr (MeV/nucleon)) (from Figure 3.2), an observed H_{ACR}/He_{ACR} flux ratio of 0.37 ± 0.10 is obtained. This is larger than the published value of 0.20 ± 0.08 (Christian *et al.* 1988) primarily because the previous "upper estimate" is now at the bottom of the current range of the estimated ACR hydrogen peak flux.

It is widely believed that these anomalous cosmic rays originate as neutrals in the very local interstellar medium, so this observed flux ratio should relate to the relative neutral abundances of hydrogen and helium in the VLISM. However, this is not as straightforward as simply comparing particle counts. For one thing, the observed ratio

compares the fluxes of hydrogen and helium at very different energies. Also, the relative abundances are modified by fractionation, which occurs at several stages of the production of anomalous cosmic rays.

4.2. Composition of the VLISM

Cummings and Stone (1987) have developed a model that estimates the relative abundances of neutral atoms in the VLISM from the relative ACR peak fluxes. This model, with several recent additions and enhancements, provides the basis for the following discussion.

As described in §1.1.2, there are several steps in the generation of anomalous cosmic rays. The interstellar neutrals drift into the heliosphere with a bulk velocity equal to the velocity of the sun relative to the VLISM, which is about 20 km/s (Bertaux *et al.* 1985). To enter the solar system, the particles must first pass through a heliospheric interface, consisting of the heliopause, which separates the solar wind plasma from the ionized interstellar gas, and probably at least one shock transition (see, e.g., Axford 1972).

Several theories have been proposed that show a modification of the neutral interstellar gas as it passes through the heliospheric interface (see, e.g., Wallis 1981; Ripken and Fahr 1983) primarily because of charge exchange processes between the diverging flows of the neutral and the ionized components of the gas. This is a difficult problem because important parameters of the very local interstellar medium, such as magnetic field strength and ionization state, are not directly measured and difficult to estimate. Also, the subsonic region of the solar wind (beyond the solar wind termination shock) must be modeled because its parameters are unmeasured.

These theories are used to explain the discrepancies between the measured VLISM parameters of inflowing hydrogen and helium as measured by solar ultraviolet backscatter experiments (see §4.2.1). These discrepancies include possible temperature differences between hydrogen and helium as well as a possible difference in the apparent direction of approach (Paresce 1982). Typical of these theories is a decrease in the flux of neutral hydrogen transmitted through the interface, whereas helium suffers negligible attenuation.

Cummings and Stone (1987) calculated the abundances in the very local interstellar medium without including the effects of neutral gas modification in the heliospheric interface. Indeed, their analysis indicates that the modification may be small. Oxygen has a large charge-exchange cross section on protons and therefore if the neutral hydrogen is attenuated in the interface, the neutral oxygen should be also. Yet the results of Cummings and Stone (1987) show the abundance of oxygen to be unattenuated relative to helium, which has a small charge-exchange cross section.

Even though the level of hydrogen modification in the heliospheric interface is in question, we can still compare the ACR determined relative abundances of hydrogen and helium to the abundances in the inflowing neutral gas. This is very useful because solar ultraviolet backscatter experiments measure the flux of this inflowing gas, which is a precursor of anomalous cosmic rays.

4.2.1. Solar Ultraviolet Backscatter Experiments

Solar photons can resonantly scatter off the inflowing interstellar neutral gas. Neutral hydrogen scatters Lyman α (121.6 nm) photons and helium has a resonance wavelength of 58.4 nm. The characteristics of the interstellar gas can then be

determined by observing the backscattered photons. However, the resonant scattering emission pattern must be combined with a model of the interaction between the neutral gas and the sun (see, e.g., Axford 1972).

By comparing the backscatter observations with a heliospheric model, not only are the number densities of hydrogen and helium obtained, but also parameters such as inflowing velocity and the ionization rate of the neutral gas. These parameters are needed to calculate the ionization efficiency, which is used to correct the fractionation that occurs during ionization.

These observations have been done on many spacecraft starting with *OGO 5* in 1969 and including *Pioneer 10* and *Pioneer 11*, *Venera 11* and *Venera 12*, *Prognoz 5* and *Prognoz 6*, *Voyager 1* and *Voyager 2*, and others (see Ajello *et al.* 1987 for a summary of these observations). There is sizable scatter in the parameters obtained from these experiments, and so several sets of values will be investigated here. One set of characteristics is taken from *Prognoz 5* and *Prognoz 6* for hydrogen (Bertaux *et al.* 1985) and *Prognoz 6* for helium (Dalaudier *et al.* 1984). This has several advantages. For *Prognoz 6*, the hydrogen and helium data were taken at about the same time and are therefore easily comparable. Also, measurements were made primarily in 1977 when the solar activity, as indicated by 10.7 cm solar flux (National Geophysical Data Center 1988), was similar to that during the 1987 time period of the *Voyager* measurements. The 10.7 cm (2800 MHz) solar flux is commonly used as one of the standard indices of solar activity.

However, newer results have converged on values that differ substantially from the *Prognoz* observations. Therefore, this dissertation will also use parameters from *Pioneer Venus* (Ajello *et al.* 1987) for hydrogen, and *Voyager 1* and *Voyager 2* for helium (Chassefière *et al.* 1988).

4.2.2. Ionization Efficiency

There are several different processes that ionize the neutral atoms flowing into the inner heliosphere. Charge exchange with the solar wind is the primary cause of hydrogen ionization, whereas helium is dominated by photoionization. All the species have charge exchange and photoionization processes occurring although both rates vary from element to element.

Not only are the ionization rates different for the different species, but the particle orbits are also different. This is due to solar radiation pressure, which is small for most heavy elements, but is important for hydrogen. Solar radiation pressure can be approximated as a radial outward force that varies inversely with the square of the distance from the sun. Therefore, the particles' trajectories can be calculated using an effective gravitational constant $(1-\mu)G$ with μ being the ratio of the force of radiation pressure to the force of gravity. Hydrogen has $\mu \approx 1$ due to a large contribution from solar Lyman α radiation. Heavier atoms have trajectories that are dominated by gravity ($\mu << 1$) because the radiation pressure is small. It should be noted, however, that the exact value of μ is time variable because it depends on the solar photon flux, which varies with the solar activity cycle.

To calculate the fraction ionized or ionization efficiency (F_{ion}) for each of the elements, Cummings and Stone (1987) used a method similar to that outlined by Axford (1972) and briefly summarized here. Because all of the ionization processes vary inversely with the square of the distance to the sun, they can be combined into a single ionization rate, I_0, the fraction of particles ionized per second, usually referenced at a radius of 1 AU. The ionization rate will then be given by $I = I_0 \cdot r^{-2}$ (r given in AU) for any point within a boundary radius, r_b, corresponding to the solar wind termination shock. Particles are ionized outside the shock as well, but these particles are convected

away from the shock and thus are not accelerated and can be disregarded.

Due to gravitational focusing, particles with impact parameters larger than r_b can still have trajectories that bring the particles within the region of ionization. The maximum impact parameter b_{max} (in AU), is given by:

$$b_{max} = \left(\frac{2 r_b (1 - \mu) GM}{v^2} + r_b^2 \right)^{1/2} . \tag{4.1}$$

The mass of the sun is M, and v is the inflowing velocity (at infinity). If the thermal velocity is small compared to the bulk velocity, the so-called Cold Model, then v is just the bulk velocity of the interstellar gas relative to the sun, about 20 km/s (Bertaux *et al.* 1985).

The probability of ionization for a given particle is then:

$$p_{ion} (\mu, v, r_b, I_0) = 1 - e^{-\int_{t_i}^{t_f} I_0 \cdot r^{-2} \cdot dt} , \tag{4.2}$$

where t_i and t_f are the times that the particle enters and exits the ionization region respectively. The integral over time can be turned into an integral over angles, and the initial and final angles can be derived from the equation of the orbit:

$$p_{ion} (\mu, v, r_b, I_0) = 1 - e^{-\frac{I_0 \cdot (\theta_f - \theta_i)}{vb}} \tag{4.3}$$

$$\theta_f - \theta_i = \pi - 2 \cdot \sin^{-1} \left[\frac{A - r_b}{B r_b} \right] \tag{4.4}$$

$$A = \frac{v^2 b^2}{(1 - \mu) GM} \tag{4.5}$$

$$B = \left(1 \pm \frac{A^2}{b^2} \right)^{1/2} . \tag{4.6}$$

In Equation 4.6 the + is for $\mu < 1$ and the − is for $\mu > 1$. If $\mu = 1$ then:

$$\theta_f - \theta_i = \pi - 2 \cdot \sin^{-1} \left[\frac{b}{r_b} \right] . \tag{4.7}$$

Equation (4.3) gives the ionization probability for a single particle. The ionization efficiency for all particles that enter the ionizing region is:

$$f_{ion}(\mu, v, r_b, I_0) = \frac{\int_0^{b_{max}} p_{ion}\, 2\pi b\, db}{\pi\, b_{max}^2} . \tag{4.8}$$

This equation is integrated using Gauss-Legendre numerical integration to give the ionization efficiency for a given set of parameters.

4.2.2.1. Hot Model

However, the inflowing interstellar neutral gas is actually not cold, and its $\sim$10 000 K temperature (see, e.g., Ajello *et al.* 1987) gives it thermal velocities ($<v> \sim 16$ km/s for hydrogen), which are comparable to the bulk velocity. Therefore, the analysis of §4.2.1 should include the addition of random thermal velocities, a "hot model" (see, e.g., Dalaudier *et al.* 1984).

In order to investigate the importance of temperature on the ionization rate, I extended the analysis of Cummings and Stone (1987) by using a Monte Carlo simulation to add thermal velocities, u, to the bulk velocity. In the rest frame of the interstellar gas, the particles have a Maxwellian distribution of velocities distributed randomly in direction. This addition of a thermal velocity means that the particles no longer enter the ionizing region along parallel trajectories. Using a spherically symmetric ionization region makes this unimportant, because each trajectory can be arbitrarily

rotated. The Monte Carlo program generates a thermal velocity, adds it to the bulk velocity, and then calculates F_{ion} (equation 4.8) for the new velocity. Over many iterations, n, the program calculates:

$$F_{ion}(\mu, v, r_b, I_0, T) = \frac{\sum_{i=1}^{n} f_{ion}(\mu, |\vec{v} + \vec{u}_i(T)|, r_b, I_0)}{n} , \qquad (4.9)$$

with $\vec{u}_i$ being the random thermal velocity, and n typically equal to 10 000.

This Monte Carlo was used to obtain ionization efficiencies for H and He. As mentioned in §4.2.1, most of the parameters come from solar ultraviolet backscatter results:

Table 4.1

Parameter	Hydrogen(1)	Hydrogen(2)	Helium(3)	Helium(4)
V (km/s)	20 ± 1	22.5	27 ± 3	22
T (K)	8000 ± 1000	~ 10000	16000 ± 5000	9000
I_0 (s)	$3 \pm 1 \times 10^{-7}$	$8.4 \pm 1.7 \times 10^{-7}$	$1.25^{+0.29}_{-0.20} \times 10^{-7}$	$1.25^{+0.29}_{-0.20} \times 10^{-7}$
μ	0.75 ± 0.1	0.7–1.0	0	0
n_∞ (cm^{-3})	$3-6 \times 10^{-2}$	$7 \pm 1 \times 10^{-2}$	$1.5-2 \times 10^{-2}$	$1.0 \pm 0.45 \times 10^{-2}$

Table 4.1 Solar Ultraviolet Backscatter Parameters

(1)Bertaux *et al.* (1985)

(2)Ajello *et al.* (1987)

(3)Dalaudier *et al.* (1984)

(4)Chassefière *et al.* (1988)

This ionization efficiency is actually very insensitive to the radiation parameter, μ. For helium, the addition of a temperature makes a negligible difference in the ionization efficiency because u(T) << v; for hydrogen, the hot model analysis results in a decrease in ionization by less than 10%. To first order, the ionization efficiency is proportional to I_0, and inversely proportional to v.

However, the large uncertainty in the location of the solar wind termination shock (see §1.1.1) requires an understanding of the dependence of F_{ion} on the boundary radius, r_b, which represents the shock. Figure 4.1 shows this dependence for hydrogen and helium. The hydrogen curves use the parameters of Bertaux *et al.* (1985) from Table 4.1 except the cold model curve has a temperature of zero. The helium curve uses the parameters of Dalaudier *et al.* (1984) with the cold model ($T = 0°$) giving the same curve as the hot model. As can be seen, there is a strong dependence of the ionization efficiency on this boundary radius. However, because it is the relative ionization efficiencies of hydrogen and helium that is of interest, and both have similar dependencies upon the boundary radius, this is not as important. Figure 4.2 shows the ratio of the two ionization efficiencies from which it can be seen that the ratio changes by less than 10% even as r_b changes by a factor of three. From this analysis of the ionization efficiencies it has become clear that the lack of agreement in the ionization rate, I_0, is the cause of the largest uncertainties in the calculation of F_{ion}. If the *Prognoz* parameters are used ((1) and (3) from Table 4.1) the ratio F_{ion} (He)/F_{ion} (H) is 0.37 ± 0.19, meaning helium is ionized only ~40% as efficiently as hydrogen. If the newer parameters of Ajello *et al.* (1987) and Chassefière *et al.* (1988) are used ((2) and (4) from Table 4.1) then the relative ionization efficiency is F_{ion} (He) / F_{ion} (H) = 0.21 ± 0.06.

Figure 4.1

Ionization efficiency vs. boundary radius for hydrogen and helium. The hydrogen cold model has $T = 0\,^{\circ}K$ (dashed curve). The hydrogen hot model uses $T = 8000\,^{\circ}K$ (solid curve). The helium curve (dotted) is the same whether the cold model ($T = 0\,^{\circ}K$) or the hot model ($T = 16000\,^{\circ}K$) is used. The other parameters used were $I_0 = 3{\times}10^{-7}\ s^{-1}$, $v = 20$ km/s, and $\mu = 0.75$ (Bertaux *et al.* 1985) for hydrogen and $I_0 = 1.25{\times}10^{-7}\ s^{-1}$, $v = 27$ km/s, and $\mu = 0$ (Dalaudier *et al.* 1984) for helium (see Table 4.1).

Figure 4.1

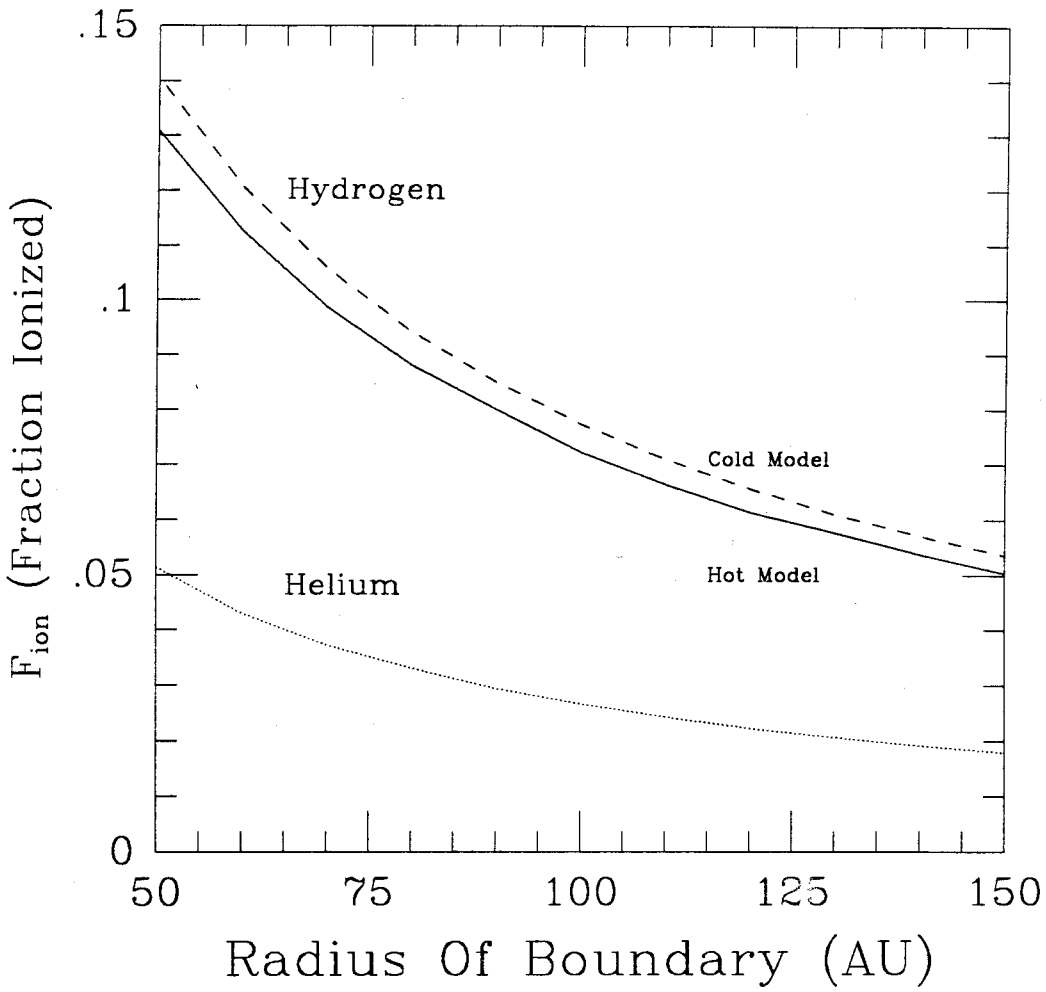
.15
.1
.05
0
F_{ion} (Fraction Ionized)
Hydrogen
Helium
Cold Model
Hot Model
50
75
100
125
150
Radius Of Boundary (AU)

Figure 4.2

Ratio of the ionization efficiency of helium to the ionization efficiency of hydrogen as a function of boundary radius. The hot model uses a temperature of 8000 ° K for hydrogen, whereas the cold model uses a 0 ° K. There is no difference between the two models in the ionization efficiency of helium. The other parameters used were $I_0 = 3 \times 10^{-7}\ s^{-1}$, v = 20 km/s, and $\mu = 0.75$ (Bertaux *et al.* 1985) for hydrogen and $I_0 = 1.25 \times 10^{-7}\ s^{-1}$, v = 27 km/s, and $\mu = 0$ (Dalaudier *et al.* 1984) for helium (see Table 4.1).

Figure 4.2

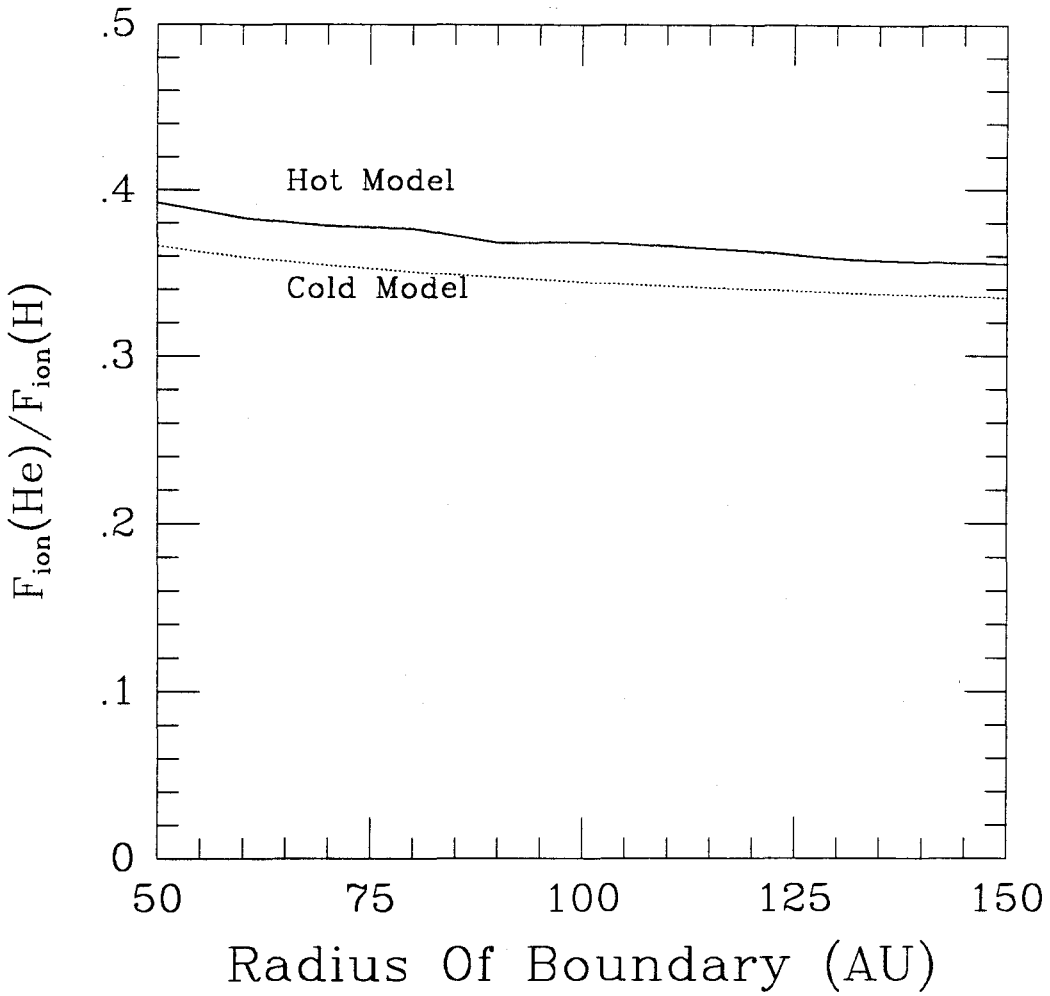
.5
.4
.3
.2
.1
0
Hot Model
Cold Model
$F_{ion}(He)/F_{ion}(H)$
50
75
100
125
150
Radius Of Boundary (AU)

4.2.3. Acceleration and Modulation Efficiency

Because it is believed that only the interstellar particles are accelerated at the solar wind termination shock, and not the solar wind particles, it is necessary to assume that the ionized interstellar particles remain as a distinct population separate from the solar wind particles. This assumption is easy to justify for helium and heavier species because the interstellar particles are only singly ionized as opposed to solar wind particles, which are fully ionized.

However, solar wind protons and ionized interstellar hydrogen both have the same ionization state, although the interstellar hydrogen does have a different velocity distribution than the solar wind. For this dissertation, we will assume that the interstellar hydrogen is not assimilated into the solar wind because the assimilation time scale should be much larger than the flow time to the solar wind termination shock (Isenberg 1986).

Because the ionized interstellar particles are separate from the solar wind population it will be assumed that the relative abundances of the elements remain constant during the transit out to the termination shock.

However, due to the different rigidity-to-energy relationship for different elements, there is almost certainly fractionation occurring during the acceleration process. This dissertation will rely on this model of the acceleration efficiency of anomalous cosmic rays, F_{acc}, developed by Cummings and Stone (1987).

The flare particle acceleration analysis of Dröge and Schlickeiser (1986) is applied to the ions assuming that losses are dominated by diffusion, and that the ions of different species are injected into the acceleration region at the same velocity. After acceleration, the differential energy spectra for singly ionized nuclei of different species have the same shape, to first order, after scaling in energy as

$$f_E \propto A^{-2\gamma/(\gamma+1)} \quad , \tag{4.10}$$

where γ is the coefficient in $K \propto \beta R^{\gamma}$ as in §3.1.2. The relative abundances at injection are then equal to the ratio of the accelerated energy spectra, after the proper energy scaling, times an acceleration correction factor, which is

$$F_{acc}(A_1, A_2) = \left(\frac{A_1}{A_2} \right)^{-(3\gamma+2)/(\gamma+1)} \quad , \tag{4.11}$$

where A_1 and A_2 are the two mass numbers, and with γ the same as in Equation 4.10.

It should be noted that the energy scaling of Equation 4.10 is the same as the modulation energy scaling of Equation 3.1. This explains why the anomalous energy spectra have very similar shapes. The input energy spectra are similar, and the energy scalings imply that the same relative point on the accelerated energy spectra will undergo the same level of modulation for different species. Because the fluxes of the anomalous spectral peaks are at the same modulation level and correspond to the same point on the acceleration energy spectra, the relative peak fluxes are directly proportional to the relative fluxes of the accelerated and shifted energy spectra.

This assumes that γ is about the same in both the region of acceleration and the region of modulation. If this is so, then the mass scaling of the ACR energy peaks from Figure 3.4 is an empirical measure of γ because the slope of the least-squares line should be equal to $-2\gamma/(\gamma+1)$. This gives a γ of 1.52 ± 0.01, almost identical to the $\gamma = 1.5$ obtained by Cummings and Stone (1987) for a time period a year earlier than the one used in Figure 3.4 even though the spectral peaks occurred at widely different energies for the two time periods.

This γ can then be used to calculate the acceleration factor in Equation 4.11. For hydrogen and helium $F_{acc}(H, He) \approx 37$. What this means is that if the hydrogen and

helium source abundances were the same, then the hydrogen flux at the ACR spectral peak would be 37 times less than the helium peak flux. Although the formal uncertainty of F_{acc} is small ($<< 1$), there is still a larger uncertainty from the theoretical model.

4.2.4. H I/He I in the VLISM

We now have all of the pieces we need to calculate the relative abundance of neutral hydrogen and helium (n(H I)/n(He I)) in the very local interstellar medium. Ignoring any fractionation that might occur just outside the heliospheric interface or to the ionized but not yet accelerated particles, the relative ACR fluxes, the ionization efficiencies, and the acceleration factor are combined as in Cummings and Stone (1987):

$$\frac{n(H\,I)}{n(He\,I)} = \frac{H_{ACR}}{He_{ACR}} \cdot \frac{F_{ion}(He)}{F_{ion}(H)} \cdot F_{acc}(H, He) \qquad (4.12)$$

If the *Prognoz* parameters (Bertaux *et al.* 1985, Dalaudier *et al.* 1984) are used, then a value, n(H I)/n(He I) = 5±3 is obtained, and if the more recent characteristics are used (Ajello *et al.* 1987, Chassefière *et al.* 1988) then n(H I)/n(He I) = 3±1. The indicated uncertainty excludes the unknown uncertainty in F_{acc} and any variation in F_{ion} due to changes in solar activity. The new figures bracket our previous value of 4±2 (Christian *et al.* 1988). These results can also be compared to the value of 2.6±0.9 obtained from the *Prognoz* spacecraft (Bertaux *et al.* 1985, Dalaudier *et al.* 1984). Chassefière *et al.* (1986) obtain a value of 6.5±3.1 with data from the *Venera 11* and *Venera 12* spacecraft, and Ajello *et al.* (1987) report a H/He ratio of 7±3 from *Pioneer Venus* (using the *Venera* helium results). These n(H I)/n(He I) values are shown in Figure 4.3. It can be seen that, despite modelling uncertainties, the n(H I)/n(He I) values obtained from the anomalous cosmic ray abundances are very similar to the

solar UV backscatter values. The scatter in the values also shows that our results are similarly sensitive to important parameters such as I_0 and v.

These n(H I)/n(He I) values are interesting because they differ systematically from the "cosmic" abundance ratio of ~10 (Anders and Grevesse 1989). If the inflowing hydrogen is not depleted in the heliospheric interfaces (see §4.2), then our results support the hypothesis (see Cox and Reynolds 1987 for review) that hydrogen in the very local interstellar medium is substantially (20% - 80%) ionized.

4.3. Conclusion

From the beginning of this analysis, it was known that the search for an anomalous cosmic ray hydrogen component would be difficult. It would require detecting the small effect of an anomalous cosmic ray hydrogen energy spectrum superimposed on a much larger galactic cosmic ray energy spectrum at the same time the galactic energy spectrum was undergoing changes due to modulation, which were not fully understood and so therefore could not be modeled.

Very early in the analysis it was noticed that the hydrogen energy spectrum had changed slope between 1985 and 1987 by more than would be expected by first order modulation theory. As the analysis evolved and was improved, the derived energy spectra changed by as much as 20% in absolute flux. But these modifications have never qualitatively changed the differences seen in the hydrogen energy spectra of *Voyager 2* between 1985 and 1987. The excess flux observed spans all three independent analysis regions (A-Stopping, B-Stopping, and Penetrating), which limits the possibility of a systematic error imitating the spectral shape change seen. It therefore seems very plausible to assume that the change in spectral shape observed is real. However, that still leaves the question of whether anomalous cosmic ray hydrogen or solar modulation

Figure 4.3

Comparison of derived values of n(H I)/n(He I) in the VLISM. In the first column are the results of this dissertation if the parameters of Bertaux *et al.* (1985) and Dalaudier *et al.* (1984) are used for hydrogen and helium respectively. The second column shows the results of this dissertation if the parameters of Ajello *et al.* (1987) and Chassefière *et al.* (1988) are used for hydrogen and helium respectively. Our previous results (Christian *et al.* 1988) are in column three. Column four contains the *Prognoz* results (Bertaux *et al.* 1985; Dalaudier *et al.* 1984). Column five is the *Venera 11* and *Venera 12* result (Chassefière *et al.* 1986) and column six is the *Pioneer Venus* hydrogen data (Ajello *et al.* 1987) combined with the *Venera* helium results (Chassefière *et al.* 1986).

Figure 4.3

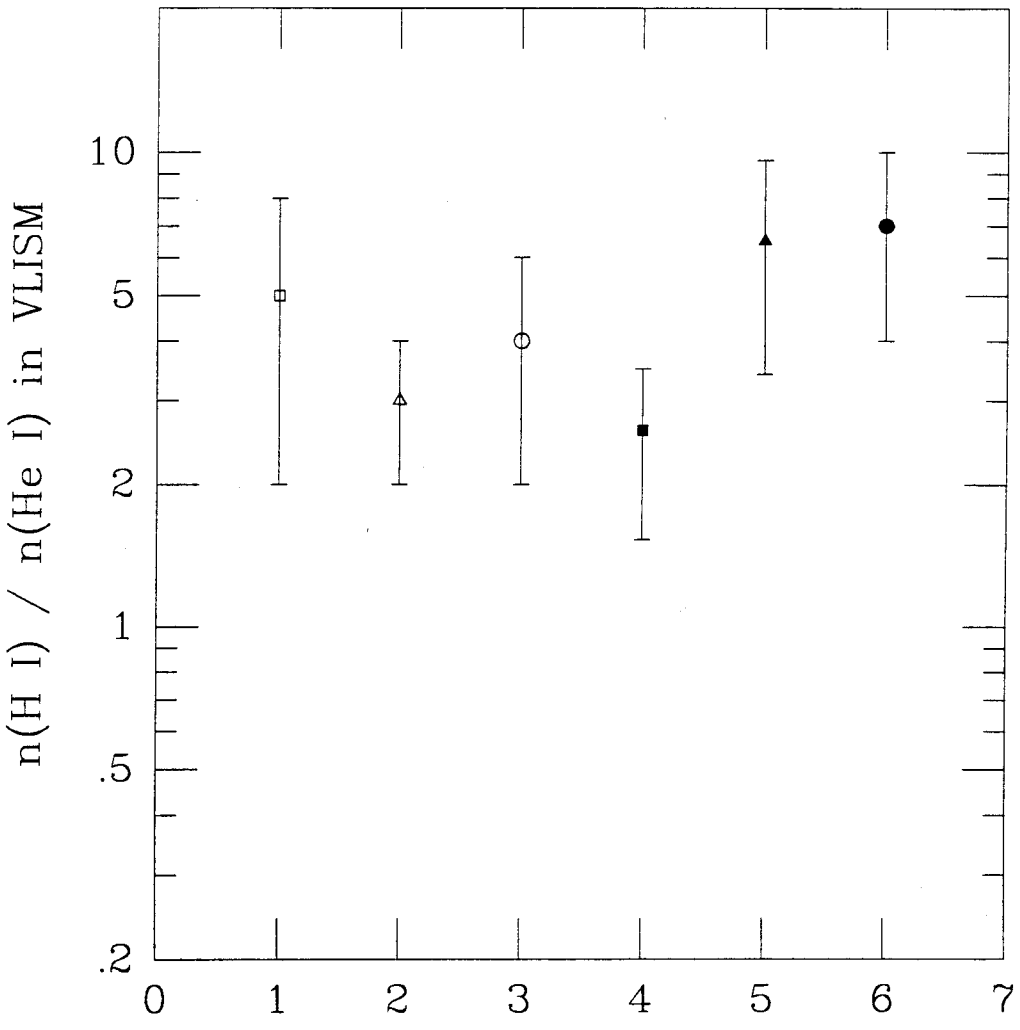

is the cause of this spectral shape change.

The typical explanation in the framework of modulation theory for this change in the spectral shape is that, as a consequence of the time dependent nature of modulation, the lower rigidity particles react to the decrease in modulation faster than the higher rigidity particles. However, the excess seen in the 1987 energy spectra occurs only in the intermediate energies, the lowest energies increase in flux at almost the exact same rate as the highest energies. Why only the intermediate energies should be affected is difficult to understand in the framework of modulation theory.

Also the fact that the effect is not seen in the carbon galactic energy spectra is another point against modulation being the sole cause of the change seen in the hydrogen energy spectra. However, modulation theory is still improving, and it is still possible that the entire effect seen in hydrogen can be explained in a complete, time-dependent modulation model.

On the other hand, the evidence is consistent with the hypothesis that some of this spectral shape change is due to an increase in the flux of anomalous cosmic ray hydrogen. As is shown in Chapter 3 the change can be characterized as an excess of flux in the intermediate energies between approximately 30 MeV and 300 MeV. This excess appeared in hydrogen at the time when the anomalous components of other elements were exhibiting an increase in flux at a rate much greater than the galactic components. The excess has a peak at about the correct energy for anomalous cosmic ray hydrogen, and the shapes of the estimates are very similar to the shape of other anomalous components. The ratio of the observed excess in *Voyager 2* and *Voyager 1* is also what would be expected for an anomalous component, both during the 1987 solar minimum and later in 1988 during the time of increasing solar modulation.

The absolute amount of ACR hydrogen observed is also completely consistent with the results of solar ultraviolet backscatter experiments. Admittedly, there are still uncertainties in the model relating the ACR fluxes to the relative abundances of neutrals in the VLISM. Even so, the agreement between the n(H I)/n(He I) value obtained in this dissertation and previous observations adds credence both to the Cummings and Stone (1987) method of deriving VLISM relative neutral abundances and this measurement of an ACR hydrogen component. With further theoretical work and better values for parameters, such as the hydrogen and helium ionization rates in the solar system, it should be possible to derive accurate relative abundances of neutrals in the VLISM from the observations of the composition of the anomalous cosmic ray component.

There are, of course, prospects for resolving the question of anomalous cosmic ray hydrogen in the future. In the near term, there are data from a detector on *Pioneer 10*, which is very similar to the HETs in the *Voyager* CRS. During the 1987 period of minimum solar modulation, *Pioneer 10* was in the ecliptic plane and further from the sun ($\sim$ 40 AU) than *Voyager 1* and *Voyager 2*. It correspondingly saw a larger amount of the anomalous cosmic ray component, both in absolute flux and relative to the flux of the galactic component. The *Pioneer 10* hydrogen energy spectra do show some shape change around the period of minimum modulation (MacDonald, private communication), and a very preliminary analysis indicates that the ratio of observed excess in *Pioneer 10* to *Voyager 2* is entirely consistent with an excess caused by an increase of an anomalous cosmic ray hydrogen component.

In the long term, because the level of solar modulation has increased to the point where ACR hydrogen is impossible to see, resolution of the ACR hydrogen question may have to wait until the *Pioneer* and *Voyager* spacecraft reach the solar wind

termination shock. This may be soon if the shock is indeed as close as 50 AU. Otherwise, the next solar minimum a decade hence will see the *Voyager* and *Pioneer* spacecraft even further from the sun, and then the increased contribution of the ACR component should clear up the problem of anomalous cosmic ray hydrogen.

References

Ajello, J. M., Stewart, A. I., Thomas, G. E., and Graps, A. 1987, *Ap. J.*, **317**, 964.

Anders, E., and Grevesse, N. 1989, in *Symposium on Cosmic Abundances of Matter* (Minneapolis 1988), AIP Conf. Proc. (in publication).

Axford, W. I. 1972, in *Solar Wind*, ed. C. P. Sonett, P. J. Coleman, and J. M. Wilcox (NASA SP-308) (Washington: NASA), p. 609.

Axford, W. I. 1985, *Solar Physics*, **100**, 575.

Bertaux, J. L., Lallement, R., Kurt, V. G., and Mironova, E. N. 1985, *Astr. Ap.*, **150**, 1.

Chassefière, E., Bertaux, J. L., Lallement, R., and Kurt, V. G. 1986, *Astr. Ap.*, **160**, 229.

Chassefière, E., Bertaux, J. L., Lallement, R., Sandel, B. R., and Broadfoot, L. 1988, *Astron. Astrophys.*, **199**, 304.

Christian, E. R. 1988, "Determination of Z, A, and Initial Energy from *Voyager* HET Events," Space Radiation Laboratory Internal Report 97, California Institute of Technology.

Christian, E. R. 1989, "HET Flux Normalizations for *Voyager 1* and *Voyager 2*," Space Radiation Laboratory Internal Report 98, California Institute of Technology.

Christian, E. R., Cummings, A. C., and Stone, E. C. 1988, *Ap. J. (Letters)*, **334**, L77.

Cook, W. R. 1981, "Elemental Composition of Solar Energetic Particles," Ph.D. diss., California Institute of Technology.

Cox, Donald P. and Reynolds, R. J. 1987, *Ann. Rev. Astron. Astrophys.*, **25**, 303.

Cummings, A. C., and Stone, E. C. 1987, in *Proc. 20th Internat. Cosmic Ray Conf. (Moscow)*, **3**, p. 413.

Cummings, A. C., and Stone, E. C. 1988, in *Proc. of Sixth Internat. Solar Wind Conf.*, ed. V. J. Pizzo, T. E. Holzer, D. G. Sime, **II**, p. 599.

Cummings, A. C., Stone, E. C., and Webber, W. R. 1984, *Ap. J. (Letters)*, **287**, L99.

Cummings, A. C., Stone, E. C., and Webber, W. R. 1987, *Geophys. Res. (Letters)*, **14**, 174.

Dalaudier, F., Bertaux, J. L., Kurt, V. G., and Mironova, E. N. 1984, *Astr. Ap.*, **134**, 171.

Dröge, W. and Schlickeiser, R. 1986, *Ap. J.*, **305**, 909.

Drury, L. O. 1988, in *Proc. Sixth Internat. Solar Wind Conf.*, ed. V. J. Pizzo, T. E. Holzer, D. G. Sime, **II**, p. 521.

Ferlet, R., Lallement, R., and Vidal-Madjar, A. 1986, *Astron. Astrophys.*, **163**, 204.

Fisk, L. A. 1971, *J. Geophys. Res.*, **76**, 221.

Fisk, L. A. 1986, in *The Sun and the Heliosphere in Three Dimensions*, ed. R. G. Marsden (Dordrecht: Reidel), p. 401.

Fisk, L. A., Kozlovsky, B., and Ramaty, R. 1974, *Ap. J. (Letters)*, **190**, L35.

Forbush, S. 1954, *J. Geophys. Res.*, **59**, 525.

Garcia-Munoz, M., Margolis, S. H., Simpson, J. A., and Wefel, J. P. 1979, *Proc. 16th Internat. Cosmic Ray Conf. (Kyoto)*, **1**, 310.

Garcia-Munoz, M., Mason, G. M., and Simpson, J. A. 1973, *Ap. J. (Letters)*, **182**, L81.

Garcia-Munoz, M., Mason, G. M., Simpson, J. A. 1975, *Ap. J.*, **202**, 265.

Garcia-Munoz, M., Mason, G. M., Simpson, J. A. 1977, *Ap. J.*, **213**, 263.

Garrard, T. L. 1976, "MJS CRS Science Requirements Document," Space Radiation Laboratory Technical Report 76-1, California Institute of Technology.

Heckman, H. H., Perkins, B. K., Simon, W. G., Smith, F. M., and Barkas, W. H. 1960, *Phys. Rev.*, **117**, 544.

Hess 1912, *Physik. Zeitschr.*, **13**, 1804.

Hovestadt, D., Vollmer, O., Gloeckler, G., and Fan, C. Y. 1973, *Phys. Rev. (Letters)*, **31**, 650.

Isenberg, P. A. 1986, *J. Geophys. Res.*, **91**, 9965.

Janni, J. F. 1966, "Calculations of Energy Loss, Range, Pathlength, Straggling, etc.," Technical Report AFWL-TR-65-150.

Jokipii, J. R. 1986, *J. Geophys. Res.*, **91**, 2929.

Lee, M. A. and Axford, W. I. 1988, *Astron. Astrophys.*, **194**, 297.

McDonald, F. B., Lal, N., Trainor, J. H., and Van Hollebeke, M. A. I. 1981, *Ap. J. (Letters)*, **249**, L71.

McDonald, F. B., Teegarden, B. J., Trainor, J. H., and Webber, W. R. 1974, *Ap. J. (Letters)*, **187**, L105.

McKibben, R. B., Pyle, K. R., and Simpson, J. A. 1988, *Ap. J. (Letters)*, **254**, L23.

Mewaldt, R. A., Spalding, J. D., and Stone, E. C. 1984, *Ap. J.*, **283**, 450.

Mewaldt, R. A., Stone, E. C., Vidor, S. B., and Vogt, R. E. 1975, in *Proc. 14th Internat. Cosmic Ray Conf. (Munich)*, **1**, p. 349.

Mewaldt, R. A., Stone, E. C., Vidor, S. B., and Vogt, R. E., 1976, *Ap. J.*, **205**, 931.

Mewaldt, R. A., Stone, E. C., and Vogt, R. E. 1975, in *Proc. 14th Internat. Cosmic Ray Conf. (Munich)*, **2**, p. 804.

National Geophysical Data Center. 1988, *Ottawa 10.7 cm Solar Flux diskette*, (Boulder: NOAA Environmental Data Information Service).

Ormes, J., and Freier, P. 1978, *Ap. J.*, **222**, 471.

Paresce, F. 1982, *Reports on Astronomy (Trans. of the IAU).* (Dordrecht: Reidel), 660.

Pesses, M. E., Jokipii J. R., and Eichler, D. 1981, *Ap. J. (Letters)*, **246**, L85.

Potgieter, M. S., and Moraal, H. 1988, *Ap. J.*, **330**, 445.

Ripken, H. W., and Fahr, H. J. 1983, *Astron. Astrophys.*, **122**, 181.

Rygg, T. A., and Earl, J. A. 1967, *J. Geophys. Res.*, **76**, 7445.

Simpson, J. A. 1983, *Ann. Rev. Nucl. Part. Sci.*, **33**, 323.

Stilwell, D. E., Davis, W. D., Joyce, R. M., McDonald, R. B., Trainor, J. H., Althouse, W. E., Cummings, A. C., Garrard, T. L., Stone, E. C., and Vogt, R. E. 1979, *IEEE Trans. Nucl. Sci.*, **NS-26(1)**, 513.

Stone, E. C. 1987, in *Proc. 20th Internat. Cosmic Ray Conf. (Moscow)*, **7**, p. 105.

Stone, E. C., Vogt, R. E., McDonald, F. B., Teegarden, B. J., Trainor, J. H., Jokipii, J. R., and Webber, W. R. 1977, *Space Sci. Rev.*, **21**, 355.

Vidal-Madjar, A., Laurent, C., Bruston, P., and Audouze, J. 1978, *Ap. J.*, **223**, 589.

Wallis, M. K. 1981, in *Proc. Fourth Solar Wind Conf.*, ed. H. Rosenbauer, p. 516.

Webber, W. R. 1987, *Astron. Astrophys.*, **179**, 277.

Weller C. S., and Meier, R. R. 1981, *Ap. J.*, **246**, 386.